Masterarbeit

Nanostructured S-Layer Affinity Matrix for Cell Capture in Microfluidic Devices

Autorin

Barbara Theiler

zur Erlangung des akademischen Grades einer

Diplom-Ingenieurin

Technische Universität Graz

Studienrichtung: Biotechnologie (F 066 484)

durchgeführt am Department für NanoBiotechnologie der Universität für Bodenkultur Wien
in Kooperation mit dem AIT Austrian Institute of Technologies, Abteilung für Nano Systems

Betreuer/in: Ao.Univ.Prof. Dipl.-Ing. Dr.techn. Dietmar Pum,
Dipl.-Ing. Dr.techn. Seta Küpcü, Dipl.-Ing. Dr.habil. Peter Ertl

August 2011

To my Family

Statutory declaration

I declare that I have authored this thesis independently, that I have not used other than the declared sources/resources, and that I have explicitly marked all material which has been quoted either literally or by content from the used sources.

…… ……..

date (signature)

Acknowledgements

First of all I would like to thank my advisor Seta Küpcü at DNBT and my second advisor Peter Ertl at AIT for their constant support during experimental work and writing of this master thesis. As both are great advisors, they kept up having patience and faith in my abilities. I would also like to thank Andreas Breitwieser, Jacqueline Friedmann and Andrea Scheberl at DNBT for supplying essential samples and always lending an ear to my questions and concerns. Furthermore, I want to thank Mario Rothbauer, Verena Charwat and Lukas Richter at AIT for creating such a pleasant working atmosphere and for their generous help. Thank you also goes to Ronald Zirbs at DNBT for backing me with humor and sympathy.

In addition, I would like to thank my supervisor Dietmar Pum at DNBT for taking over the universal supervision and spending time for my requests. Also thanks to Uwe Sleytr for introducing me to the world of S-layers and microfluidics.

Finally, I would like to thank my family for their great support and confidence.

Zusammenfassung

Die Erfassung und Untersuchung von seltenen Zellen, wie bestimmten T-Lymphozyten und zirkulierenden Tumorzellen, ist in der heutigen medizinischen Diagnostik von immer größer werdender Bedeutung. Hierbei spielen vor Ort einsetzbare Testgeräte eine wichtige Rolle, um in Entwicklungsländern effiziente und kostengünstige Diagnose-Systeme bereitstellen zu können. Mikrofluidische Systeme zeichnen sich durch einzigartige Eigenschaften wie den geringen Volumenverbrauch, den kleinen Maßstab, hoch laminare Flussbedingungen und die einfache Handhabung aus. Mikrofluidische Geräte ermöglichen und erleichtern die Erfassung von seltenen Zellen innerhalb spezifisch modifizierter Mikrokanäle, die gut auf die Bedürfnisse von lebenden Zellen angepasst werden können. In dieser Masterarbeit wird eine CD3-Affinitätsmatrix vorgestellt, welche auf dem kristallinen Immunoglobulin G (IgG)-bindenden S-Schicht-Fusionsprotein rSbpA$_{31\text{-}1068}$/ZZ von *Lysinibacillus sphaericus* CCM 2177 basiert. Diese CD3-Affinitätsmatrix soll in mikrofluidischen Systemen zur Erfassung seltener Zellen über spezifische IgG-Antikörper, die auf dem S-Schicht-Fusionsprotein immobilisiert sind, Anwendung finden. S-Schicht-Proteine verfügen über besondere Attribute wie Antifouling-Eigenschaften und die Fähigkeit, selbständig auf Oberflächen zu assemblieren. Bezüglich Oberflächenanalyse wurde die Rasterkraftmikroskopie (AFM) herangezogen, um das rekristallisierte Gitter des S-Schicht-Fusionsproteins unter anderem auf dem Polymer SU8 zu untersuchen. Das Polymer SU8 gewinnt in der Herstellung von Mikrofluidik-Systemen zunehmend an Bedeutung. Weiters wurde die IgG-Affinitätsmatrix mittels „Enzyme linked immunosorbent assay“- und Oberflächenplasmonenresonanz-Experimenten untersucht. Basierend auf der IgG-Affinität des S-Schicht-Fusionsproteins wurde eine CD3-Affinitätsmatrix für die spezifische Erfassung von CD3-Lymphozyten entwickelt. Diese Affinitätsmatrix wurde in mehreren statischen und mikrofluidischen Anordnungen, bestehend aus verschiedenen Materialen wie Glas, Polydimethylsiloxan und SU8, angewandt. Zur Quantifizierung und Untersuchung der Linearität bezogen auf die Menge an Zellbedeckung wurde ein Lichtstreuungsdetektionssystem eingesetzt. Aufgrund der einzigartigen Eigenschaften von mikrofluidischen Systemen und der multifunktionalen Attribute von S-Schicht-(Fusions)proteinen, bietet eine Kombination aus beiden einen herausfordernden und vielversprechenden Ansatz für die medizinische Diagnostik und die Untersuchung von Biomolekülen.

Abstract

The capture and investigation of rare cells, such as certain T-lymphocytes and circulating tumor cells, has become increasingly important to today's medical diagnostics. In particular, point-of-care devices are of major interest in order to provide quick and affordable diagnostic systems for developing countries. Microfluidic systems feature unique properties such as low volume requirements, a small scaling factor, highly laminar flow conditions, and easy handling procedures. Such fluidic devices enable and facilitate the capture of rare cells within specifically modified microchannels which can be adapted well to the requirements of living cells. In this master thesis, a CD3-affinity matrix based on the crystalline immunoglobulin G (IgG)-binding surface layer (S-layer) fusion protein rSbpA$_{31\text{-}1068}$/ZZ of *Lysinibacillus sphaericus* CCM 2177 is presented. This approach can be applied in microfluidic devices for the immunocapture of rare cells via specific IgG-antibodies immobilized on the S-layer fusion protein. S-layer proteins offer particular characteristics such as antifouling properties and the ability of performing self-assembly on surfaces. In terms of surface analytical methods, atomic force microscopy was used for the analysis of the S-layer fusion protein lattice recrystallized on the negative photoresist SU8. The polymer SU8 is becoming more and more relevant in the fabrication of microfluidic devices. Further, the IgG-affinity matrix was investigated by performing enzyme linked immunosorbent assay and Surface Plasmon Resonance experiments. Based on the established IgG-affinity of the S-layer fusion protein, a CD3-affinity matrix was developed for the specific immunocapture of CD3-lymphocytes. This affinity matrix was studied in various static and microfluidic cell capture devices fabricated of different materials, such as glass, polydimethylsiloxane and SU8. In terms of quantification and investigation of linearity relating to the amount of cell coverage, a light scattering detection system was used. Due to the unique features of microfluidic systems and the multifunctional characteristics of S-layer (fusion) proteins, their combination presents a challenging and promising approach for medical diagnostics and the study of biomolecules.

Outline of the thesis

The structure of this thesis implies an *Introduction* at the beginning describing S-layer fundamentals and technology, microfluidic fundamentals, microfluidic rare cell capture, and analytical techniques in microfluidic devices. The section *Aim of the thesis* describes the goal of this research based on the literature presented in the *Introduction*. The *Materials and Methods* include the establishment of the CD3-affinity matrix, the cell capture experiments in static manner and in microfluidic devices as well as the light scattering measurements in terms of an analytical approach. Basically, the fundamentals of each detection system are explained for a better understanding of the conducted experiments. The *Results and Discussion* part presents and interprets the outcome of all experiments. The thesis ends with a *Conclusion* summarizing the results and providing an outlook.

Index

1 Introduction 1
1.1 Surface layer proteins 1
1.1.1 Ultrastructure and chemical characterization 1
1.1.2 Isolation and recrystallization 3
1.1.3 Antifouling properties of S-layer proteins 4
1.1.4 S-layer fusion proteins 5
1.1.4.1 The S-layer fusion protein rSbpA/ZZ 6
1.2 Micro total analysis systems 8
1.2.1 General aspects of micro total analysis systems 8
1.2.2 Microfluidic fundamentals 9
1.2.3 Fabrication of microfluidic devices with PDMS and SU8 11
1.2.4 Air bubbles in microfluidics 12
1.3 Microfluidic rare cell capture 13
1.3.1 Electrokinetic methods 13
1.3.2 Non-electrokinetic methods 14
1.3.2.1 Cell capture via antibody immobilization or aptamer chemistry 14
1.3.2.1.1 Blood cell fractionation – capture of T-lymphocytes 15
1.3.2.1.2 Capture of cancer cells – the influence of microfluidic geometry 16
1.3.2.1.3 Isolation of other mammalian cells 17
1.4 Analytical techniques for microfluidic devices 18
1.4.1 Pathogen sensing in microfluidic devices 18
1.4.2 Optical sensing systems for microfluidic devices 18
1.4.2.1 Coupling of optical detection systems: off-chip approach 19
1.4.2.2 Integration of optical functions: on-chip approach 20
2 Aim of the thesis 22
3 Materials and Methods 23
3.1 S-layer proteins 23
3.1.1 S-layer protein SbpA 23
3.1.2 S-layer fusion protein rSbpA/ZZ 23
3.1.3 Recrystallization of S-layer proteins 23
3.2 Atomic Force Microscopy 24
3.2.1 Fundamentals of AFM 24
3.2.2 AFM imaging of recrystallized rSbpA/ZZ 25

3.3 Enzyme linked immunosorbent assay 26
3.3.1 Fundamentals of ELISA 26
3.3.2 SbpA and rSbpA/ZZ recrystallization and preparation for the immobilization of human IgG 27
3.3.3 Detection of human IgG immobilization on SbpA and rSbpA/ZZ 28
3.3.4 Optimization of human IgG detection on rSbpA/ZZ 29
3.4 Surface Plasmon Resonance 30
3.4.1 Fundamentals of SPR 30
3.4.2 Sensor chip preparation 31
3.4.3 Recrystallization of the S-layer proteins SbpA and rSbpA/ZZ 32
3.4.4 Investigation of antibody binding and antifouling properties 33
3.4.4.1 Antifouling properties of rSbpA/ZZ 33
3.4.4.2 Binding of human IgG and CD3-Ab to rSbpA/ZZ 34
3.4.4.2.1 Antifouling properties of rSbpA/ZZ with immobilized CD3-Ab 35
3.5 Static cell capture 36
3.5.1 The T-cell receptor-CD3 complex 36
3.5.2 The Jurkat cell line – CD3-cells 37
3.5.3 Jurkat cell capture via CD3-Ab immobilized on rSbpA/ZZ protein 37
3.5.4 Specific Jurkat cell capture from a cell mixture 38
3.5.4.1 Cell labeling of Jurkat and MOLT 3 cells 38
3.5.4.2 Specific Jurkat cell capture from a cell mixture of Jurkat and MOLT 3 cells via CD3-Ab immobilized on rSbpA/ZZ 38
3.5.4.2.1 Microscopical setup 39
3.6 Microfluidic cell capture 40
3.6.1 Mask designs for PDMS and SU8 fabricated microchips 40
3.6.1.1 Mask design for PDMS fabricated microfluidic chips 40
3.6.1.2 Mask design for SU8 fabricated microfluidic chips 41
3.6.2 Master mold fabrication for PDMS microchips 42
3.6.3 Microfluidic PDMS chip assembly 42
3.6.4 Cell capture experiments in PDMS microchips 44
3.6.4.1 System components for PDMS microchips 44
3.6.4.2 Static modification of PDMS microchips with rSbpA/ZZ and CD3-Ab 44
3.6.4.3 Microfluidic Jurkat cell capture in modified PDMS microchips 45
3.6.5 Cell capture experiments in SU8 microchips 46
3.6.5.1 System components 47
3.6.5.2 Static modification of SU8 microchips with rSbpA/ZZ and CD3-Ab 48
3.6.5.3 Microfluidic Jurkat cell capture in modified SU8 microchips 50

3.6.5.3.1 The cell-injecting mode 50
3.6.5.3.2 The cell-withdrawing mode 50
3.7 Cell capture detection via light scattering 51
3.7.1 Fundamentals of organic photodiodes 51
3.7.2 Light scattering detection setup 52
3.7.3 Jurkat cell capture in modified PDMS reservoirs 53
3.7.4 LS measurements for Jurkat cell capture detection 54
4 Results and Discussion 55
4.1 AFM imaging of recrystallized rSbpA/ZZ lattice 55
4.2 Enzyme linked immunosorbent assay 56
4.2.1 SbpA and rSbpA/ZZ recrystallization and preparation for the immobilization of human IgG 56
4.2.2 Detection of human IgG immobilization on SbpA and rSbpA/ZZ 56
4.2.3 Optimization of human IgG detection on rSbpA/ZZ 57
4.3 Surface Plasmon Resonance 59
4.3.1 Recrystallization of the S-layer proteins SbpA and rSbpA/ZZ 59
4.3.1.1 Antifouling properties of rSbpA/ZZ 59
4.3.2 Binding of human IgG and CD3-Ab to rSbpA/ZZ 61
4.3.2.1 Antifouling properties of rSbpA/ZZ with immobilized CD3-Ab 62
4.4 Static cell capture 64
4.4.1 Jurkat cell capture via CD3-Ab immobilized on rSbpA/ZZ protein 64
4.4.2 Specific Jurkat cell capture from a cell mixture of Jurkat and MOLT 3 cells via CD3-Ab immobilized on rSbpA/ZZ 64
4.5 Microfluidic cell capture 66
4.5.1 Static modification of PDMS microchips with rSbpA/ZZ and CD3-Ab 66
4.5.2 Microfluidic Jurkat cell capture in modified PDMS microchips 66
4.5.3 Static modification of SU8 microchips with rSbpA/ZZ and CD3-Ab 67
4.5.4 Microfluidic Jurkat cell capture in modified SU8 microchips 67
4.5.4.1 The cell-injecting mode 68
4.5.4.2 The cell-withdrawing mode 69
4.6 LS measurements for Jurkat cell capture detection 70
5 Conclusion 72
6 Appendix 73
6.1 References 73
6.2 List of Figures 80
6.3 List of Tables 82
6.4 Abbreviations 83

1 Introduction

1.1 Surface layer proteins

Surface layer (S-layer) proteins are a self-assembly system that has been optimized during the course of evolution. Organisms containing regularly structured protein lattices as their outermost cell envelope component are omnipresent. S-layer proteins completely cover the cell surface during all stages of growth and division. They have been identified in all major groups of bacteria and represent an almost universal feature of archaea (1) (2).

1.1.1 Ultrastructure and chemical characterization

Genetic studies and chemical analysis revealed that the monomolecular assembly of these crystalline cell surface layers is the result of secretion and crystallization of identical proteins or glycoproteins on the cell wall. Their molecular mass ranges from 40 to 200 kDa (3) (4) (5) (6). S-layers can be visualized by using electron microscopy combined with techniques such as freeze etching (Fig. 1) or negative staining (7) (8) (9).

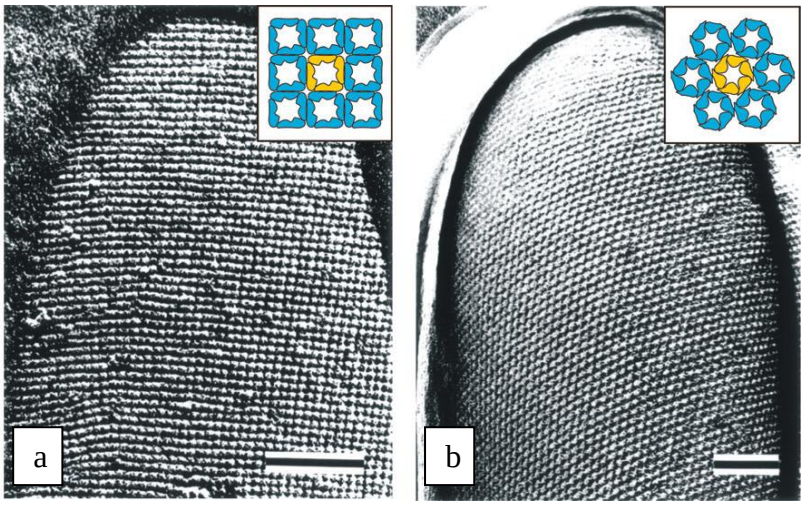

Fig. 1: Electron micrographs of freeze-etched preparations of intact cells.
(a) *Desulfotomaculum nigrificans* NCIB 8706 showing a square (p4) lattice type; scale bar; 150 nm. (b) *Thermoanaerobacter thermohydrosulfuricus* L111-69 showing hexagonal (p6) lattice symmetry; scale bar: 100 nm. Inserts: schematic drawings of the different S-layer lattice types (10), slightly modified.

The cell wall architecture of gram-positive bacteria and archaea (Fig. 2) is composed of a rigid cell wall component (peptidoglycan: bacteria, pseudomurein: archaea) and an S-layer directed externally to the cytoplasmic membrane (4) (11). Additionally, many of these

bacteria possess a secondary cell wall polymer (SCWP); this polymer interacts with the N-terminal part of the S-layer subunits and is involved in anchoring those subunits to the rigid cell wall layer (12).

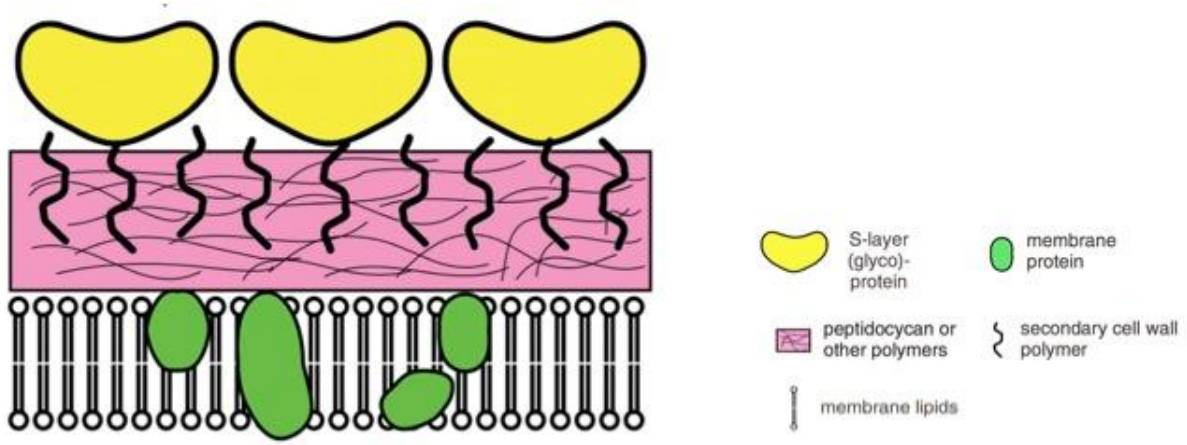

Fig. 2: Schematic illustration of the cell wall architecture of gram-positive archaea and bacteria containing crystalline S-layer proteins (11), modified.

S-layers are planar self-assembly products. The center-to-center spacing between the morphological units is a specific feature and ranges from 3.5 to 35 nm. In bacteria, the S-layer subunits are linked to each other as well as to the underlying cell envelope layer by non-covalent forces. The lattice types show oblique (p1, p2), square (p4), or hexagonal (p3, p6) symmetry (Fig. 3). Amongst archaea, hexagonal symmetry predominates (13). One morphological unit is built of one (p1), two (p2), three (p3), four (p4) or six (p6) identical proteins depending on the S-layer lattice type (7).

Bacterial S-layers are generally 5 to 25 nm thick, while S-layers of archaea reveal a thickness of up to 70 nm (7) (14). Due to their high structural regularity, they present unique systems for synthesis-, genetics- and structure-studies (15) (7). S-layers possess a large amount of hydrophobic amino acids (40-60 mol%), almost no sulfur-containing amino acids and about 25 mol% charged amino acids. Lysine predominates as basic amino acid, while generally the content of arginine, histidine and methionine is low (16) (17).

The main post-translational modifications are glycosylation (18) (19) (20) and phosphorylation (21). Most S-layer lattices are formed of rather acidic proteins with an isoelectric point of pH 4-5 (9). Exceptions are S-layer proteins from *Lactobacillus* strains with an isoelectric point in the alkaline pH range (22). Amongst others, differences in surface net charge and in hydrophobicity of the inner and outer surface are important characteristics; they are responsible for the orientation and incorporation of S-layer subunits on cell surfaces. S-

layers are dynamic closed surface crystals which assume a structure of low free energy during cell growth and division (4) (23).

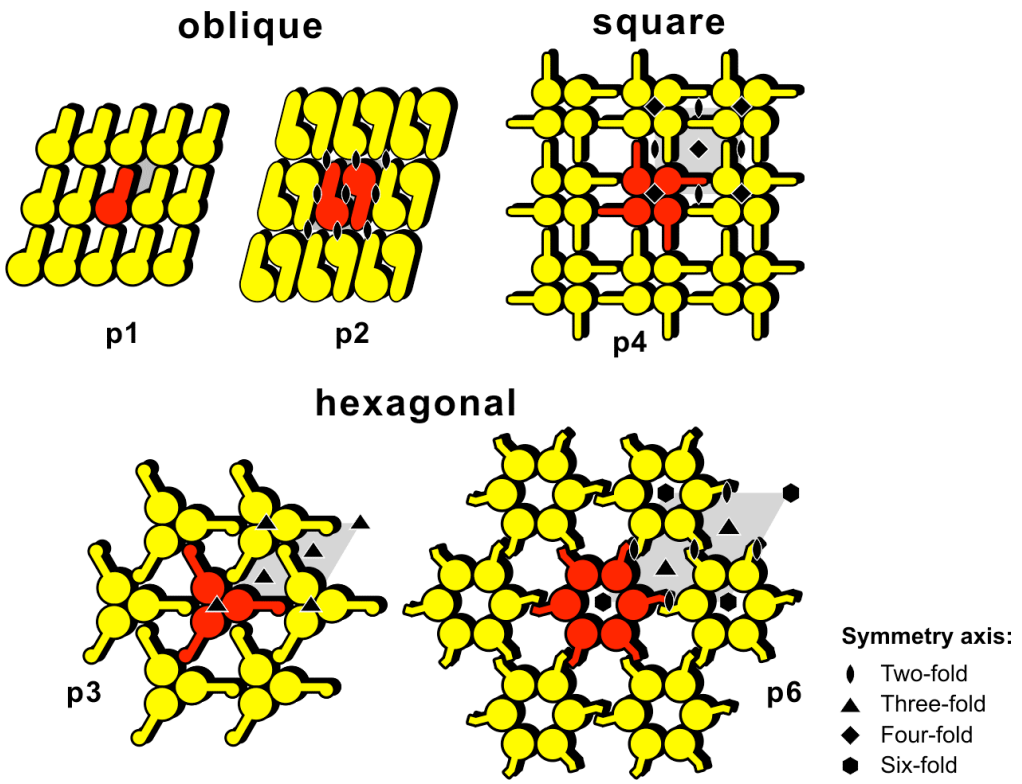

Fig. 3: Schematic drawing of S-layer lattice types. The regular arrays exhibit oblique (p1, p2), square (p4), or hexagonal lattice symmetry (p3, p6) (24).

1.1.2 Isolation and recrystallization

S-layer proteins can be isolated from the cell wall and disrupted into their constituent subunits by using chaotropic agents such as urea or guanidinhydrochloride (GHCl) breaking hydrogen bonds, by lowering or raising the pH or by applying metal-chelating agents like EDTA (3) (25). Removing the disrupting agent leads to reassembly of the S-layer subunits into monomolecular crystalline arrays. The reassembly of S-layers can occur on various solid surfaces such as polymers, silicon wafer, glass and metals as well as at interfaces like the air-water interface and lipid films (Fig. 4). The isolation and reassembly of recombinantly produced S-layer proteins, which are heterologously expressed in a host organism like *Escherichia coli*, can be performed after disintegration of the host cells (24).

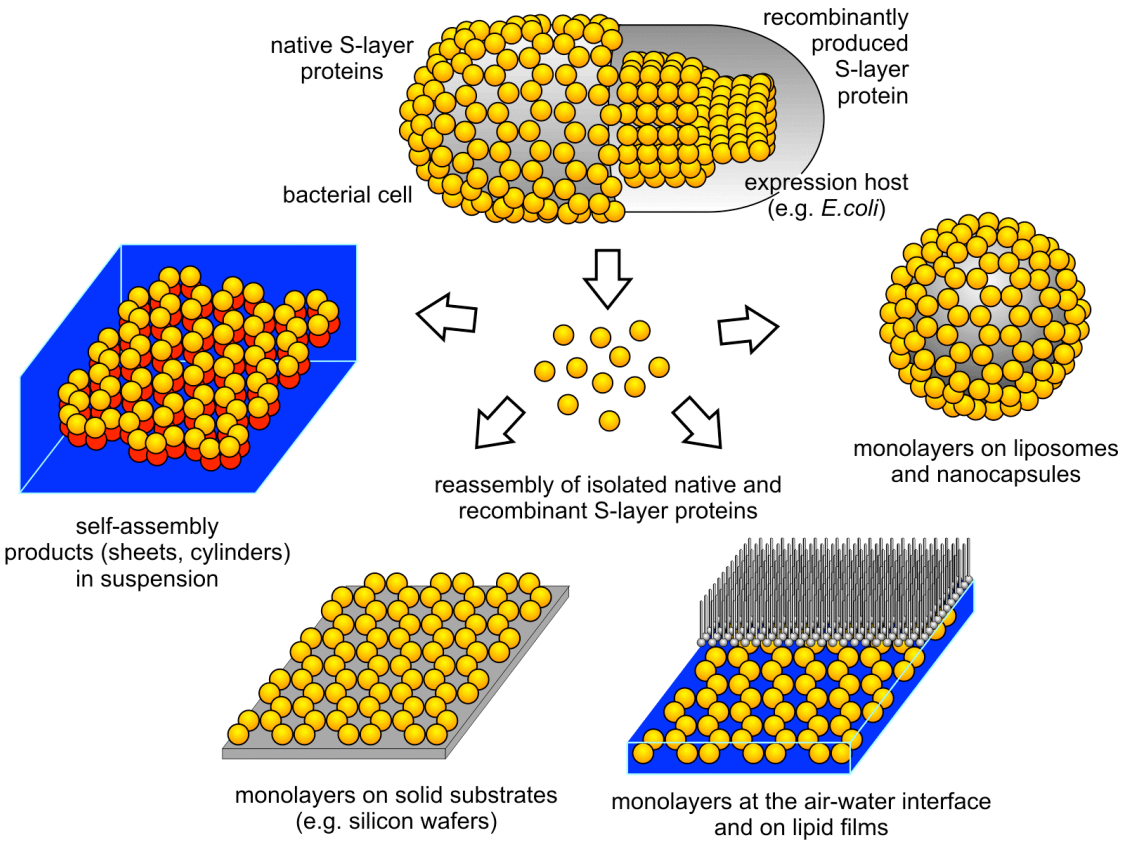

Fig. 4: Schematic of the reassembly of native and recombinant S-layer proteins into crystalline arrays. S-layer proteins perform self-assembly on solid supports, the air-water interface, planar lipid films, liposomes and emulsomes and build self-assembly products in suspension (24).

1.1.3 Antifouling properties of S-layer proteins

Antifouling properties of S-layer proteins were investigated first by Weigert and Sára in 1996 (26). In combination with microfiltration membranes the S-layer fulfilled its function as active filtration layer in the nanometer range. This setup was termed S-layer ultrafiltration membranes (SUMs). SUMs are isoporous structures with very sharp molecular exclusion limits and are manufactured by depositing S-layer-carrying cell wall fragments on commercial microfiltration membranes with an average pore size of approximately 0.4 µm. The studies of Weigert and Sára revealed that S-layer proteins covering microfiltration membranes result in regular porous structures with constant pore size providing indeed an antifouling layer. Via modification of the S-layer structure, the surface properties can be changed in terms of charge and polarity without influencing the crystalline SUM structure. In terms of the S-layer antifouling behavior, the best SUM performance can be achieved with hydrophilic uncharged surfaces (26).

1.1.4 S-layer fusion proteins

One big challenge in nanobiotechnology is the utilization of self-assembly systems in a technological aspect. For this reason, S-layer technology has been advanced by constructing functional S-layer fusion proteins (Fig. 5).

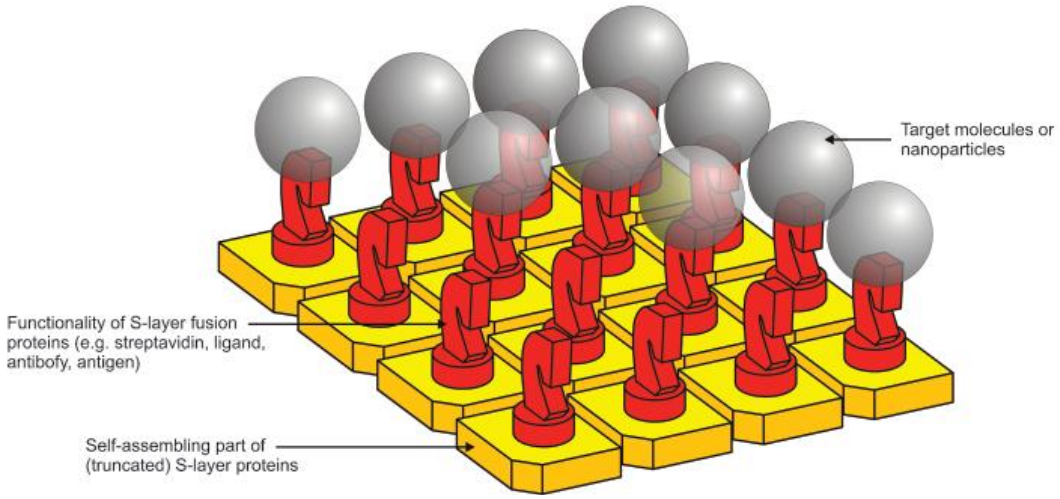

Fig. 5: Schematic illustrating self-assembled S-layer fusion proteins with target molecules or nanoparticles bound in defined spacing and orientation (24).

These recombinant S-layer proteins include the N-terminal cell wall anchoring domain, the domain for self-assembly and a C-terminal fused functional sequence. This construction mode belongs to the C-terminal S-layer fusion proteins containing the N-terminal SCWP-binding domain for a directed recrystallization on artificial supports precoated with thiolated SCWP (27). Most S-layer fusion proteins are based on the S-layer proteins SbpA of *Lysinibacillus sphaericus* CCM 2177, SbsB of *Geobacillus stearothermophilus* PV72/p2, SbsC of *G. stearothermophilus* ATCC 12980 and SgsE of *G. stearothermophilus* NRS 2004/3a which are cloned and expressed in *E. coli* (28).

Studies of the relationship between structure and function of the SbpA protein revealed that the deletion of 200 C-terminal amino acids interferes neither with its self-assembly properties nor with the formation of its square lattice structure (Fig. 6). Besides, the amino acid position 1068 was figured out to be located on the outer S-layer surface and was hence chosen as a fusion site for the production of chimeric SbpA proteins (29).

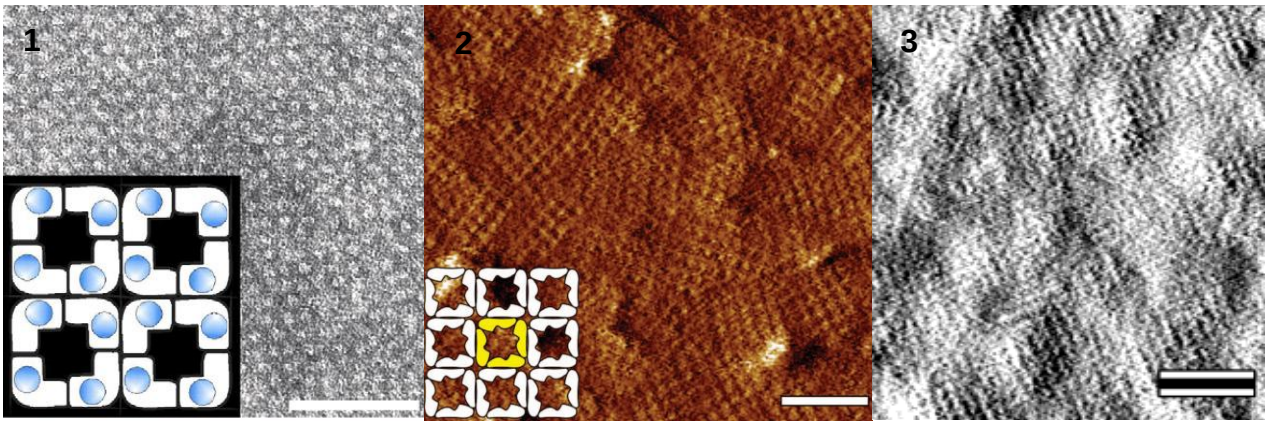

Fig. 6: Microscope images of recrystallized SbpA fusion proteins showing square lattice structure.
1) TEM image of a negatively stained preparation of the S-layer fusion protein LamA/SbpA; insert showing the square lattice symmetry (enzyme moiety in blue) (30). 2) AFM image of the fusion protein SbpA/F1 recrystallized on polystyrene slides; insert showing the square lattice symmetry (31). 3) AFM image of the fusion protein rSbpA$_{31\text{-}1068}$/cAb-Lys3 recrystallized on gold chips precoated with thiolated SCWP (32). Scale bars: 100 nm.

1.1.4.1 The S-layer fusion protein rSbpA/ZZ

The chimeric protein rSbpA$_{31\text{-}1068}$/ZZ, for simplifying reasons referred to as rSbpA/ZZ, presents the base on which this thesis is established. The rSbpA/ZZ protein encodes a C-terminally-truncated form of the S-layer protein SbpA of *L. sphaericus* CCM 2177 and two copies of the Fc-binding Z-domain and is heterologously expressed in *E. coli* HMS174(DE3). The construction of rSbpA/ZZ was first published by Völlenkle et al. 2004 (33). The rSbpA/ZZ protein features an Immunoglobulin G (IgG) affinity matrix, for it comprises two copies of the Fc-binding Z-domain which offers a synthetic analogue of the IgG-binding B-domain of protein A from *Staphylococcus aureus* (33). Staphylococcal protein A (SPA) plays an important role in immunology due to its specific interaction with the Fc part of immunoglobulins from many mammals (Fig. 7). Numerous immunological systems have been investigated and advanced using SPA as a reagent, implying immunoprecipitation techniques and double sandwich immunoassays. SPA is constructed of a cell wall binding region and five domains, C, B, A, D, and E, whereas C is located next to the cell wall. The molecular interaction between SPA and IgGs as well as the binding sites on the Fc part of IgG1, -2, and -4 are well explored. By X-ray analysis it was revealed that the SPA B-domain contains two contact sites interacting with the Fc part of IgG (33) (34).

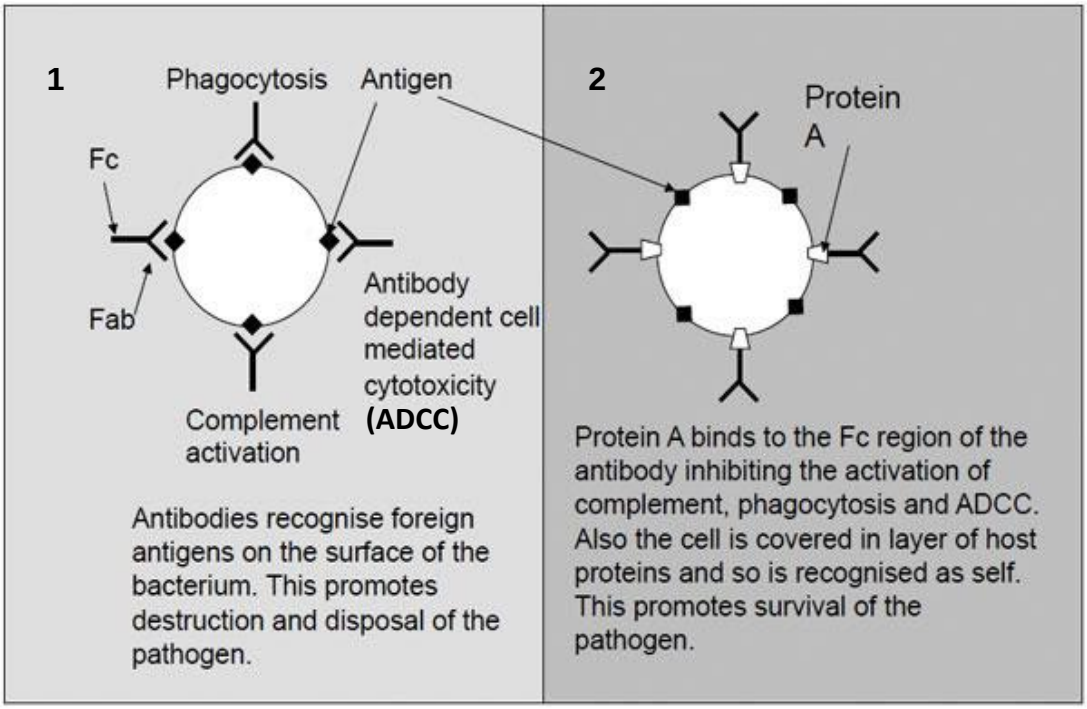

Fig. 7: 1) Schematic of immunogloblins bound to a bacterium and 2) to staphylococcal protein A (SPA). SPA binds immunoglobulins in non functional orientation inhibiting the destruction and disposal of the pathogen (35).

Based on this knowledge, Völlenkle et al. 2004 fused the synthetic Z-domain consisting of 58 amino acids and capable of binding the Fc part of IgG to the 3' end of the gene encoding the C-terminally-truncated form of the S-layer protein SbpA. After heterologous expression in *E. coli*, isolation from the host cells and purification, the S-layer fusion protein rSbpA/ZZ was recrystallized on solid supports such as gold and cellulose based microbeads precoated with thiolated SCWP. The accessibility of the fused ZZ-domains and their IgG-binding capacity (Fig. 8) could be proved by immunodot assays and Surface Plasmon Resonance (33).

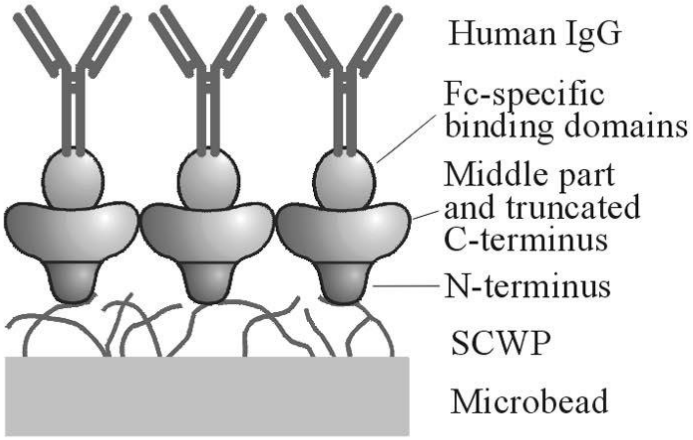

Fig. 8: Illustration of the immobilization of human IgG on rSbpA/ZZ (33).

1.2 Micro total analysis systems

1.2.1 General aspects of micro total analysis systems

Micro total analysis systems (μTAS) or also called lab-on-a-chip (LOC) have become more and more relevant due to their unique features which are, amongst others, reduction in space requirements, reagent and nutrition consumption and analysis time. μTAS devices apply laboratory conditions on a miniaturized scale and provide controlled surroundings for scientific measurements (Fig. 9) (36).

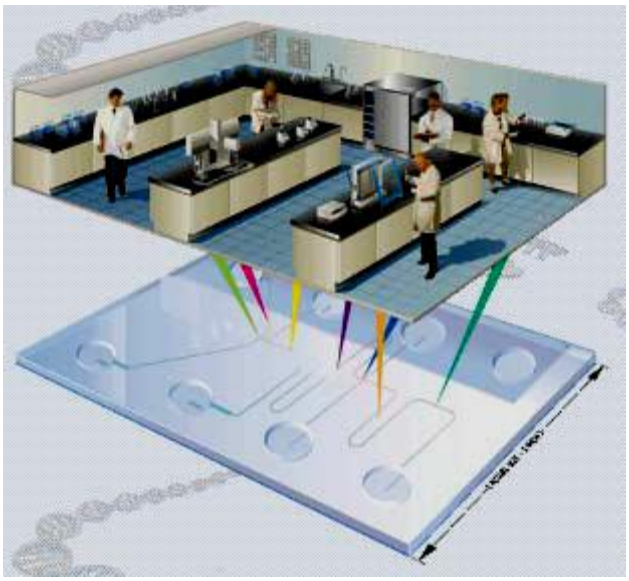

Fig. 9: Schematic of how laboratory functions are confined in a microchip (37).

Modern microfluidics can be traced back to the development of a silicon chip based gas chromatograph and an ink-jet printer in the late 1970s. However, the concept of LOC as it is known today was presented in the early 1990s. Since then, the field has considerably grown and branched off into many different areas. Important benefits of μTAS are the supply of nutrition, medium and oxygen at a controlled flow, highly laminar flow conditions and the miniaturization of analytical equipment. The scale of microfluidic devices is proportional to the in vivo cellular microenvironment and therefore well suited to the size of living cells (Fig. 10). The development tools for μTAS have been expanded recently by highly biocompatible soft lithographic techniques such as micro contact printing, replica molding, micro transfer molding and micro molding. Polydimethylsiloxane (PDMS) is a frequently used polymer for the fabrication of microfluidic devices due to its characteristics like biocompatibility, optical transparency, elasticity and gas permeability making it an optimal material for cell based devices. Besides, by microfluidic and laminar flow patterning the modification of culture

substrates and the selective delivery of various materials to specific substrate regions can be simply performed (36) (38) (39) (40).

SU8 is an epoxy-based UV-sensitive negative photoresist and offers an alternative to PDMS. It's a hard polymer and therefore represents a thermally and mechanically stable material. SU8 provides high biocompatibility and chemical inertness against most biological substances and is impermeable for small molecules (41) (42).

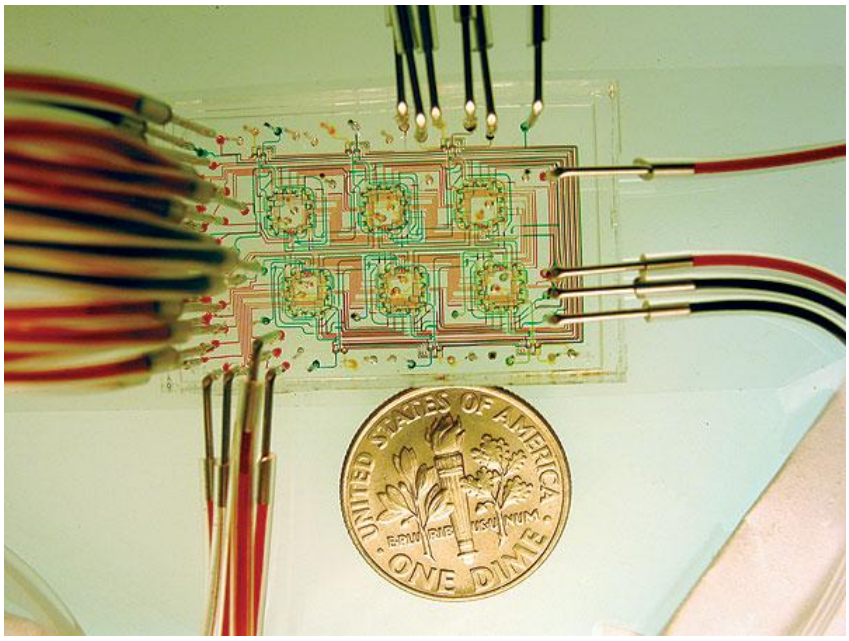

Fig. 10: Photograph of a microfluidic chemostat used to study the growth of microbial populations. The colors are dyes introduced to trace the channels (36).

1.2.2 Microfluidic fundamentals

In microfluidics a central focus lies on the considerations about fluids and flows. A fluid can be defined as a material that deforms under shear stress, is able to flow and has no rigid three-dimensional structure. Characterizing liquids, the three most important parameters are its density ρ, pressure of the liquid P and its viscosity η. The density is defined as the mass m per volume unit V:

$$\rho = m/V \qquad [1]$$

The viscosity is defined as the resistance that occurs when setting a liquid in motion, resembling an internal friction. This theory has often been described by a certain concept (Fig. 11); two solid plates are set on each other with a liquid film in between.

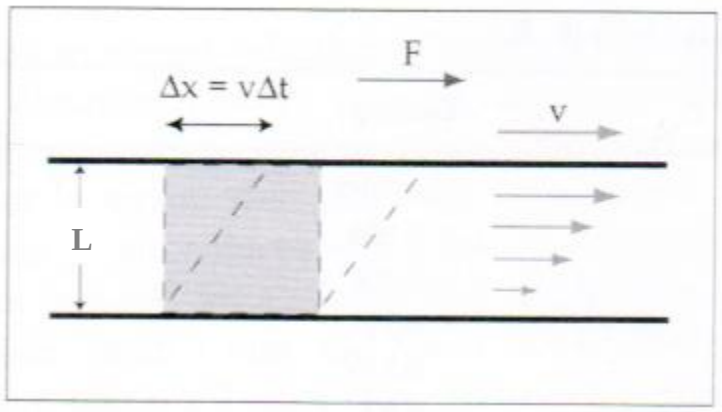

Fig. 11: Schematic of the two-plate model explaining fluid viscosity.
The upper plate is set in motion by force *F* resulting in velocity *v*.

The lower plate is fixed while the upper plate is set in motion by force *F* resulting in velocity *v*. The applied force *F* is acting on area *A* of the liquid interface which induces shear stress (*F/A*). The displacement Δx of the liquid surface at the upper plate relative to the liquid thickness is called shear strain ($\Delta x/L$), the shear strain per unit time *t* is called shear rate ($\Delta x/Lt = v/L$).

The viscosity η is defined as the ratio of shear stress to shear rate:

$$\eta = (F/A)/(v/L) \qquad [2]$$

Furthermore, the Reynolds number *Re* (non-dimensional) describes the tendency of a liquid stream to develop turbulence:

$$Re = lv\rho/\eta \qquad [3]$$

whereas *l* [m] stands for diameter of the geometry, *v* [m/s] for flow velocity, ρ [g/m^3] for density, and η [Pa s] for viscosity. Liquid flows with $Re < 1$ are defined as laminar while liquid flows with $Re > 2300$ are usually turbulent (43).

In addition, the Hagen-Poiseuille equation is applied when using a pressure gradient to drive a liquid through a channel containing a cylindrical diameter, called volume flow *Q:*

$$Q = \Delta P/R = (\pi r^4/8\eta L)\Delta P \qquad [4]$$

The formula for rectangular geometries is:

$$Q = \Delta P/R = (wh^3/12\eta L)\Delta P \qquad [5]$$

The continuity equation describes flow behavior in channels with variable cross sections and states. The product of cross sectional area and flow velocity is constant:

$$A_1 v_1 = A_2 v_2 = const. \quad [6]$$

Unless indicated differently, all information for this section was retrieved from Geschke et al. (44).

1.2.3 Fabrication of microfluidic devices with PDMS and SU8

In this thesis, a soft lithographic method as described by Yeon and Park (2007) was used for the PDMS-fabrication of microfluidic devices as depicted in Fig. 12 (40). First, the SU8 photoresist is developed on a silicon wafer by exposure to UV light and the desired pattern is generated by the photo mask. Further, the patterned mold is used as a master for molding an elastomer such as PDMS. After curing and cutting the PDMS mold, both sides of the elastomeric PDMS structure are bonded on a glass substrate by plasma treatment. Finally, ports for in- and outlets are attached to complete the fabricated microfluidic device.

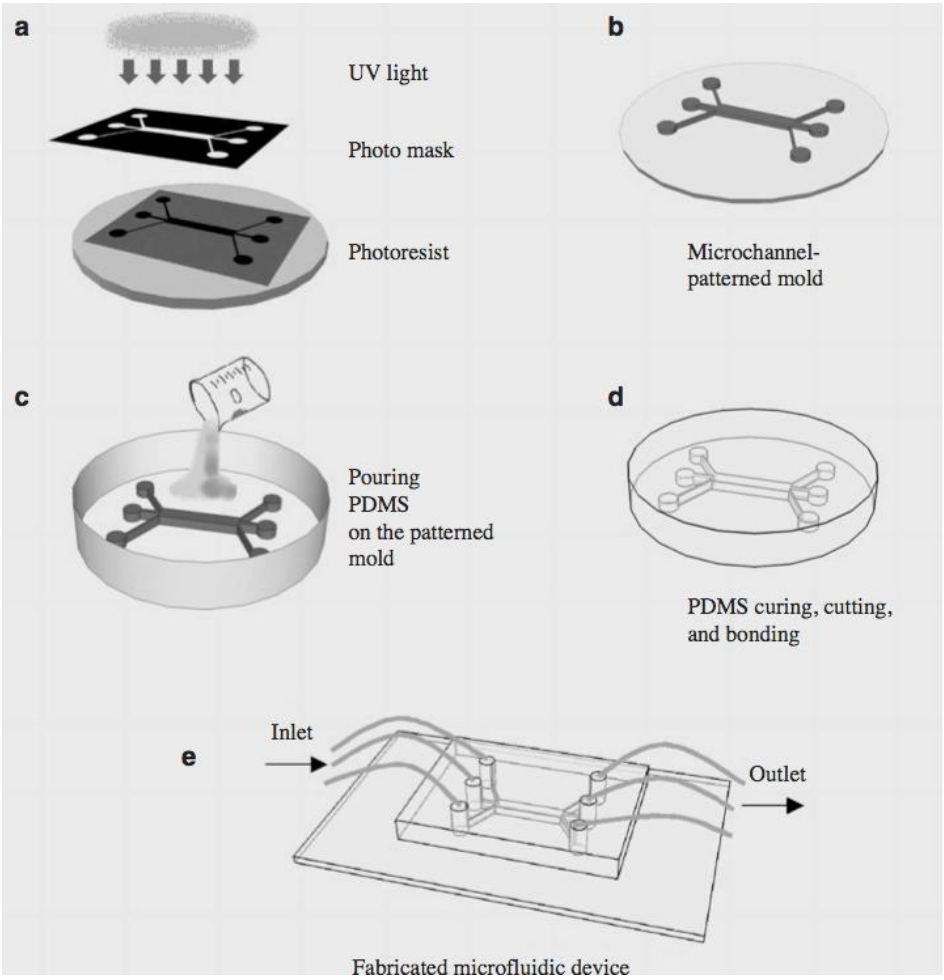

Fig. 12: Schematic of microfabrication procedures of a microfluidic chip.
UV photolithography process (a) resulting in a master mold (b) for PDMS replica molding (c), which is cured, cut and bonded (d) to result in a fabricated microfluidic device (e) (40).

1.2.4 Air bubbles in microfluidics

Generally, infiltration or enclosure of air bubbles belongs to the most unwanted events when dealing with microfluidics in combination with cells. Due to the presence of air, whole experiments can be ruined by increasing shear stress and therefore affecting the viability and morphology of biological samples (45). The introduction of such bubbles can have various reasons. Amongst others, incomplete priming or defects of the microfluidic system can lead to arising of air bubbles from residual air. The fluid flow is obstructed then and cells get killed at the liquid-gas interface. One efficient method to prevent air bubble formation is to prime the system under high pressure >5 psi; under such conditions residual air collapses within the microchannel (Fig. 13) (46). A further rather simple way is to carefully flush the system with low surface tension liquids like ethanol or isopropanol to rinse the air bubbles out of the microfluidic device (47).

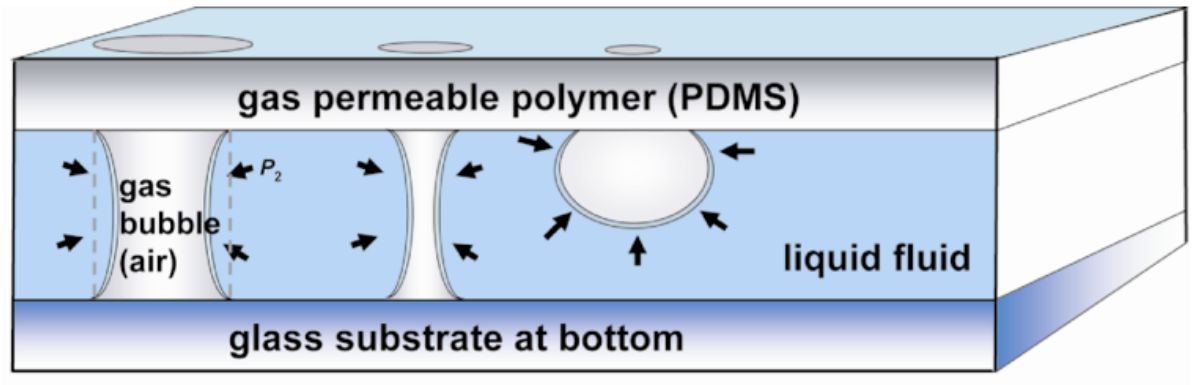

Fig. 13: Schematic of removing trapped air bubbles using a pressurized microchannel with a PDMS ceiling (47).

1.3 Microfluidic rare cell capture

Cell isolation, fractionation and capture from suspensions cover a wide application range from bacteria detection to cancer cell enumeration. Flow cytometers, immunomagnetic separators and other macro-sized sorting equipments have been studied extensively concerning their benefits and limitations compared to the abilities of microfluidic devices. In terms of microfluidic cell capture, the focus lies on devices and techniques for the analysis of suspension cells that are characteristically found at low concentrations. Such devices have great relevance in environmental pathogen detection and cancer cell isolation from patient blood samples. However, still many of the methods described in literature only exist as proof-of-concept studies. There exist two major classifications of microfluidic approaches: electrokinetic and non-electrokinetic methods (48).

1.3.1 Electrokinetic methods

Electrokinetic methods utilize electric fields to put cells in motion. In microfluidic devices, electrophoresis and dielectrophoresis are the two most common electrokinetic techniques for manipulating cells. Due to the application of an electric field on the net free charge of a particle, electrophoresis refers to net migration. For a cell's net charge is often not specific enough to differentiate within a cell mixture, electrophoresis is not appropriate for rare cell capture contrary to dielectrophoresis. Dielectrophoresis (DEP) refers to the net migration of polarized particles due to interactions with an electric field gradient. DEP is dependent on the electrical properties of cell wall, membrane, and cytoplasm. Further, the DEP force is a function of cell size, electrical properties of the fluid medium, and magnitude and frequency of the applied electric field. The dependence on this wealth of parameters makes DEP to a valuable tool for sorting different rare cell types. A classification into two regimes relates to DEP response: particles more polarizable than the medium cause positive DEP results attracting the particles to stronger field regions; contrary, particles less polarizable than the medium induce negative DEP response repelling the particles from stronger field regions. The DEP force frequency switching between the two regimes is termed "crossover frequency". The selection of a frequency regime enables the attraction of one cell type to the electrodes (positive DEP) while repelling another cell type (negative DEP) which finds application in DEP field flow fractionation (DEP-FFF) (Fig. 14) (48) (49).

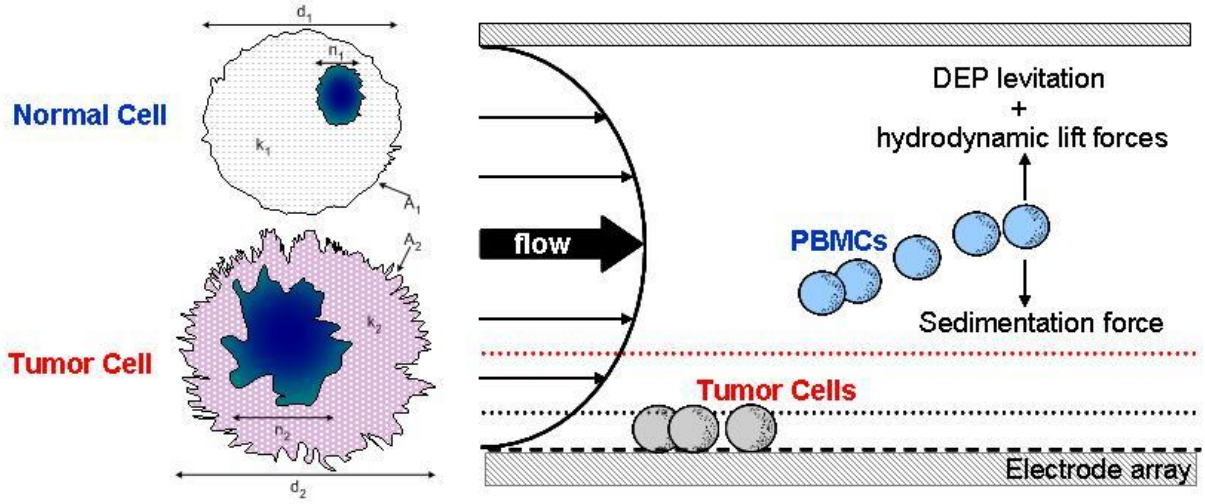

Fig. 14: A microchannel flow field to isolate circulating tumor cells using DEP-FFF.
Rare circulating cells such as circulating tumor cells (CTCs) have inherent differences in morphology and dielectric properties from peripheral blood mononuclear cells (PBMCs). In DEP-FFF, cells are repelled from or attracted to a charged electrode at the channel bottom. Different flow rates relative to the distance from the electrode are used for fractionating specific cell types. Electric fields at lower level pull CTCs towards the channel floor while PBMCs are carried away by the eluent (49).

1.3.2 Non-electrokinetic methods

Non-electrokinetic methods focus on cell isolation, capture, or fractionation from a suspension by sorting techniques such as antibody capture, size-selective sorting, streamline focusing and sheath flow. Further, each sorting method is subdivided into cell separations of interest: fractionation of blood cells, cancer cells, other mammalian cells and prokaryotes and viruses. The focus of blood cell fractionation lies on isolation of cell types native to circulation, studying most the capture or elimination of white blood cells (WBCs). WBCs are of great interest in many diagnostics and studies about disease progression, e.g. in HIV. Their concentrations are low; around 1 to 1000 compared to red blood cells (RBCs). In terms of isolating cancer cells, studies focus on the capture of circulating tumor cells (CTCs) which can be found in the circulation of cancer patients. CTCs are about 10^6 times rarer than WBCs, making their capture to a particular challenge (48).

1.3.2.1 Cell capture via antibody immobilization or aptamer chemistry

In this thesis, the focus lies on modifications of microfluidic devices based on biochemical interactions to enhance rare cell capture and fractionation. These techniques belong to immunocapture and are frequently used in the isolation of cells, viruses and proteins from suspension. Most techniques are based on the chemical immobilization of antibodies inside the microfluidic channel (50) (51) (52). Immunocapture provides an opportunity to separate cells in a viable state from a suspension with extremely high specificity and therefore presents

an analogue to microscale affinity chromatography for cells containing unique markers or characteristics (48).

1.3.2.1.1 Blood cell fractionation – capture of T-lymphocytes

The progress in microfluidic devices for T-lymphocyte counting has become increasingly important during the last years, for CD4+ T-lymphocytes play a large role in HIV diagnostics and microfluidics present a great hope for point-of-care devices (53) (54).

CD4+ T-lymphocytes, also called CD4+ T-cells, are a specific WBC population and express the CD4 molecule. They play a major role in coordinating the body's immune response, e.g. by helping B-cells to produce antibodies. HIV uses CD4 molecules on the lymphocyte surface as primary targets. The consequence of CD4+ T-cell destruction by HIV is the loss of HIV-specific immune response, recall antibody response, and non-specific immune response in the AIDS stage. Therefore, counts of CD4+ T-cells are essential biological indicators regarding the process of managing HIV-infected subjects (55).

Amongst others, Cheng at al. developed several microfluidic devices for CD4 counting of unprocessed, unlabeled whole blood (50) (51) (54). The specific isolation of CD4+ T-cells is based on cell affinity chromatography via a chemically immobilized CD4 antibody and operates under differential shear flow. The capture and enumeration process of CD4+ T-cells in a sample of whole blood is described in Fig. 15. At first, a Hele-Shaw chamber was designed to study the dynamics of lymphocyte attachment and investigate the optimal shear rates. In a Hele-Shaw chamber the shear stress along the chamber axis decreases linearly with the chamber length while the chamber width increases. Therefore, multiple shear rates can be obtained in one flow chamber without varying the inlet flow rate (56). The other types of devices were PDMS fabricated straight flow channels providing a constant shear stress along the channel length. The definite cell capture and counting experiments were performed operating with the optimal shear stress determined from the Hele-Shaw experiments (50) (51) (54). In terms of analysis, the described setup has been recently combined with electrical impedance sensing (57).

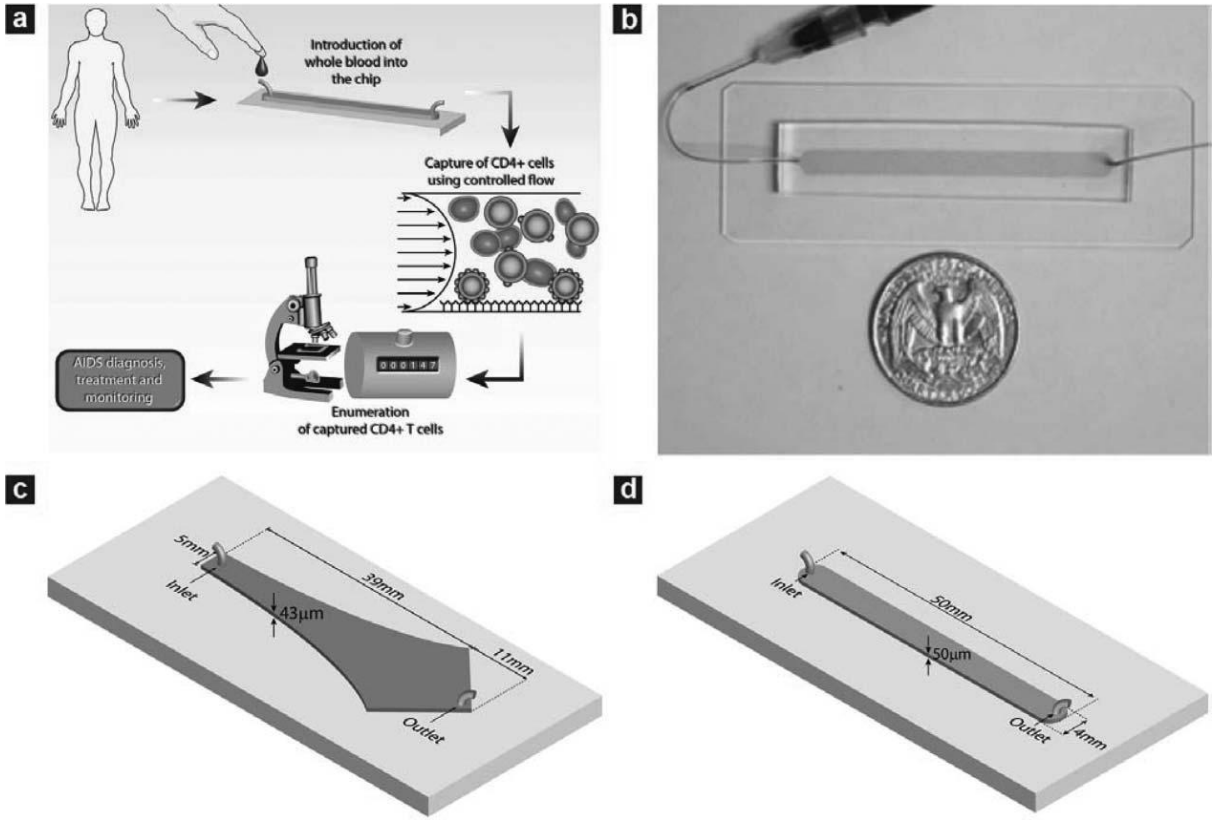

Fig. 15: Microfluidic devices used in the CD4+ T-cell counting studies.
(a) Schematic explaining the operating procedure of the CD4 counting device: 10 µL of whole blood were injected into the microchip at a controlled flow rate. After capture, unbound cells were rinsed off the chamber and all captured cells were counted within the microchip using an optical microscope to obtain CD4 counts. (b) A linear microchamber as cell counting device: PDMS fabricated devices with one inlet and one outlet were bonded to glass slides to create closed chambers and functionalized with a specific antibody for target cell capturing from whole blood. (c) Design of the Hele-Shaw device providing a linear variation of shear stress along its central line to screen the optimal shear stress for cell capture. (d) Geometry of the linear cell count device. Capture and enumeration of the target cells was performed under the Hele-Shaw-optimized shear stress (50).

1.3.2.1.2 Capture of cancer cells – the influence of microfluidic geometry

Many microfluidic devices take advantage of the 3D structure of channels to increase the surface area available to be coated with the antibody or aptamer of choice (48). For instance, DNA aptamers within an S-shaped microfluidic device were used to capture cancer cells (Fig. 16) (58). Further, research work on silicon nanopillars indicated that the topology of the microdevice itself may contribute greatly to the efficiency of rare cell capture. Cancer cells have also been captured from blood-based systems; nickel micro-pillars were used to immobilize functionalized superparamagnetic beads to create a capture zone within their microfluidic devices. In other studies, cell margination was observed along the walls of linear channels when working with whole rabbit blood. This phenomenon was no longer seen when straight-walled channels were exchanged for sinusoidal ones. In combination with anti-epithelial growth factor receptor (EpCAM) antibodies, immortalized breast cancer cell capture

efficiencies of 97% were achieved. The device was translated to the capture of model prostate cancer cells spiked in PBS using anti-prostate specific membrane antigen aptamers with an efficiency of 90%. While the prior studies worked with model cell lines spiked in buffer solution or blood systems, this method has also been used for cancer patient blood samples. Recently, computational modeling was used to design micro-pillar arrays such that cell-antibody interactions were size-dependent (48).

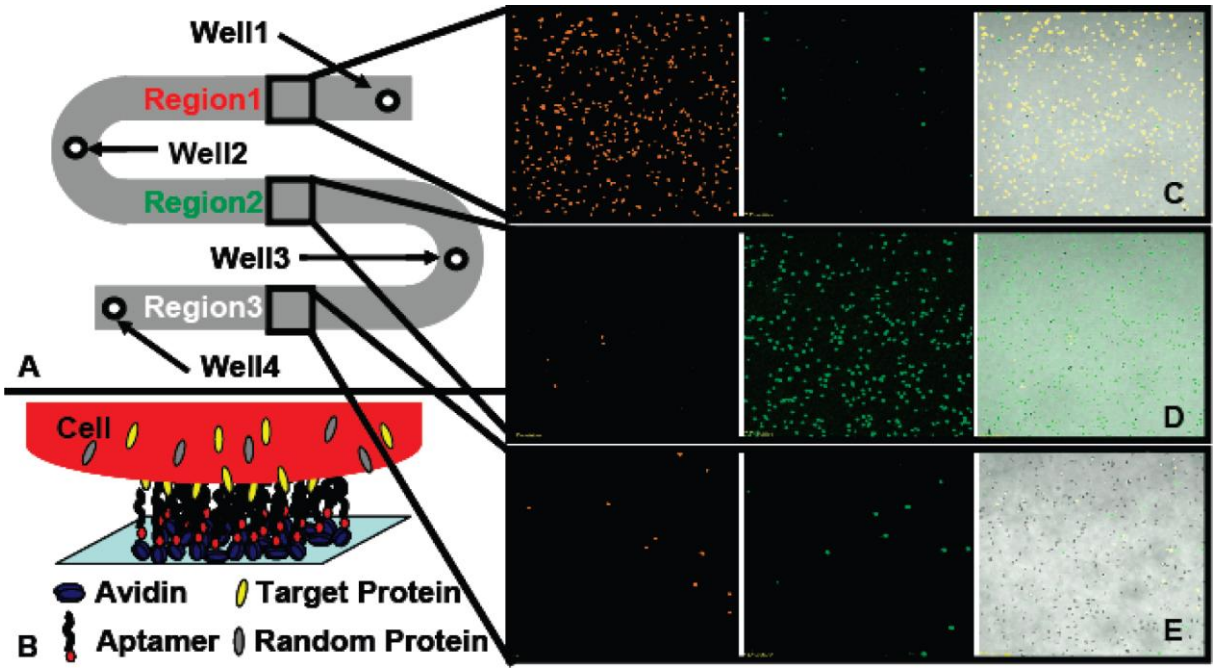

Fig. 16: Microfluidic device and detection of three different cancer cell lines.
(A) Schematic of a microfluidic device with three regions for aptamer immobilization and four wells for sample injection. (B) Aptamer immobilization scheme; avidin adsorbed to the glass surface and biotinylated aptamers capturing a cell via specific molecular interactions. (C-E) One location within each aptamer coated region showing red fluorescent images, green fluorescent images, and double overlays of the fluorescent channels (58).

1.3.2.1.3 Isolation of other mammalian cells

Various microfluidic devices were used to selectively isolate endothelial cells (ECs) and smooth muscle cells (SMCs) from suspension. The devices were coated with peptides targeted to ECs and SMCs investigating the binding to target cells as a function of shear stress. Using these peptide sequences, ECs and SMCs were differentially isolated from homogeneous and heterogeneous suspensions with purities of 86% and 83%, respectively. Further, the feasibility of peptide-based capture systems by using a 3-stage isolation system to deplete heterogeneous suspensions of ECs, SMCs and fibroblasts was demonstrated. Using this system, it was able to achieve 96% to 99% depletion of the three different cell types with over 97% viability of non-immobilized cells (48).

1.4 Analytical techniques for microfluidic devices

1.4.1 Pathogen sensing in microfluidic devices

Rapid detection and identification of microorganisms play an important role in fields ranging from clinical diagnostics to biological warfare agents. Health care systems would greatly benefit from faster diagnosis reducing health care costs, while simultaneously providing better epidemiological data that can be used for infectious disease modeling (59). Furthermore, since most centralized laboratories are limited to large cities, near-patient testing using point-of-care devices has become increasingly important. Therefore, robust and portable diagnostic devices capable of rapidly providing information on pathogens will also help reduce mortality rates, hospitalization and timely isolation in case of infectious pathogens. Portable medical diagnostic tools are of great importance in developing countries where more than half of the deaths are attributed to infectious diseases (60) (61). Virtually, all analytical detection methods have been successfully integrated or coupled with LOC devices, including optical detectors, electrochemical detectors, magneto-resistive sensors, acoustic and mass spectrometric as well as nuclear magnetic resonance ones (62). However, optical sensors are probably the most popular in pathogen analysis due to their selectivity and sensitivity (63). For instance, the application of photodiodes allows making portable LOC systems for the integration of optical detectors with microfluidics; amongst others, a microfluidic ATP bioluminescence sensor for the detection of airborne microbes using commercial available photodiodes has been reported (64). Other optical methods include fluorescence, chemiluminescence, bioluminescence and Surface Plasmon Resonance (SPR) biosensors. Alternative detection methods for pathogen sensing include the application of silver dots for direct optical density measurements using a scanometric reader, or biosensors using resonance light scattering techniques based on nanometer-sized metallic particles (mostly gold) covalently linked to antibodies. These metal colloidal particles radiate energy in the form of scattered light when illuminated by a white light source (62).

1.4.2 Optical sensing systems for microfluidic devices

Initially, the analytical improvements associated with the scaling down of the size should be the most significant benefit of LOC devices. Though, the detection concerns arise when sensing systems are miniaturized. The volume reduction decreases the number of analytes making their detection more difficult. Therefore, the two main factors in detection methods for microfluidic devices are sensitivity and scalability to smaller dimensions. Electrochemical

detection (e.g. conductivity, potential) does not fulfill all these conditions, where sensitive portable systems are required. Hence, there is an increasing interest to couple and/or integrate optical components to microfluidic devices. The optical components used in these detectors are mainly light-emitting diodes (LEDs) or laser diodes as light sources, optical fibers, gradient refractive index lenses, and diffractive elements. These are assembled into compact detectors to develop a portable instrumentation based on microfluidic devices. The coupling/integration of optical sensing systems to microfluidic devices is referred to as "off-chip"/"on-chip" approach (63).

1.4.2.1 Coupling of optical detection systems: off-chip approach

Macro-scale optical detection, especially spectrometric detection is common because there is a wide range of applications, e.g. absorbance, fluorescence and chemiluminescence. In order to couple these macro-scale detection into micron-sized detection areas, pinholes are used at focus points along the optical path or optical fiber. The advantages of this approach are very low levels of background signal that can be combined with very sensitive photon detection techniques, such as photomultiplier tubes (PMTs) and charge-coupled devices which in turn, result in very low detection limits. Further, the development of a wide range of intense LEDs and photodiodes that can be well coupled directly to microfluidic devices can easily be realized. UV/VIS absorbance detection is the most widely used detection method in common macro-structure sensing systems. However, despite its very wide range of possible applications, the small dimensions of a microchip channel pose a severe problem for sensitive and reliable absorbance measurements. Incorporating optical fibers into the microchip is a simple approach minimizing the number of required optical components. Fluorescence detection is still the most widely used optical method for microsensing systems, due to its superior selectivity and sensitivity (63) (60). Although a variety of excitation sources are available, laser-induced fluorescence (LIF) is most easily adapted to the dimensions of microchips (Fig. 17, left). The coherence and low divergence of a laser beam makes it easy to focus on very small detection volumes and to obtain very high irradiation, resulting in one of the lowest detection limits of any detection system. Chemiluminescence (CL) as a detection method for microsensing systems has the advantage of high sensitivity, low detection limits and simple instrumentation compared with other spectrophotometric techniques, due to the exclusion of an external light source (63) (65). An extremely simple CL setup has been developed by directly monitoring a microchip onto PMTs without using any optics or filters (Fig. 17, right) (66).

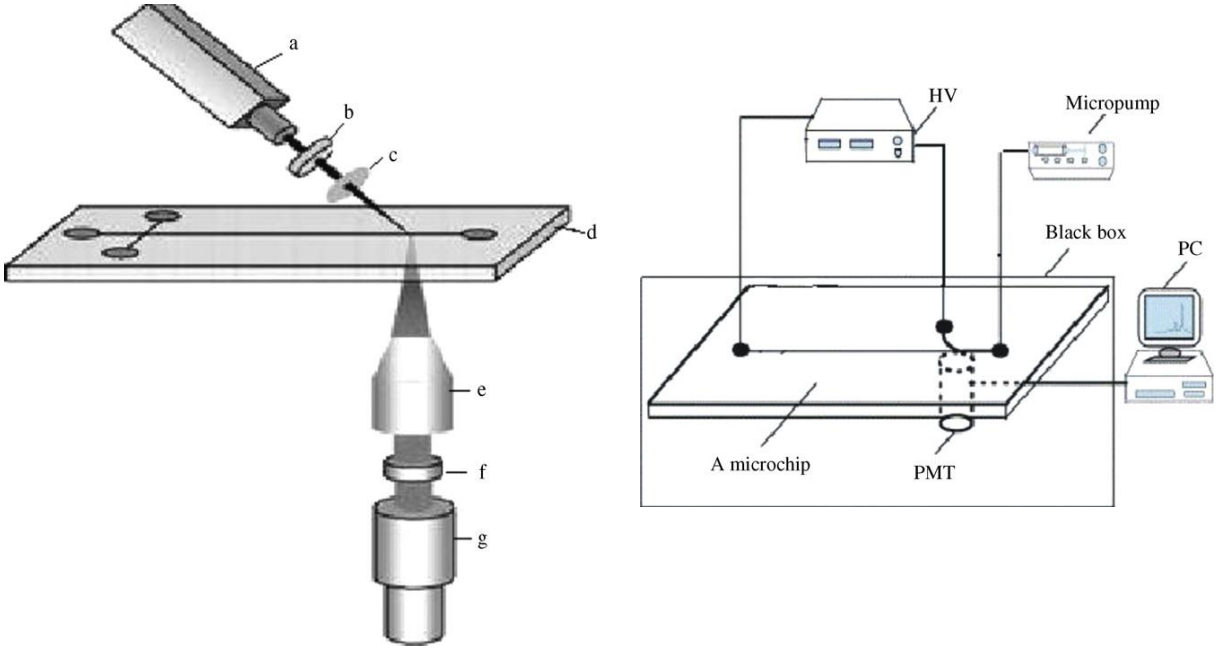

Fig. 17: Common setups used for LIF and CL detection.
Left:(a) laser; (b) excitation filter; (c) focusing lens; (d) microchip; (e) objective for collimated emission; (f) emission filter; (g) PMT detector. Right: Schematic representation of the instrumentation for a simple CL setup (63).

1.4.2.2 Integration of optical functions: on-chip approach

The integration of optical components or functions in a microfluidic platform, that should be able to perform all chemical functions and detection in a single device, requires increased integration of not only fluidic but also electrical or other types of elements. This method can be classified as on-chip approach. The microelectromechanical systems' (MEMS) world has demonstrated the integration of mechanical and electrical functionalities into small structures for diverse applications. Micromachining technologies have traditionally been silicon-based, since it makes the combination of mechanical and electrical functions in single devices possible. In general, silicon and other semiconductor materials also exhibit active optical properties, such as the ability to absorb and emit light. Direct electronic optical sensors like the silicon photodiode operate by converting absorbed photons directly into electronic carriers which are ultimately detected. Alternatively, many semiconductors and combinations thereof form the base of laser diodes and LEDs, a class of devices producing light in different wavelength regions from the blue to the near infrared. From both the material and technological point of view, the integration of optical functions (passive or active) into a microchip is very promising. However, the existing devices in the on-chip approach are generally still in its infancy (63). For instance, integrated optical waveguide technology has

been used for the fabrication of a miniaturized optical detection system for sensing in microchannels. The design allowed the implementation of both absorption and fluorescence measurement methods (67). Further, individual functional components were assembled to higher integrated devices. Five different components (liquid dye laser, waveguides, fluidic channels, measurement cuvettes, and photodiodes) were monolithically integrated on one substrate (one layer of SU8 polymer) as well as photodiodes were embedded in the silicon substrate (68) (Fig. 18, 1). In another microfluidic device, thin-film organic photodiodes have been applied as integrated optical detectors for microscale chemiluminescence. Simple detector fabrication, based on layer-by-layer vacuum deposition, allows facile integration with planar chip-based systems. Fig. 18, 2 shows an optoelectronic detection system composed of a disposable biosensing element and a hand-held controller (69).

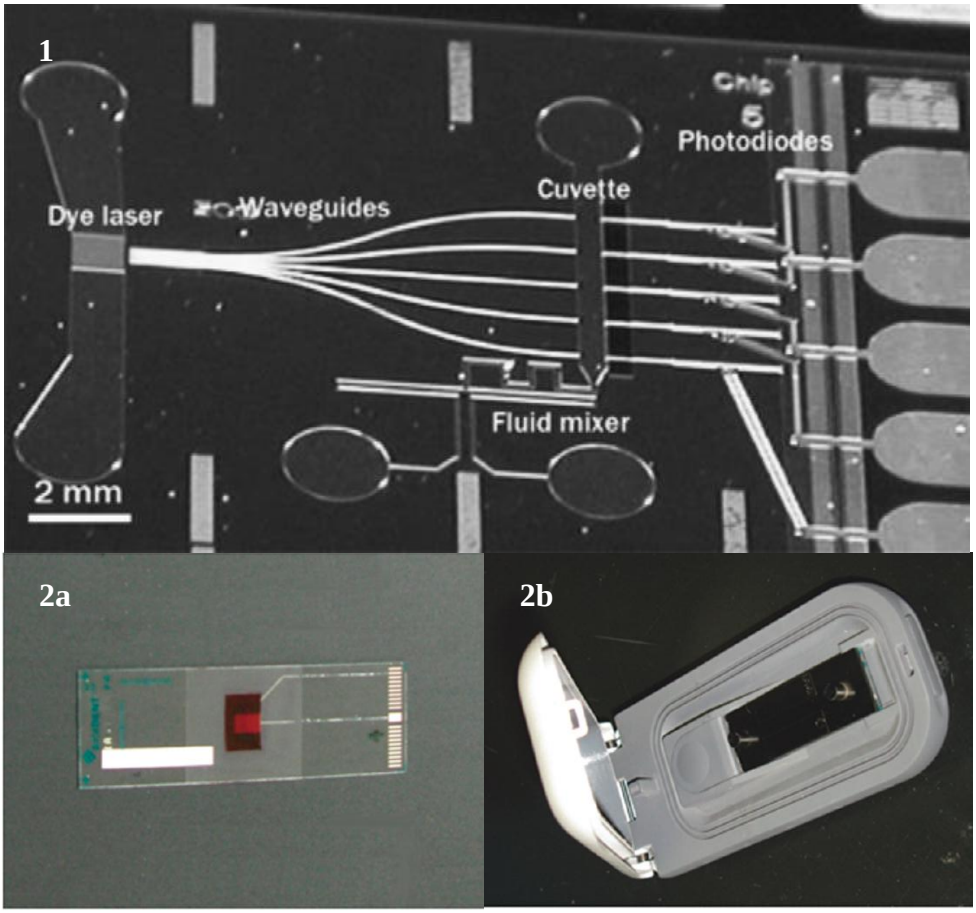

Fig. 18: Photographs of two on-chip approaches and a hand-held controller.
1) LOC device with integrated microfluidic dye laser, optical waveguides, microfluidic network, and photodiodes (68). 2a) A glass sensor slide containing a centrally located printed OPD and the associated electrodes. 2b) A hand-held controller that can be connected to any computer using a USB interface (69).

2 Aim of the thesis

The S-layer fusion protein rSbpA/ZZ providing an IgG-affinity matrix offers a challenging approach for the immobilization of IgG-based antibodies and the capture of rare cells from suspension as well as from whole blood in static and fluidic manner. Microfluidic devices have outstanding benefits such as small volume requirements, highly laminar flow conditions, and cost effectiveness and are easy to handle in terms of point-of-care diagnostics in developing countries. The purpose of this thesis was to establish a CD3-affinity matrix based on the S-layer fusion protein rSbpA/ZZ in order to capture CD3-lymphocytes (Jurkat cell line) from suspension in microfluidic devices. PDMS and SU8 microchannels were statically modified with the S-layer fusion protein and a specific CD3 antibody. The investigation of the CD3-affinity matrix and its antifouling properties, the establishment of cell capture approaches and the improvement of the microfluidic setup present the main challenges of this thesis. Further, a detection system was required in order to quantify the amount of captured cells and establish a calibration system for cell capture experiments. Throughout this research, several characterization and detection methods were conducted, such as atomic force microscopy, Surface Plasmon Resonance and light scattering.

3 Materials and Methods

3.1 S-layer proteins

All S-layer proteins used in this thesis were produced at the Department of NanoBiotechnology (DNBT), University of Natural Resources and Life Sciences, Vienna.

3.1.1 S-layer protein SbpA

The S-layer protein SbpA was isolated from *L. sphaericus* CCM 2177 after the procedure described in Egelseer et al. 1998 (70). All SbpA protein stock solutions with an average concentration of 1 mg/mL were kindly obtained from Jacqueline Friedmann at DNBT.

3.1.2 S-layer fusion protein rSbpA/ZZ

The S-layer fusion protein $rSbpA_{31-1068}$/ZZ was produced by genetic modification of SbpA as described in Völlenkle et al. 2004 (33). After heterologous expression in *E. coli*, the fusion protein was isolated, purified and lyophilized following the standard procedure (33). To obtain rSbpA/ZZ protein subunits, 2 mg lyophilized rSbpA/ZZ protein were solved per 1 mL 5 M GHCl (guanidinhydrochloride) for 20 minutes at room temperature. The dialysis of the rSbpA/ZZ protein solution was carried out in total for 180 minutes in three steps of 30, 60 and 90 minutes, whereas each dialysis step was conducted against 3 L of renewed distilled water. After dialysis, the protein concentration was determined by UV-measurements at 280 nm, adjusted to a stock solution of ~1 mg/mL with distilled water and stored at 4°C. All rSbpA/ZZ protein samples were kindly obtained from Andreas Breitwieser at DNBT.

3.1.3 Recrystallization of S-layer proteins

Throughout this thesis, the S-layer proteins SbpA and rSbpA/ZZ were recrystallized on several surfaces generally performed under the following conditions: the S-layer protein stock solution was diluted 1:15 in TRIS-buffer solution (10 mM $CaCl_2$ in 0.5 mM tris(hydroxymethyl)-aminomethane, pH 9) and applied to a support such as gold (precoated with thiolated SCWP as described in Völlenkle et a. 2004 (33)), PS (Polystyrene), glass, PDMS or SU8 and incubated over night at 4°C. After the recrystallization procedure, the samples were washed and stored in TRIS-buffer solution at 4°C until their usage.

3.2 Atomic Force Microscopy

In order to visualize the lattice structure of the S-layer fusion protein rSbpA/ZZ recrystallized on various supports such as gold, glass and SU8, atomic force microscopy (AFM) was applied.

3.2.1 Fundamentals of AFM

Atomic force microscopy (AFM) (71) is a valuable tool for studying biological molecules. AFM gives high-resolution information of one nanometer of the topography of biomolecules as well as of physical properties and interaction forces. Amongst others, proteins, membranes, membrane bound proteins and nucleic acids have been studied using AFM. The main principle is to measure forces acting between a fine tip placed on a micrometer-sized cantilever and the sample of interest. These forces are caused by attraction and repulsion resulting from interactions between tip and sample which lead to positive or negative bending of the cantilever. A micro-machined cantilever and a special tip form the probe, the part interacting with the sample. Often a silicon nitride (Si_3N_4) tip on a V-shaped cantilever is used. The cantilever's physical and geometric properties determine its spring constant, which is used to convert the deflection angle of the cantilever into a contact force; a laser beam gets reflected off the back of the cantilever to a position sensitive photodetector (PSPD) consisting of four photodiodes. To produce a three-dimensional picture of the sample surface, the cantilever deflection is recorded and translated into the sample height while the tip is scanning over the sample. Another scanning method is to move the specimen stage by a piezoelectric positioner while the tip remains constant. In this case, the three-dimensional movements of the piezoelectric positioner are converted into a height image. Ultrasensitive piezoelectric positioners keep the resulting cantilever deflection constant by adjusting the z-position; the force is measured and is used in a feedback loop for the topographical image generation of the sample. AFM can be performed in two different modes: contact mode and non-contact mode. The principle of AFM is shown in (Fig. 19) (72) (73).

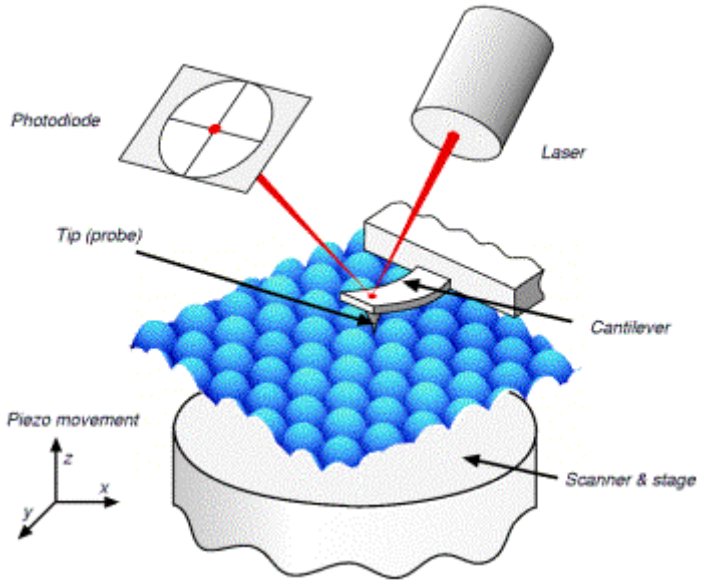

Fig. 19: Atomic Force Microscopy (AFM) principle.
A laser beam emitted from a light source meets the back of the cantilever and is reflected to a position sensitive photodetector (PSPD) consisting of four photodiodes translating the position signal into the angle deflection and further into an image (74).

3.2.2 AFM imaging of recrystallized rSbpA/ZZ

For AFM imaging of the rSbpA/ZZ lattice, the Nanoscope IIIa (Veeco Instruments, USA) was used in contact mode under liquid (100 mM NaCl) with oxide-sharpened silicon nitride cantilevers (NanoProbes, Digital Instruments) with a nominal spring constant of 0.7 N/m. The surfaces were scanned at 1-3 Hz on areas ranging from 10 µm down to 500 nm at constant load.

3.3 Enzyme linked immunosorbent assay

To investigate the S-layer fusion protein rSbpA/ZZ as an affinity matrix binding IgG to its ZZ-sequence, enzyme linked immunosorbent assay (ELISA) experiments were performed. Amongst others, the affinity of rSbpA/ZZ to human IgG was compared to the chemical immobilization of human IgG to the S-layer protein SbpA. The goal was to figure out the optimal IgG concentration to achieve saturation between rSbpA/ZZ and IgG.

3.3.1 Fundamentals of ELISA

ELISA is an immunoassay utilizing enzyme-conjugated antibodies, with antigens or antibodies bound to a solid support. The assay measures changes in enzyme activities proportional to the antigen or antibody concentration involved in the underlying immune reactions (75). The first published ELISA system is based on the principle of an immunoassay with an enzyme rather than radioactivity as the reporter label. The ELISA technique was developed by Peter Perlmann, principal investigator, and Eva Engvall at Stockholm University, Sweden. In 1960, the immunoassay technique with a radioactive label immediately caught the attention of many researchers and clinicians. In 1968, Miles and Hales published their first results of an "immuno-radiometric" technique with radioactive labeled antibodies measuring insulin in human plasma. Despite of special facilities which enabled investigators to work safely with the required amounts of radioactivity, the concerns persisted regarding amongst others the safety, the radioactive waste and the requirements for special laboratory facilities. In the early 1970s, the idea of using enzymes for labeling was considered with skepticism. Nevertheless, Engvall and Perlmann published their first paper on ELISA in 1971 in which they described quantitative measurements of IgG in rabbit serum with alkaline phosphatase serving as reporter label. Finally, commercialization of ELISA test kits started. Microtiter plates with 96 wells were developed in which either an antigen or an antibody is bound to a solid-phase support. Technical improvements led to automated pipetting devices, multichannel pipettes, and microtiter plate readers and washers. In the 1980s, fully automated test instruments were manufactured which have come to stay in medical laboratories. The invention of ELISA resulted in a whole series of test formats, from the "immuno-radiometric" to many variants of "sandwich" test procedures (Fig. 20). In conclusion, the worldwide number of analytical and clinical investigations based on ELISA as nonradioactive variant of immunoassays is enormous (76).

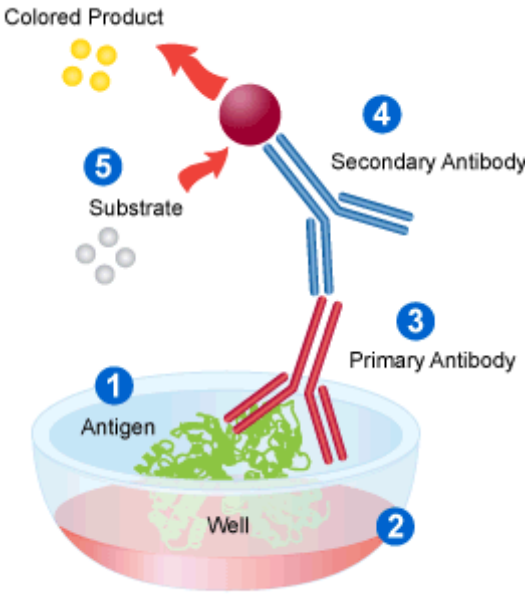

Fig. 20: Schematic setup of a "Sandwich ELISA".
1) A solution of antigen, which is specific for the primary antibody, is immobilized in a well of a microtiter plate. 2) Blocking buffer is added to block remaining binding sites. 3) The sample being assayed (primary antibody) is then applied in order to bind to the immobilized specific antigen. 4) The bound primary antibody is recognized by addition of a specific secondary antibody, which is linked to an enzyme that catalyzes the conversion of its substrate to a detectable form. 5) Finally, the enzyme substrate is added and incubated so that the enzyme can catalyze the conversion of the substrate to signal the detection of the primary antibody (77), modified.

ELISAs typically employ either a chromogenic or a fluorogenic substrate producing a color or fluorescence change. Conversion of the enzyme substrate is observed on a plate reader measuring optical density or fluorescence intensity. In summary, a color or fluorescence change signals the enzyme activity, which indicates the presence of the secondary antibody and therefore the presence of the primary antibody and the antigen as well (78).

3.3.2 SbpA and rSbpA/ZZ recrystallization and preparation for the immobilization of human IgG

The SbpA and rSbpA/ZZ solutions with a concentration of about 1 mg/mL were diluted 1:15 with TRIS-buffer solution. 110 µL SbpA solution were provided to the first part of a 96 well ELISA plate (Microlon 200; GREINER, medium capacity), while 110 µL rSbpA/ZZ solution were added to the second part under the same conditions. The recrystallization was performed at 4°C overnight. Unbound S-layer protein was washed away with TRIS-buffer solution. For the chemical immobilization of human IgG to SbpA, several treatments are required (79). The SbpA coated wells were crosslinked with 100 µL glutardialdehyde (0.5% glutardialdehyde in 0.1 M phosphate buffer solution, pH 7.2) for 30 minutes; crosslinking was stopped with 1 M

TRIS solution for 5 minutes. After glutardialdehyde crosslinking, Schiff bases were reduced with 100 µL sodium borohydride solution (10 mM $NaBH_4$ in 10 mM NaOH) for 1 hour. Further, the SbpA protein was activated by providing 100 µL EDC solution (1 mg/mL 1-ethyl-3-(3-dimethylaminopropyl)carbodiimide in Milli-Q water, pH 4.75) for 1 hour at room temperature, followed by washing with Milli-Q water.

3.3.3 Detection of human IgG immobilization on SbpA and rSbpA/ZZ

For the immobilization of human IgG, a stock solution with a concentration of 1 mg/mL human IgG (Human IgG-reagent grade, Sigma, I4506) in blocking solution composed of 0.2% Blocking Reagent CA (AppliChem, A3409) in PBS (phosphate buffered saline) was prepared. First, 100 µL blocking solution were provided to all wells. Then, 100 µL human IgG with a concentration of 2 µg/mL in blocking solution were offered to the first well-row resulting in 200 µL with a human IgG concentration of 1 µg/mL. After pipette-mixing, 100 µL of this solution were offered to the second row and so further. Therefore, a serial dilution of human IgG ranging from 1000-8 ng/mL in blocking solution was provided to the S-layer coated wells (except one column for each S-layer type serving as blank). The immobilization reaction was performed for 2 hours at room temperature under shaking conditions of 300 rpm followed by washing with PBS. To prevent unspecific binding of the secondary antibody (80), the SbpA and rSbpA/ZZ coated wells were blocked by incubating them with 300 µL blocking solution for 4 hours at room temperature. After washing with PBS, 100 µL anti human IgG POD solution (anti human IgG (Fab specific) peroxidase conjugate, Sigma, A0293, diluted 1:5000 in PBS) were added to all wells and incubated for 30 minutes at room temperature and 300 rpm followed by washing with PBS. In the meantime, a TMB solution was prepared for the detection reaction: 1 TMB tablet (3,3',5,5'-Tetramethylbenzifidine dihydrochloride, Sigma, T3405; 1 mg per tablet) was solved in 12 mL TMB buffer solution (50 mM sodium acetate buffer, adjusted with acetic acid to pH 5.5) and 2 µL 30% H_2O_2 were added. 100 µL TMB solution were applied to all wells. In the moment, when a color development could be observed (H_2O_2 and POD catalyze the oxidation of reduced $TMBH_2$ to TMB forming a blue color, Fig. 21), the reaction was stopped by adding 25 µL 2 M H_2SO_4 to all wells (transformation into a super-oxidized yellow product, detectable at 450 nm). To detect the amount of bound anti human IgG and therefore indirectly detect the immobilization of human IgG on S-layer protein, the absorption was measured colorimetrically at 450 nm in a multiplate reader (infinite F200, Tecan).

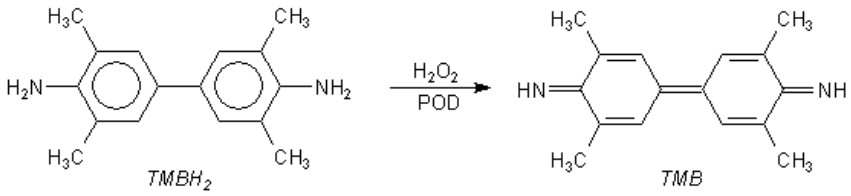

Fig. 21: Conversion of $TMBH_2$ to TMB by enzymatic reaction with H_2O_2 and peroxidase (POD).

3.3.4 Optimization of human IgG detection on rSbpA/ZZ

To achieve improvements and present an alternative to the enzyme POD coupled to the secondary antibody, further immobilization experiments on rSbpA/ZZ were assayed with alkaline phosphatase (ALP) as substrate-converting enzyme. In addition, a crosslinking step with DMP (Dimethyl pimelimidate dihydrochloride, Thermo Scientific, 21667) was performed after antibody immobilization in order to introduce covalent bonds between the S-layer protein and the antibody (81) (33) and to investigate its impact on the antibody activity. Recrystallization procedure of the rSbpA/ZZ protein was performed as described above. For the immobilization of human IgG, a serial dilution of human IgG ranging from 500-0.5 ng/mL in blocking solution was applied to the rSbpA/ZZ coated wells and the immobilization was carried out as described above. After washing with PBS, 120 µL of 10 mM DMP in HEPES buffer solution (100 mM 4-(2-hydroxyethyl)-1-piperazineethanesulfonic acid, 10 mM $CaCl_2$, pH 8) were optionally supplied for 45 minutes at room temperature and 300 rpm, followed by washing with PBS. The blocking procedure was performed as described above. Afterwards, 100 µL anti human IgG ALP solution (anti human IgG (Fab specific) alkaline phosphatase, Sigma, A8542, diluted 1:40000 in PBS) were added to each well and incubated for 30 minutes at room temperature and 300 rpm, followed by washing with PBS. In the meantime, a pNPP solution was prepared: 2 tablets of pNPP (4-Nitrophenylphosphate disodium salt hexahydrate, Sigma, N9389; 5 mg/tablet) were solved in 10 mL DEA buffer solution (1 M Diethanolamine, 0.5 mM $CaCl_2$). Then, 100 µL of pNPP solution were supplied; for the enzyme reaction (ALP converts pNPP into p-Nitrophenol forming a yellow color, Fig. 22) the plate was stored for 15 minutes in the dark. Finally, the reaction was stopped by adding 25 µL of 3 M NaOH and the absorption was measured colorimetrically at 405 nm in Tecan multiplate reader.

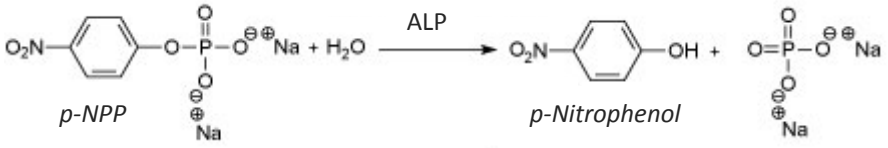

Fig. 22: Conversion of p-NPP to p-nitrophenol by enzymatic reaction with alkaline phosphatase (ALP).

3.4 Surface Plasmon Resonance

Surface plasmon resonance (SPR) was applied in order to quantify the amount of antibody bound to rSbpA/ZZ. Besides, the antifouling properties of rSbpA/ZZ in comparison to gold were investigated by supplying human plasma samples. In general, the SPR containing a microfluidic system should provide information about the stability of antibody immobilization.

3.4.1 Fundamentals of SPR

The application of Surface Plasmon Resonance (SPR) is increasingly popular for it allows quantitative measurements of biomolecular interactions in real-time without requiring a labeling procedure. Amongst others, fundamental biological studies, health science research and environmental and agricultural monitoring are the fields of interest (82).

In the early 20th century, the excitation of surface plasmons was observed as anomalous reflection when polarized light hit a metal grating, which was initially termed Wood's Anomalies (Wood, 1902). Nowadays, biosensors using the excitation of the surface plasmons are in general termed "Surface Plasmon Resonance" (SPR) providing important information about specificity, affinity, and kinetics of biomolecular interactions. In SPR biosensing, the adsorption of an analyte of interest to a surface bioreceptor is detected by measuring the change of the resonance coupling of incident light to the propagating surface plasmon wave (SPW). The existence of the SPW is determined by the electromagnetic properties of the metal, typically a thin film of gold sputtered on a glass sensor chip, and the dielectric interface (sample medium). A decaying electrical field associated with the SPW travels for a short distance of ~300 nm from the gold film into the sample medium. For this, the resonant frequency of the SPW as well as the angle shift of the incident light depend on the refractive index of the sample medium changing with the modification of the surface. The coupling of incident light to surface plasmons results in a reduction of the intensity of reflected light, which is traditionally tracked by measuring the resonant angle shift (Fig. 23) An SPR biosensor necessarily comprises four components: a microfluidic system for sample handling, an opto-electronic system for SPR-excitation and -detection, a biointerface functionalized with surface receptors and a data analysis module to extract the relevant information (82).

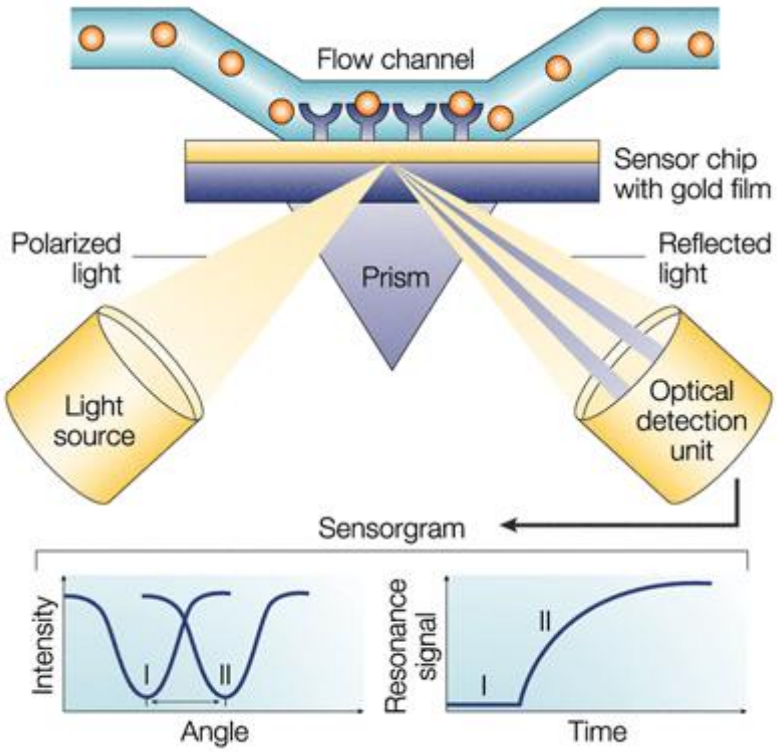

Fig. 23: Typical setup for an SPR biosensor.
SPR detects changes in the refractive index of the sample medium presenting the immediate vicinity of the surface layer of a sensor chip. SPR is observed in the reflected light from the surface at an angle dependent on the mass of material at the surface. The SPR angle shifts (from I to II in the lower left-hand diagram) when biomolecules bind to the chip surface changing the mass of the surface layer. This change in resonant angle can be monitored in real-time and label-free as a plot of resonance signal (proportional to mass change) versus time (83).

3.4.2 Sensor chip preparation

SPR studies were performed with a Biacore 2000 system (Biacore, Uppsala, Sweden). Glass sensor chips sputtered with gold (10x12 mm sq. SPR-Au, Ssens bv) were cleaned in piranha solution (30% H_2O_2: conc. H_2SO_4 = 3:7) for 15 minutes, washed with Milli-Q water and dried with helium before docking to the SPR-system. Before starting the sensorgram, the system was primed three times with running-buffer. There are four flow cells which can be directed separately or in different combinations. The base line was set with running-buffer for at least 10 minutes at a flow rate of 10 µL/min. Aside from the injection-steps, running-buffer was supplied to the system. All buffers and reagents are listed in Table 1.

Table 1: Buffers and reagents used for SPR experiments.

Buffers	Concentration/composition	Origin
Running-buffer	Milli-Q water	DNBT
TRIS-buffer	0.5 mM Tris(hydroxymethyl)-aminomethane 10 mM Calcium chloride dihydrate pH 9	BIO-RAD, 161-0716 Riedel-de Haen, 31307
HEPES-buffer	100 mM HEPES-b 10 mM $CaCl_2x2H_2O$ pH 8	GERBU
Reagents		
SCWP	100 µg/mL thiolated secondary cell wall polymer	DNBT
SbpA	1 mg/mL SbpA protein	DNBT
rSbpA/ZZ	1 mg/mL rSbpA/ZZ protein	DNBT
DMP	Dimethyl pimelimidate dihydrochloride	Thermo Scientific, 21667
Human IgG	Human IgG-reagent grade	Sigma, I4506
CD3-Ab	Purified mouse human anti-CD3, IgG2a, monoclonal	BD Pharmingen, 555337
Full-plasma	Human heparin-plasma	DNBT
IgG-free plasma	Human heparin-plasma purified from IgG via protein G column	DNBT

3.4.3 Recrystallization of the S-layer proteins SbpA and rSbpA/ZZ

To investigate and compare the quantity of SbpA and rSbpA/ZZ recrystallization, the S-layer proteins were recrystallized on the sensor chip and analyzed and compared by doing SPR-experiments listed in Table 2. In order to achieve the best efficiency for antibody binding, the gold chips were precoated with thiolated SCWP to guarantee a directed S-layer recrystallization (27) (33) (Fig. 24).

Table 2: Recrystallization of rSbpA/ZZ and SbpA on gold prior modified with thiolated SCWP.

step	flow cell	reagent	concentration	flow rate / µL/min	time / min
1.	1-2	thiolated SCWP	100 µg/mL	5	12
2.	1	rSbpA/ZZ	100 µg/mL in TRIS-buffer	1	60
3.	2	SbpA	100 µg/mL in TRIS-buffer	1	60

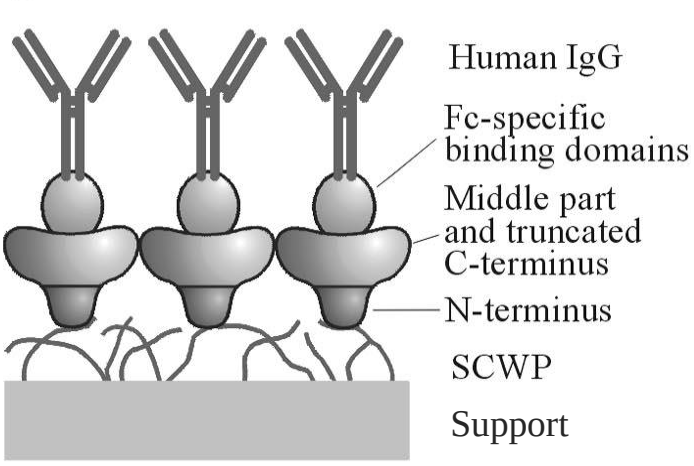

Fig. 24: Schematic illustration of the immobilization of human IgG on rSbpA/ZZ recrystallized on the gold support via thiolated SCWP (33), slightly modified.

3.4.4 Investigation of antibody binding and antifouling properties

For a basic setup, the gold chip coating with thiolated SCWP and rSbpA/ZZ was performed several times in order to continue either with the binding of antibodies or with the investigation of antifouling properties in comparison to gold. For this, the flow cells 1-2 were coated with thiolated SCWP and rSbpA/ZZ while the flow cells 3-4 remained as unmodified gold (Table 3).

Table 3: Basic setup with coating of thiolated SCWP and rSbpA/ZZ.

step	flow cell	reagent	concentration	flow rate / µL/min	time / min
1.	1-2	thiolated SCWP	100 µg/mL	5	12
2.	1-2	rSbpA/ZZ	100 µg/mL in TRIS-buffer	1	60

3.4.4.1 Antifouling properties of rSbpA/ZZ

The antifouling properties of rSbpA/ZZ were analyzed with full-plasma and IgG-free plasma (flow cells 1-2) which was prepared via a protein G affinity column chromatography and kindly obtained from Andrea Scheberl at DNBT. The affinity of the plasma samples to the S-layer fusion protein was compared to gold (flow cells 3-4). The described experiments (Table 4) where appended to the basic setup shown in Table 3 (for a better overview, the prior modification steps are always listed in the flow cell column).

Table 4: Investigation of antifouling properties of rSbpA/ZZ against IgG-free plasma and full-plasma in comparison to gold.

step	flow cell	reagent	dilution	flow rate / µL/min	time / min
3.	1 (rSbpA/ZZ)	IgG-free plasma	1:100 in running-buffer	3	20
4.	2 (rSbpA/ZZ)	full-plasma	1:500 in running-buffer	3	20
3.	3 (gold)	IgG-free plasma	1:100 in running-buffer	3	20
4.	4 (gold)	full-plasma	1:500 in running-buffer	3	20

3.4.4.2 Binding of human IgG and CD3-Ab to rSbpA/ZZ

The known affinity between IgG and the Z-sequence presented a challenge to investigate the binding of human IgG and CD3-Ab to rSbpA/ZZ and to compare these different antibodies. Aside from SPR, the CD3-Ab should find its application later in CD3-cell capture experiments. Due to the fact that monoclonal antibodies are expensive, the concentration of CD3-Ab (50 µg/mL) was chosen lower than the one of human IgG (100 µg/mL) but still at an excessive level. The antibody immobilization experiments (Table 5) were appended to the basic setup described in Table 3 and performed several times to enable various further experiments. To crosslink the antibody with the S-layer fusion protein, DMP was added after antibody immobilization.

Table 5: Immobilization of human IgG and CD3-Ab to rSbpA/ZZ.

step	flow cell	reagent	concentration	flow rate / µL/min	time / min
3.	1 (rSbpA/ZZ)	human IgG	100 µg/mL in TRIS-buffer	3	40
4.	2 (rSbpA/ZZ)	CD3-Ab	50 µg/mL in TRIS-buffer	3	40
5.	1-2 (rSbpA/ZZ, human IgG / CD3-Ab)	DMP	10 mM in HEPES-buffer	2	40

3.4.4.2.1 Antifouling properties of rSbpA/ZZ with immobilized CD3-Ab

After the antifouling analysis of rSbpA/ZZ alone, the focus lied on the investigation of the antifouling properties of rSbpA/ZZ after the immobilization of the antibody CD3-Ab compared to gold. Therefore, the following described experiments with IgG-free plasma and full-plasma (Table 6 and Table 7) were appended to the antibody immobilization experiments listed in Table 5.

Table 6: Antifouling experiments with IgG-free plasma on CD3-Ab prior immobilized on rSbpA/ZZ and crosslinked with DMP.

step	flow cell	reagent	dilution	flow rate / µL/min	time / min
6.	2 (rSbpA/ZZ, CD3-Ab, DMP)	IgG-free plasma	1:100 in running-buffer	3	10
6.	3 (gold)	IgG-free plasma	1:100 in running-buffer	3	10

Table 7: Antifouling experiments with full plasma on human IgG and CD3-Ab prior immobilized on rSbpA/ZZ and crosslinked with DMP.

step	flow cell	reagent	dilution	flow rate / µL/min	time / min
6.	2 (rSbpA/ZZ, CD3-Ab, DMP)	full-plasma	1:500 in running-buffer	3	10
6.	3 (gold)	full-plasma	1:500 in running-buffer	3	10

3.5 Static cell capture

Due to the IgG affinity matrix that rSbpA/ZZ is offering, the CD3-Ab was immobilized on rSbpA/ZZ to capture Jurkat cells expressing the CD3 receptor. The performance of several experiments should prove the specific capture of CD3-cells to the CD3-Ab. First, the focus lied on the quantification of the amount of captured Jurkat cells, followed by experiments with a mixture of two differently labeled cell types to investigate the specificity of the binding between CD3-cells and the CD3-Ab.

3.5.1 The T-cell receptor-CD3 complex

The T-cell receptor (TCR)-CD3 complex (CD stands for cluster of differentiation) is one of the most complicated identified transmembrane (TM) receptor structures and fulfills an important function in the immune system. Signals that are delivered through this complex are required for T-cell development in the thymus. Further, these signals are responsible for induction of T-cell mediated immune responses against infectious agents and for T-cell differentiation into effector and memory populations that owe distinct properties. The αβ TCR-CD3 contains six different TM proteins which are the TCRα and TCRβ chains and the non-covalently linked CD3γ, CD3δ, CD3ε and ζ chains. TCRα and TCRβ chains form the TCR heterodimer responsible for ligand recognition, while CD3γ, CD3δ, CD3ε and ζ chains include cytoplasmic sequence motifs and recruit many signaling components (84) (Fig. 25).

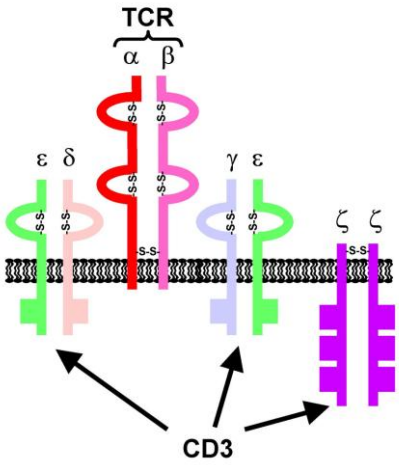

Fig. 25: Schematic of the TCR-CD3 complex across the cytoplasmic membrane.
The TCR is formed by two subunits (αβ) and the other four proteins assemble in three dimers (γε, δε and ζζ) to form the CD3 complex (85).

3.5.2 The Jurkat cell line – CD3-cells

Jurkat cells are an immortalized line of T-lymphocyte cells (Fig. 26) which was established from the peripheral blood of a 14 year old boy by Schneider et al. 1977 (86) . According to ATCC where the Jurkat cell line (TIB-152) was ordered at, the cells express the CD3 antigen. Jurkat cells were grown and passed in RPMI 1640 medium (Thermo Scientific: SH30096.FS) supplemented with 10% fetal bovine serum (DNBT), 1% glutamine, 1% antibiotics, 1% HEPES and 1% non-essential amino acids (Thermo Scientific: SH30034.01, SV30079.01, SH30851.01, SH30238.01, respectively) and cultured at 37°C. Cells were routinely passed every 3 days when their concentration was between 0.2-1.0x10^6/mL. The size of the Jurkat cells can diverge, most cells varying between 7 and 20 µm in diameter (87); measuring the herein used Jurkat cells under the microscope (Eclipse TE2000-S) revealed an average diameter of 20 µm.

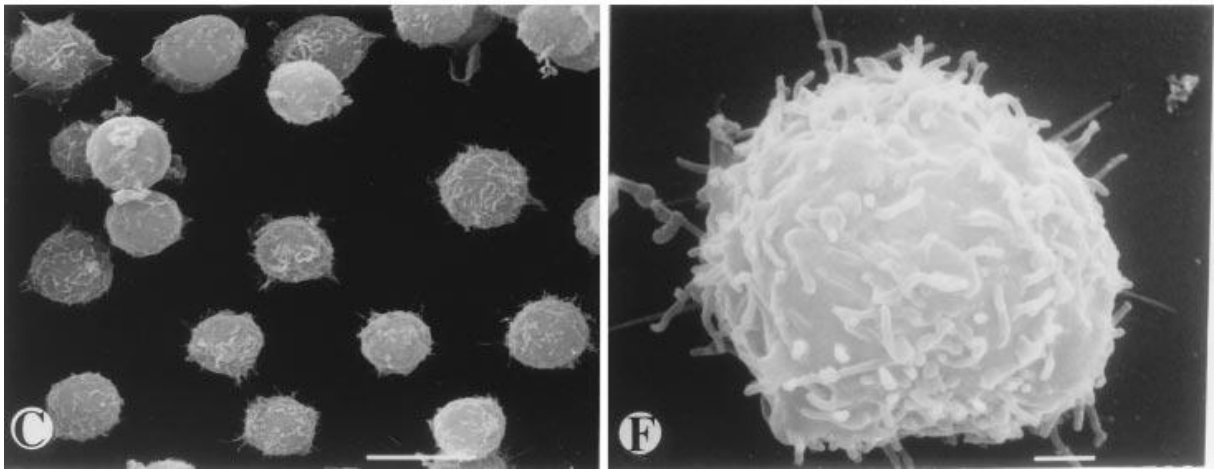

Fig. 26: SEM image of Jurkat cells with scale bars of 10 µm (C) and 1 µm (F) (88).

3.5.3 Jurkat cell capture via CD3-Ab immobilized on rSbpA/ZZ protein

Glass cover slides (diameter 12 mm, Menzel, Germany) were modified by coating with rSbpA/ZZ 1:15 diluted in TRIS-buffer solution at 4°C overnight. After washing with TRIS-buffer solution, 2 µg/mL CD3-Ab in PBS were immobilized on the recrystallized rSbpA/ZZ layer during 2 hours at room temperature. After washing with PBS, an excess of Jurkat cells in growth medium, about 1x10^6 cells/mL, was offered to the modified cover slides at room temperature. After 15 minutes unbound cells were removed carefully from the surface by putting the sample into PBS. Jurkat cells were provided to an rSbpA/ZZ coated cover slide without antibody as well which served as reference sample. All samples were observed under a microscope (Eclipse TE2000-S inverted fluorescence microscope, Nikon Instruments,

Japan; Nikon digital DS-Qi1Mc camera; NIS-elements imaging software) to determine the amount of captured cells per cm^2.

3.5.4 Specific Jurkat cell capture from a cell mixture

To investigate the specific capture of Jurkat cells (expressing the CD3-receptor) by the CD3-Ab, a mixture of differently labeled Jurkat and MOLT 3 cells (expressing the CD4-receptor, ordered from ATCC, CRL-1552, grown under the same conditions as Jurkat cells) was provided to cover slides prior functionalized with rSbpA/ZZ and CD3-Ab.

3.5.4.1 Cell labeling of Jurkat and MOLT 3 cells

For the labeling of Jurkat and MOLT 3 cells, the cells were centrifuged at 1200 rpm for 5 minutes and resuspended in RPMI 1640 medium with a temperature of 37°C to a cell concentration of $1x10^6$/mL. 5 µL of the cell-labeling solution (Jurkat cells: Orange-fluorescent Cytoplasmic Membrane Staining Kit, PromoKine, PK-CA707-30022; MOLT 3 cells: Green-fluorescent Cytoplasmic Membrane Staining Kit, PromoKine, PK-CA707-30021) were supplied per 1 mL of cell suspension and incubated for 20 minutes at 37°C in the dark. For the washing procedure, the labeled cells were centrifuged at 1200 rpm for 5 minutes. The supernatant was removed and the cells were resuspended in growth medium with a temperature of 37°C. The washing procedure was repeated two more times.

3.5.4.2 Specific Jurkat cell capture from a cell mixture of Jurkat and MOLT 3 cells via CD3-Ab immobilized on rSbpA/ZZ

A total amount of $2.0x10^5$ cells with different compositions of Jurkat and MOLT 3 cells was provided to glass cover slides prior modified with rSbpA/ZZ and CD3-Ab as described above. The Jurkat and CD4-cell suspensions were counted with Countess™ Automated Cell Counter (Invitrogen, Austria), accordingly diluted in growth medium and mixed together to the following contents of Jurkat cells: 100%, 50% and 20% (difference to 100%: MOLT 3 cells). The cell capture experiments were carried out as described above but in the dark due to the presence of fluorescent dyes.

3.5.4.2.1 Microscopical setup

Fluorescence microscope imaging was performed using an Eclipse TE2000-S inverted fluorescence microscope (Nikon Instruments, Japan) with a mercury-vapor lamp, a Nikon digital DS-Qi1Mc camera and the NIS-elements imaging software using the proper filter blocks depending on the fluorophore used (Table 8).

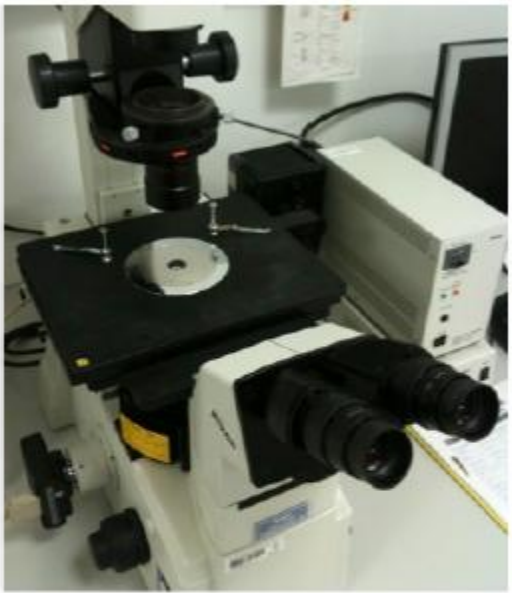

Fig. 27: Eclipse TE2000-S inverted fluorescence microscope (Nikon Instruments, Japan).

Table 8: Absorption/emission spectra for the fluorophors and filter blocks.

Fluorophore	Absorption / nm	Emission / nm	Filter block
Green-fluorescent	484	501	FITC (green, yellow)
Orange-fluorescent	549	565	TRITC (red)

3.6 Microfluidic cell capture

To extend the static cell capture from the cover slides to a microfluidic cell capture chip, PDMS and SU8 based microchips were designed, fabricated and modified with the S-layer fusion protein rSbpA/ZZ and CD3-Ab to perform microfluidic Jurkat cell capture (Fig. 28).

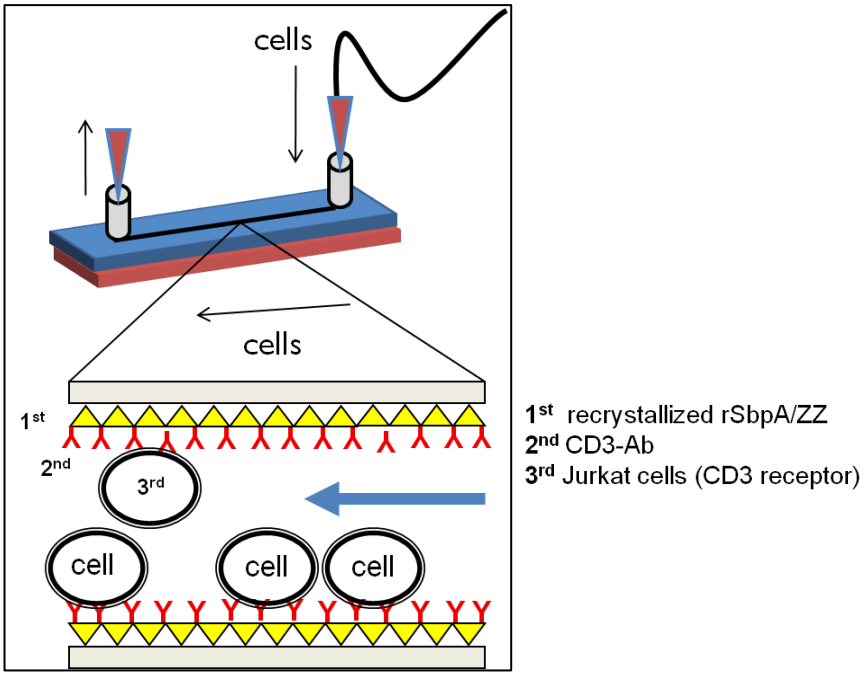

Fig. 28: Schematic of microfluidic Jurkat cell capture via CD3-Ab immobilized on rSbpA/ZZ.

3.6.1 Mask designs for PDMS and SU8 fabricated microchips

All mask designs for PDMS and SU8 fabricated microchips were realized from PIU-Printex GmbH as positive and negative photo plots.

3.6.1.1 Mask design for PDMS fabricated microfluidic chips

Masks for PDMS fabricated microfluidic chips were designed in 2009 by Verena Charwat, AIT, with TARGET 3001! software, a program for computer-aided design (CAD). The chip design consists of four channels with equal width of 500 µm and individual in- and outlets and is termed “spider” (Fig. 29).

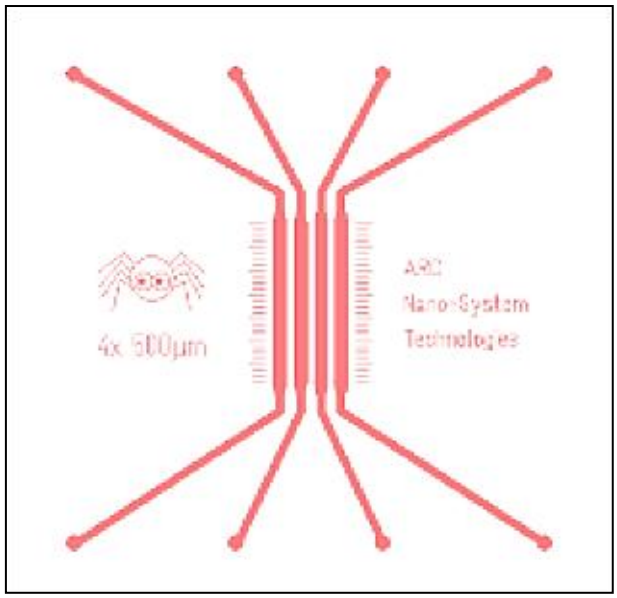

Fig. 29: Master mold design for PDMS fabricated microchips.
Spider with four parallel channels with equal width of 500 µm and individual in- and outlets (by courtesy of Verena Charwat, AIT).

3.6.1.2 Mask design for SU8 fabricated microfluidic chips

For SU8 fabricated microfluidic chips the master molds were designed with CleWin4 software. The idea was to capture a large amount of cells within the channels, therefore a design of two parallel channels with a channel width of 3 mm, a channel-wall width of 100 µm and individual in- and outlets was chosen (Fig. 30). Hence SU8 fabricated microchips were only constructed of the channels walls and require one step less in production than PDMS fabricated chips, the design principle for the SU8-design demonstrates the negative of the PDMS-design above.

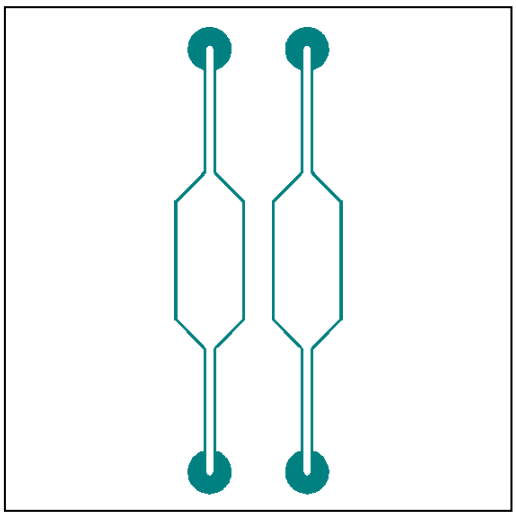

Fig. 30: Master mold design for SU fabricated microchips.
Two parallel channels with identical parameters and individual in- and outlets: channel width = 3 mm, channel-wall width = 100 µm.

3.6.2 Master mold fabrication for PDMS microchips

All master molds were provided by Department of Health & Environment, Nano Systems, AIT Austrian Institute of Technology. Spin coating and UV photolithography was used for the fabrication of SU8 based master molds as described in Fig. 31:

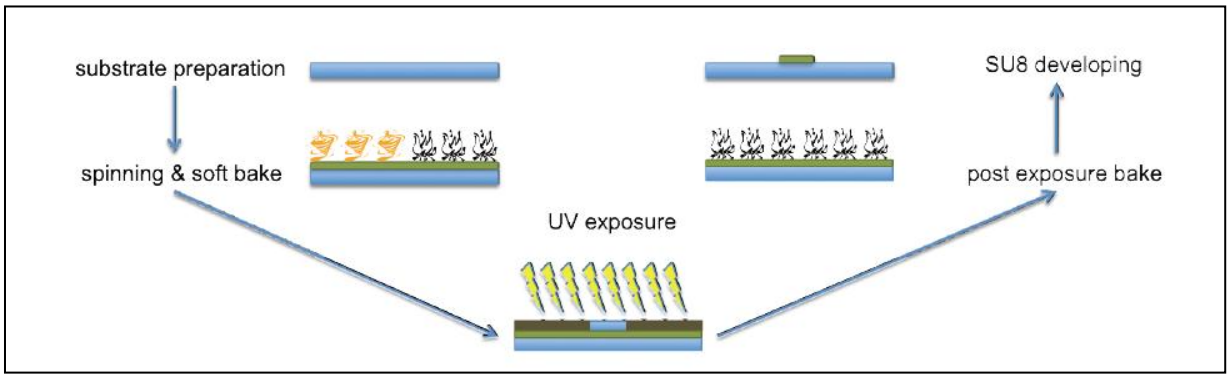

Fig. 31: Schematic of the process for the fabrication of an SU8 master mold.
Substrate preparation, spinning and soft bake, UV exposure, post exposure bake and SU8 developing (by courtesy of Mario Rothbauer, DNBT).

A silicon substrate was cleaned by performing the following steps in an ultrasonic bath: cleaning with detergent solution, Milli-Q water, acetone and finally isopropanol for 4 minutes per cleaning step. Afterwards the wafer was dried by blowing with nitrogen and additionally on a hot plate at 200°C for 5 minutes to increase the adhesion of the lithographic resin to the substrate. The SU8-2050 negative epoxy photoresist (Microchem, USA) was spun onto the substrate (3500 rpm, 50 seconds) followed by a soft bake step at 65°C for 5 minutes and 95°C for 15 minutes to form a 30 µm high resin. After UV exposure at 750 mJ/cm^2 for 4 minutes, a post exposure bake (PEB) at 95°C for 10 minutes was conducted to crosslink the exposed areas. The created patterns were developed in SU8 developer (Microchem, USA) for 2.5 minutes to remove the unexposed areas leaving only the structure of the future microfluidic device.

3.6.3 Microfluidic PDMS chip assembly

The microfluidic chip (height: 30 µm, width: 500 µm) was fabricated by replica molding PDMS (Dow Corning, USA) versus the master mold. PDMS base (silicon elastomer Sylgard 184) and curing agent were mixed in 10:1 mass ratio and the mixture was poured onto the cleaned master mold to form a 1-2 mm thick PDMS layer. Bubbles and foam were removed by degassing in an evacuated exsiccator for 45 min at room temperature. After degassing, the PDMS was cured for 2 hours at 80°C. Then, a rectangular polymer sheet was cut out of the PDMS block and peeled off from the master. For in- and outlets of the microfluidic chip, ports were punched into the PDMS with a blunt tube (diameter 1 mm). For the fabrication of

the microfluidic device, conventional ~25 x 25 mm glass bottom and top pieces were manually cut out of 1.0 mm thick, 26 x 76 mm microscope slides (Menzel, Germany). The top and bottom glass substrates as well as the PDMS mold were cleaned with detergent, rinsed with 70% isopropanol and Milli-Q water and dried for one hour at 80°C. First, the top substrate was covalently bonded to the PDMS fluidic by plasma treatment using an easiGlow system (Pelco, USA). In this context, bonding means the establishment of covalent bonds between plasma activated PDMS and glass surfaces due to the formation of silanol groups forming covalent bonds when sticked together (Fig. 32). Hence, the bottom substrate was attached to the microfluidic device in the same manner. The chip ports were stacked together, inserted into predrilled holes on the glass top and fixed using a Loctite 9492 A&B two-component adhesive (Henkel, Germany) which was cured at 80°C for 10 minutes.

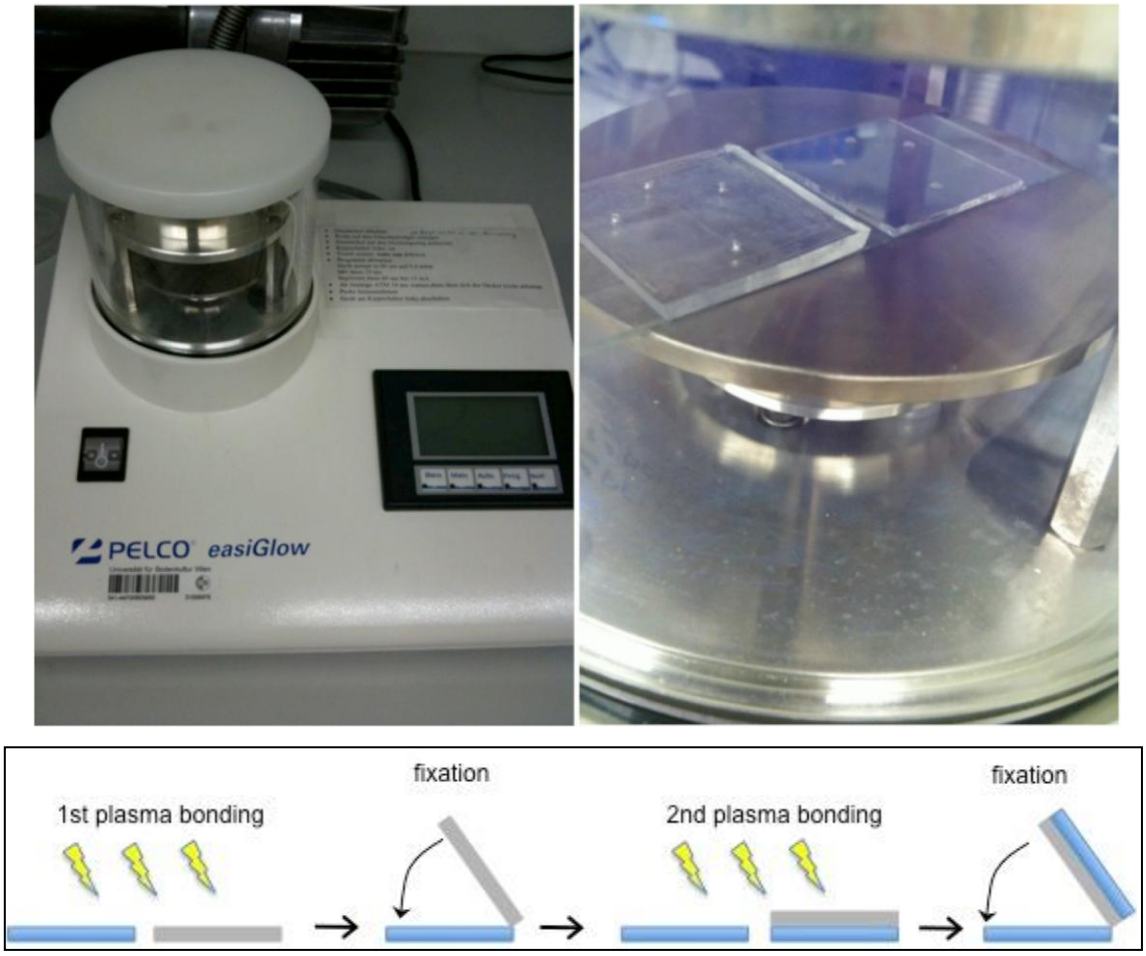

Fig. 32: Plasma bonding procedure for PDMS microchips.
Photographs of the easiGlow device (left) and a PDMS mold and glass substrate during bonding (right). Schematic illustration of the whole plasma bonding procedure (below, by courtesy of M. Rothbauer).

3.6.4 Cell capture experiments in PDMS microchips

3.6.4.1 System components for PDMS microchips

An infusion-only syringe pump (model: KDS-250-CE; kdScientific, USA) and a gastight 2.5 mL glass syringe (Hamilton, Germany) were used for all washing procedures. Another disposable 1 mL syringe (BD Biosciences, Germany) connected to the Luer-Lok™ seeding port was used for withdrawing cells into the chip in reverse direction. A four-way L-valve was used to control the fluid flow directions into the LOC and the waste-tube as well as for the seeding procedure. All of the system components (Table 9) were connected using FEP Nat tubes apart from the in- and outlet tubes of the microfluidic device, which were connected using PEEK tubing.

Table 9: Components of the microfluidic tubing system for PDMS microchips.

Name	Usage	Description	Product number
4-Way "L" valve	direction of the fluid flow	Right angle flow-switching valve ("L"), PEEK, 6.2 µL swept volume	Upchurch Scientific: V-100L
Flangeless Fittings	tube-valve and tube-syringe interfaces	Fitting + ferrule	Upchurch Scientific
Flangeless Male Nut	tube-valve and tube-syringe interfaces	1/16, PP	Upchurch Scientific: P-220X
Sleve FEP Green	connections of tubes	Sleeves for capillary tubing connections	Upchurch Scientific: F-247X
Flangeless Ferrule	tube-valve and tube-syringe interfaces	1/16, blue	Upchurch Scientific: P-200X
PEEK tube	valve-to-microfluidic tube	1/32" x 0.13 mm ID	VICI, JR-T-5993-M10
FEP Nat tube	syringe-to-valve tube, valve-to-waste-tube	1/16" x 0.254 mm ID	Upchurch Scientific: 1526
Female to female Luer	syringe-tube interfaces	1/4-28 female to female Luer (quick connect Luer adapter)	Upchurch Scientific: P-658

3.6.4.2 Static modification of PDMS microchips with rSbpA/ZZ and CD3-Ab

To prepare the microchip for the cell capture experiments, all four channels were washed one after the other by injecting three times 10 µL PBS into the injection port via a micropipette while another pipette tip was added to the outlet port and renewed with every washing step.

After washing, the S-layer fusion protein rSbpA/ZZ was injected the same way at a concentration of 100 µg/mL in TRIS-buffer solution into three channels. To perform the rSbpA/ZZ recrystallization, the microchip was kept overnight at 4°C. The S-layer coated channels were washed three times with TRIS-buffer in order to remove the excess of S-layer protein. 2 µg/mL CD3-Ab in PBS were injected into two of the S-layer coated channels. The CD3-Ab immobilization was performed for 2 hours at room temperature. To finish the chip modification, the four microchannels (one unmodified channel, one channel coated with S-layer and two channels modified with S-layer and CD3-Ab) were washed again three times with PBS.

3.6.4.3 Microfluidic Jurkat cell capture in modified PDMS microchips

The microchip was placed on the microscope (Eclipse TE2000-S, Nikon) and the chip inlet port of one fully modified channel (containing S-layer lattice and CD3-Ab) was connected to the four-way L-valve. Besides, the L-valve was connected to the 2.5 mL syringe pump filled with PBS, to an Eppendorf tube serving as a waste-tube and to another 1 mL syringe which is further called seeding syringe. Finally, the waste-tube was connected to the chip outlet port (Fig. 33).

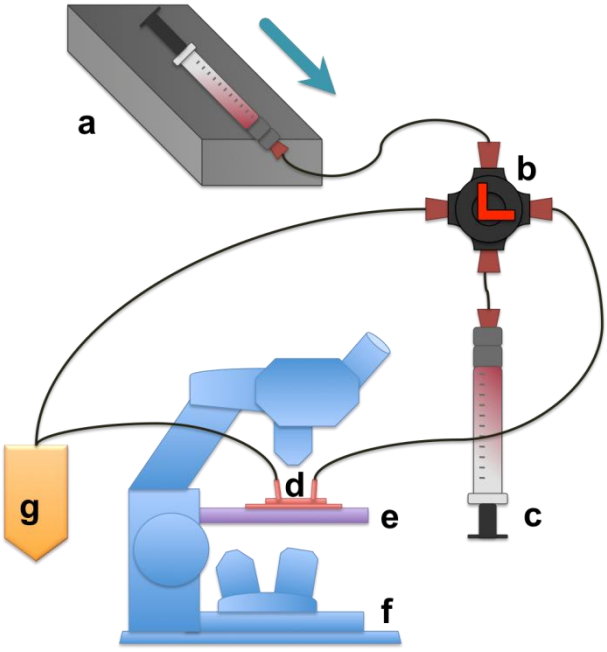

Fig. 33: System setup for microfluidic Jurkat cell capture.
a) infusion-only syringe pump with syringe, b) 4-way L-valve, c) seeding syringe, d) microchip, f) microscope, g) waste-tube.

The microfluidic cell capture procedure is described in Fig. 34: the microchannel was washed via the syringe pump with PBS for 10 minutes at a flow rate of 10 µL/min. After washing, the flow was stopped and the waste-tube was carefully removed from the chip outlet port. A pipette tip was inserted into the outlet port. To fill the pipette tip with PBS, the flow was switched on again. When the tip was halfway filled, the flow was stopped and the valve was switched so that the seeding syringe was connected with the chip inlet. An excess of Jurkat cells was added to the tip at the outlet port filled with PBS. After waiting for 5-10 minutes to guarantee the dropping of the mobile Jurkat cells, the cells were seeded into the channel by manual withdrawing via the seeding syringe. After cell seeding, the pipette tip was replaced by the tube connecting the chip with the waste-tube. After waiting for another 15 minutes to perform the cell capture, the L-valve was switched to connect the syringe pump with the microchip and the flow was restarted. The channel was rinsed with PBS at flow rates from 0.01-1 µL/min in order to remove unbound cells and finally, to rinse all cells out of the microchannel. The described experiment was identically applied to all four channels of the spider chip.

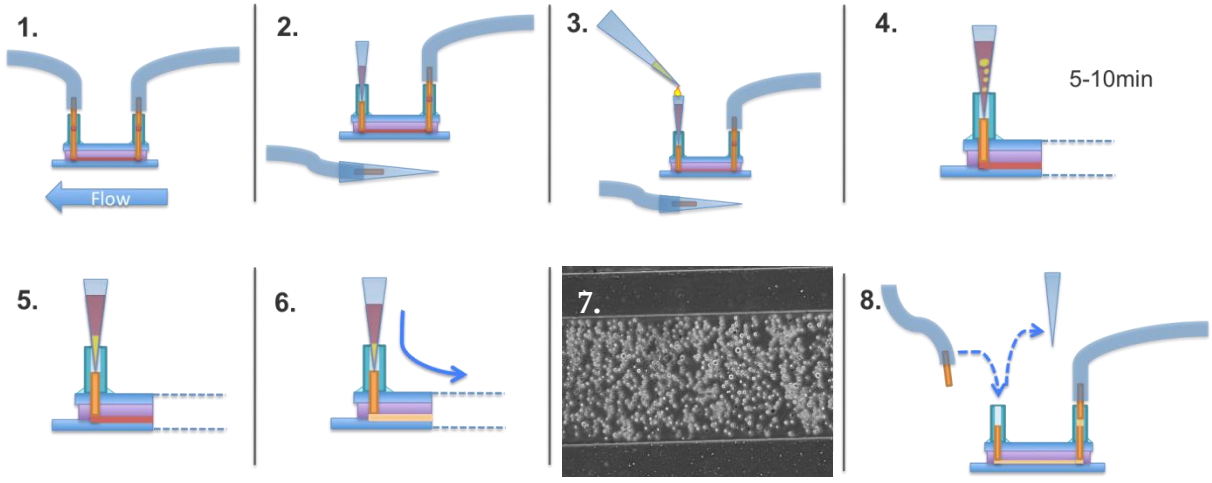

Fig. 34: Microfluidic cell capture procedure.
1.) Chip with tubing at in- and outlet 2.) The waste-tube is replaced with a pipette tip which is filled with PBS. 3.) Cell suspension is pipetted into the PBS-filled tip. 4. & 5.) Cell dropping in the tip. 6. & 7.) The cells are withdrawn into the channel. 8.) The pipette tip is replaced by the waste-tube, after 15 minutes the medium flow is restarted (by courtesy of V. Charwat, slightly modified).

3.6.5 Cell capture experiments in SU8 microchips

In order to present an alternative to the elastomer PDMS, which implies several disadvantages as mentioned in the introduction, cell capture experiments with SU8 fabricated microchips were performed. Besides, the pumping and the valve system of the prior described experiments were improved.

3.6.5.1 System components

An injecting-withdrawing syringe pump (model: KDS-260-CE; kdScientific, USA) and two gastight 2.5 mL glass syringes (Hamilton, Germany) were used for all washing procedures. The syringe pump is able to inject via one syringe while withdrawing via the other syringe at the same time (Fig. 35).

Fig. 35: Injecting/withdrawing syringe pump (KDS-260-CE, kdScientific, USA).

Another disposable 1 mL syringe (BD Biosciences, Germany) connected to the Luer-Lok™ seeding port was used for injecting cells into the chip. Two four-way diagonal flow switching-valves were used to control the fluid flow directions into the LOC and waste-tubes as well as for the seeding procedure. All of the system components (Table 10) were connected using FEP Nat tubes apart from the in- and outlet tube of the microfluidic device, which were connected using PEEK tubing.

Table 10: Components of the microfluidic tubing system for SU8 microchips.

Name	Usage	Description	Product number
4-Way valve PEEK Diagonal flow	Directing fluid flow of two syringes	Diagonal flow switching, PEEK, 12.4 µL swept volume	Upchurch Scientific: V-100D
Flangeless Fittings	tube-valve and tube-syringe interfaces	Fitting + ferrule	Upchurch Scientific
Flangeless Male Nut	tube-valve and tube-syringe interfaces	1/16, PP	Upchurch Scientific: P-220X
Sleve FEP Green	connections of tubes	Sleeves for capillary tubing connections	Upchurch Scientific: F-247X

Flangeless Ferrule	tube-valve and tube-syringe interfaces	1/16, blue	Upchurch Scientific: P-200X
FEP Nat tube	syringe-to-valve tube, valve-to-waste-tube	1/16”x0.254 mm ID	Upchurch Scientific: 1526
PEEK Tubing	valves-to-chip-tubes,	1/16” x 1 mm ID	Upchurch: Scientific: 48511
Female to female Luer	syringe-tube interfaces	1/4-28 female to female Luer (quick connect Luer adapter)	Upchurch Scientific: P-658

3.6.5.2 Static modification of SU8 microchips with rSbpA/ZZ and CD3-Ab

To prepare the two-channel-microchip for the cell capture experiments, the microchip was integrated on a mounting station provided by Department of Health & Environment, Nano Systems, AIT for microchip fixation and tube connection as shown in (Fig. 36). Besides, this setup was placed on the microscope (Eclipse TE2000-S, Nikon) to observe all procedures.

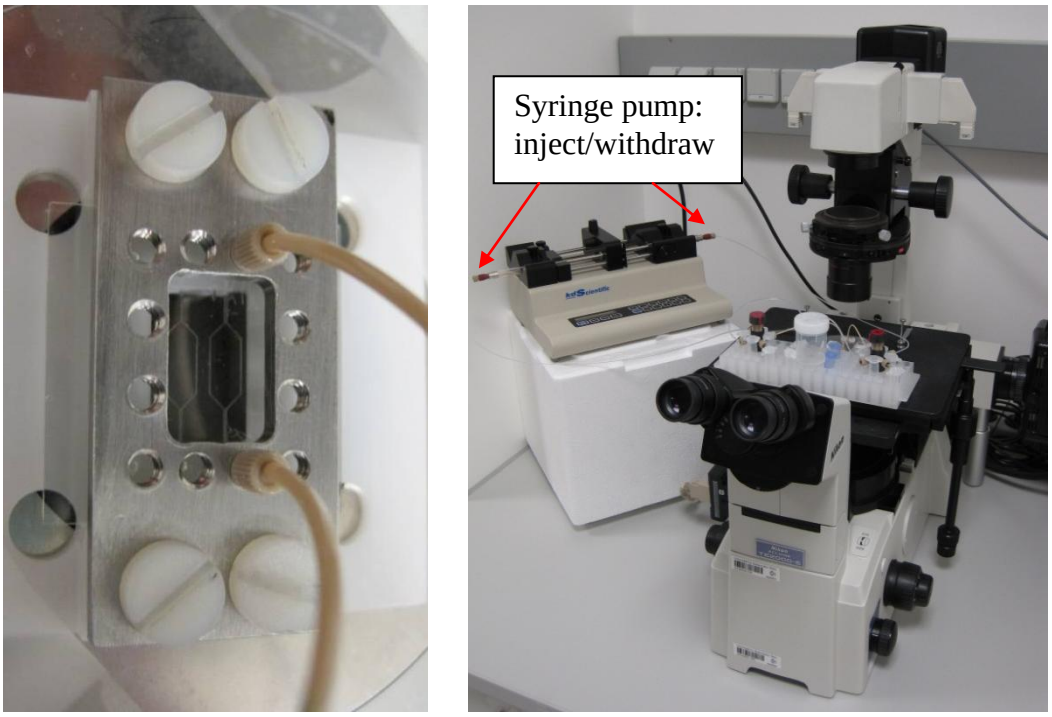

Fig. 36: Mounting station with SU8 microchip (left) and microscopical setup (right).

One microchannel was connected to the tubes (injection tube: length: 14 cm; diameter: 1 mm; V=110 µL) plugged to the in- and outlet valves which were stabilized with several Eppendorf tubes. The inlet valve was further connected via a tube to the injecting syringe, the sample-tube and the waste-tube, while the outlet valve was connected to the withdrawing syringe, the reservoir-tube and the waste-tube (Fig. 37). The microchannel was rinsed with isopropanol via the injecting-withdrawing syringe pump to get rid of air bubbles followed by washing

with PBS; each washing step was performed for 10 minutes at a flow rate of 50 µL/min. While washing with PBS, the sample-tube connected to the inlet valve was filled with 1 mL of 100 µg/mL rSbpA/ZZ protein in TRIS-buffer solution. After washing, the inlet valve was switched leading the injection to the waste-tube. Hence, only the withdrawing syringe was connected to the chip in order to withdraw the rSbpA/ZZ solution into the channel (withdrawing mode: Fig. 37).

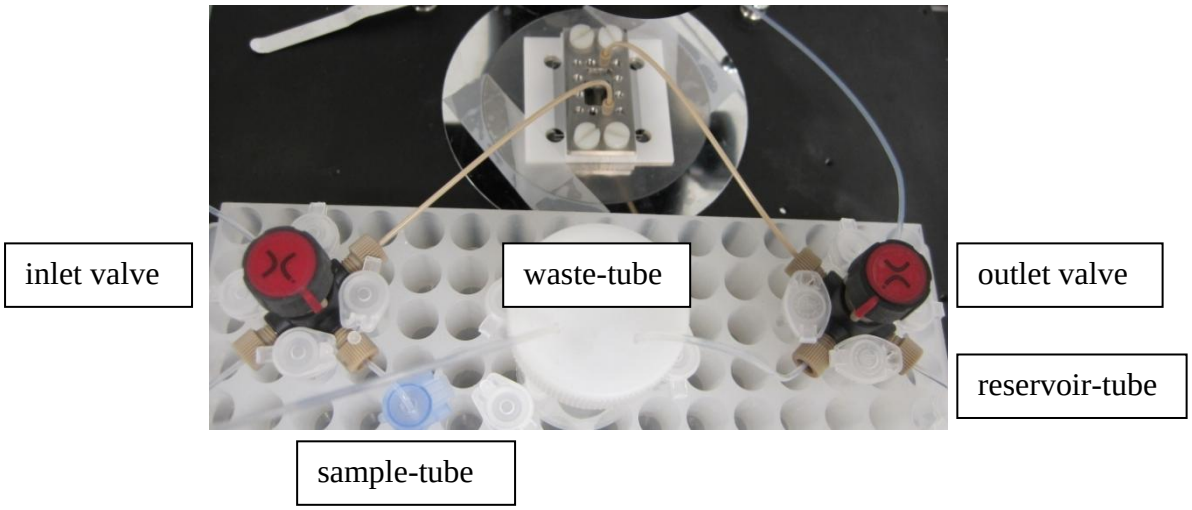

Fig. 37: Microfluidic setup comprising of the SU8 microchip, the in- and outlet valve, and several tubes (sample, reservoir and waste). The valves are switched to the withdrawing mode.

After 10 minutes, the outlet valve was switched as well in order to perform the static S-layer recrystallization overnight, while an ice block was provided to the mounting station. In the meantime, the syringe pump was running to avoid air bubble formation within the system; the injection was lead to the waste-tube, while the withdrawing syringe was filled with PBS from the reservoir-tube (peripheral mode). After S-layer recrystallization, the ice block was removed and unbound S-layer protein was washed off by rinsing the channel (valves were switched) with PBS at a flow rate of 50 µL/min via the syringe pump for 10 minutes. While washing, 700 µL of 2 µg/mL CD3-Ab in PBS were applied to a new sample-tube. After washing, the inlet valve was switched to waste in order to withdraw the CD3-Ab from the sample-tube into the channel (withdrawing mode). After 10 minutes, the outlet valve was switched as well for static performance of the CD3-Ab immobilization for 2 hours at room temperature. In the meantime, peripheral mode was applied. To finish the microchip modification, the valves were switched and the microchannel was rinsed again with PBS at a

flow rate of 50 µL/min for 10 minutes. The second microchannel was modified under the same conditions.

3.6.5.3 Microfluidic Jurkat cell capture in modified SU8 microchips

The Jurkat cell capture experiments in rSbpA/ZZ and CD3-Ab modified SU8 microchips were performed operating in two different modes: the cell-injecting and the cell-withdrawing mode. The cell-injecting mode was carried out manually, while the cell-withdrawing mode was performed via the syringe pump.

3.6.5.3.1 The cell-injecting mode

While rinsing the prior modified microchip with PBS, the sample-tube was removed and replaced by a 1 mL syringe filled with an excess of Jurkat cells. In- and outlet valves were switched to peripheral mode and the flow rate was decreased to 1 µL/min. The cells were injected manually via the filled syringe. When the cells reached the channel, which could be observed via the microscope, the valves were switched again to perform the cell capture at a flow rate of 1 µL/min. After waiting for 15 minutes, the flow rate was gradually decreased up to 5 µL/min to remove all cells out of the microchannel.

3.6.5.3.2 The cell-withdrawing mode

While rinsing the prior modified microchip with PBS, a new sample-tube was filled with an excess of Jurkat cells and connected to the inlet valve via a tube. The inlet valve was switched in order to withdraw the Jurkat cells into the microchannel (withdrawing mode). When the cells reached the channel, which could be observed via the microscope, the flow was decreased to 1 µL/min and the inlet valve was switched again in order to perform the Jurkat cell capture. After waiting for 15 minutes, the flow rate was gradually decreased up to 5 µL/min to remove all cells out of the microchannel.

3.7 Cell capture detection via light scattering

In order to detect and quantify the amount of captured Jurkat cells, light scattering (LS) experiments were performed in terms of an analytical approach. The scattered light detected and converted to the according current by organic photodiodes should provide information about the amount of captured cells and its relation to the detection signal to obtain a calibration curve for Jurkat cell capture experiments.

3.7.1 Fundamentals of organic photodiodes

A photodiode is a type of photodetector capable of converting light into either current or voltage, depending on the mode of operation. The common, traditional solar cell used to generate electric solar power is a large area photodiode (89).

Organic photodiodes (OPDs) offer the best potential for future LOC technology, as they are inexpensive, easily fabricated, have a large dynamic range and are highly sensitive. The combination of simple low-cost fabrication methods, including spin-coating, inkjet printing, and spray-coating, and the availability of diverse substrate materials, such as glass or flexible plastic, represent key advantages of organic semiconductor detectors over their silicon-based counterparts. In addition, expensive cameras or high precision scanning stages are no longer necessary, as the readout can be fully integrated with the sensor surface. Also, the short optical pathway associated with integrated OPDs minimizes the loss of optical signal and allows highly sensitive detection measurements, even without collection lenses (69). OPDs offer significant advantages in comparison to solid-state devices, such as large active areas, a variety of geometrical degrees of freedom, low temperature processing, and adjustable spectral sensitivity. To exploit all these advantages, a fast fabrication process for large active areas such as printing or spray deposition is inevitable. In addition to the ease of fabrication, OPDs have to show low dark currents and high external quantum efficiency to be competitive with solid-state detectors. Spray coating can be considered as the most flexible processing technique, but the high surface roughness of spray-coated thin films may deteriorate OPDs' properties. A layer stack of the OPD is shown in Fig. 38, a. Eight OPDs with an active area of 4 mm^2 each processed on top of a 5x5 cm^2 glass substrate with both spray-coated hole conductor (HC) and bulk heterojunction (BHJ) layers are shown in Fig. 38, b, (90).

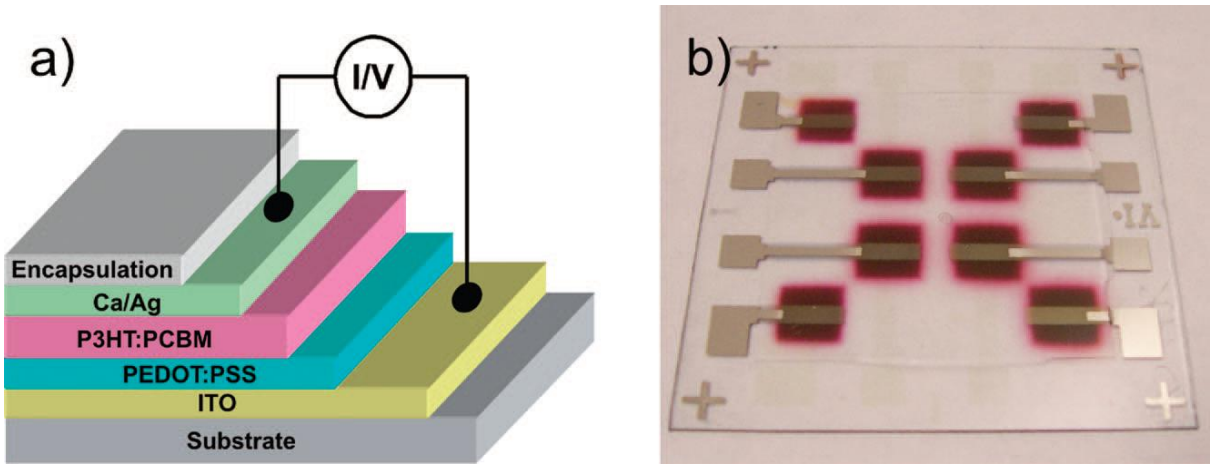

Fig. 38: OPD layout with glass encapsulation.
a) Layer stack of the OPD with ITO (indium-tin-oxide) as bottom contact, PEDOT:PSS (poly(3,4-ethylenedioxythiophene) poly(styrenesulfonate)) as hole conducting interlayer, rr-P3HT:PCBM (regioregular poly(3-hexylthiophene): 6,6-phenyl C_{61} butyric acid methyl ester = 1:0.75) as BHJ, and semitransparent Ca/Ag as top contact. b) Image of eight fully spray coated OPDs with an active area of 4 mm^2 each (90).

3.7.2 Light scattering detection setup

The LS experiments were performed in a construction further named “Siemens-Box” (Fig. 39) provided by AIT. A 488 nm laser beam (P=20 mW) is emitted by a light source, decreased by a neutral density filter (ND=1.0) and defined to a diameter of 1 mm by an aperture (Fig. 40).

Fig. 39: Siemens-Box consisting of light source, neutral density filter, aperture, microchip mounting station, notch filter and OPDs.

The light gets scattered when hitting the cells, whereas the scattering angle is dependent of the cell morphology. At scattering angles higher than 20° (filtered by a 488 nm notch filter), the light is detected and converted to the correlating current by the OPDs. The current signal relates in turn to the amount of cell coverage. A schematic of the LS setup is depicted in Fig. 40.

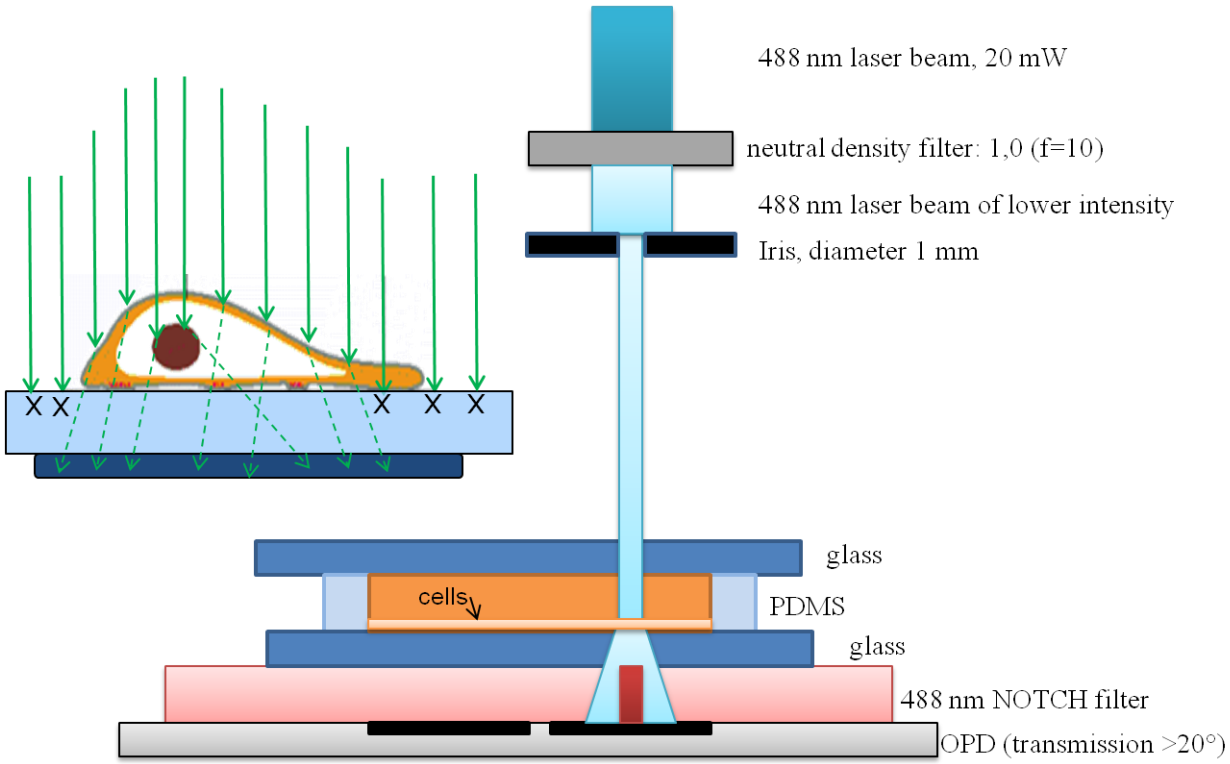

Fig. 40: Schematic of the LS setup for the detection of Jurkat cell capture.
Jurkat cells were captured on glass slides prior modified with rSbpA/ZZ protein and CD3-Ab. A 488 nm laser beam is decreased by a neutral density filter and defined to a diameter of 1 mm. When hitting the cells, the light is scattered, whereas light scattered more than 20° (filtered by a 488 nm notch filter) is detected and converted to the correlating current by the OPDs.

3.7.3 Jurkat cell capture in modified PDMS reservoirs

Glass cover slides with applied PDMS reservoirs (length: 15 mm, width: 10 mm, height: 3 mm, A=1.5 cm^2, V=450 µL; provided from AIT) were modified with rSbpA/ZZ and CD3-Ab as described in chapter 3.5.3. As declared in chapter 4.4.1, around $2.9x10^5$ Jurkat cells/cm^2 can be captured. 450 µL containing around $4.35x10^5$ Jurkat cells ($9.67x10^5$ cells/mL) had to be applied to the reservoir with an area of 1.5 cm^2 to achieve a coverage of 100%. Jurkat cells were counted with Countess™, centrifuged and diluted to several concentrations between 10% and 100% of cell coverage. The volume added to the reservoir was 500 µL to avoid air bubbles when covering the reservoir with another glass slide. The different concentrations

were added to the reservoirs and observed under the microscope (Wilovert AFL, hund Wetzlar) to control the distribution and regularity of cell coverage.

3.7.4 LS measurements for Jurkat cell capture detection

The PDMS reservoirs with different amounts of captured Jurkat cells were positioned in the Siemens-Box. To determine the light scattering in the Siemens-Box, at least a repeat determination per sample was measured. As blank, the medium without cells was measured in an identically modified PDMS reservoir.

4 Results and Discussion

4.1 AFM imaging of recrystallized rSbpA/ZZ lattice

The S-layer fusion protein rSbpA/ZZ was recrystallized on various surfaces such as gold prior coated with thiolated SCWP, glass and SU8 in order to visualize the quality of the rSbpA/ZZ lattice by AFM measurements. In former research work at DNBT, rSbpA/ZZ was recrystallized on PS (polystyrene) and studied by AFM as well. The S-layer fusion protein recrystallized into a monolayer consisting of numerous randomly oriented patches (Fig. 41). All patches exhibit the square lattice structure (p4). According to Völlenkle et al. 2004, the center-to-center spacing of the morphological units amounts to 13.1 nm (33).

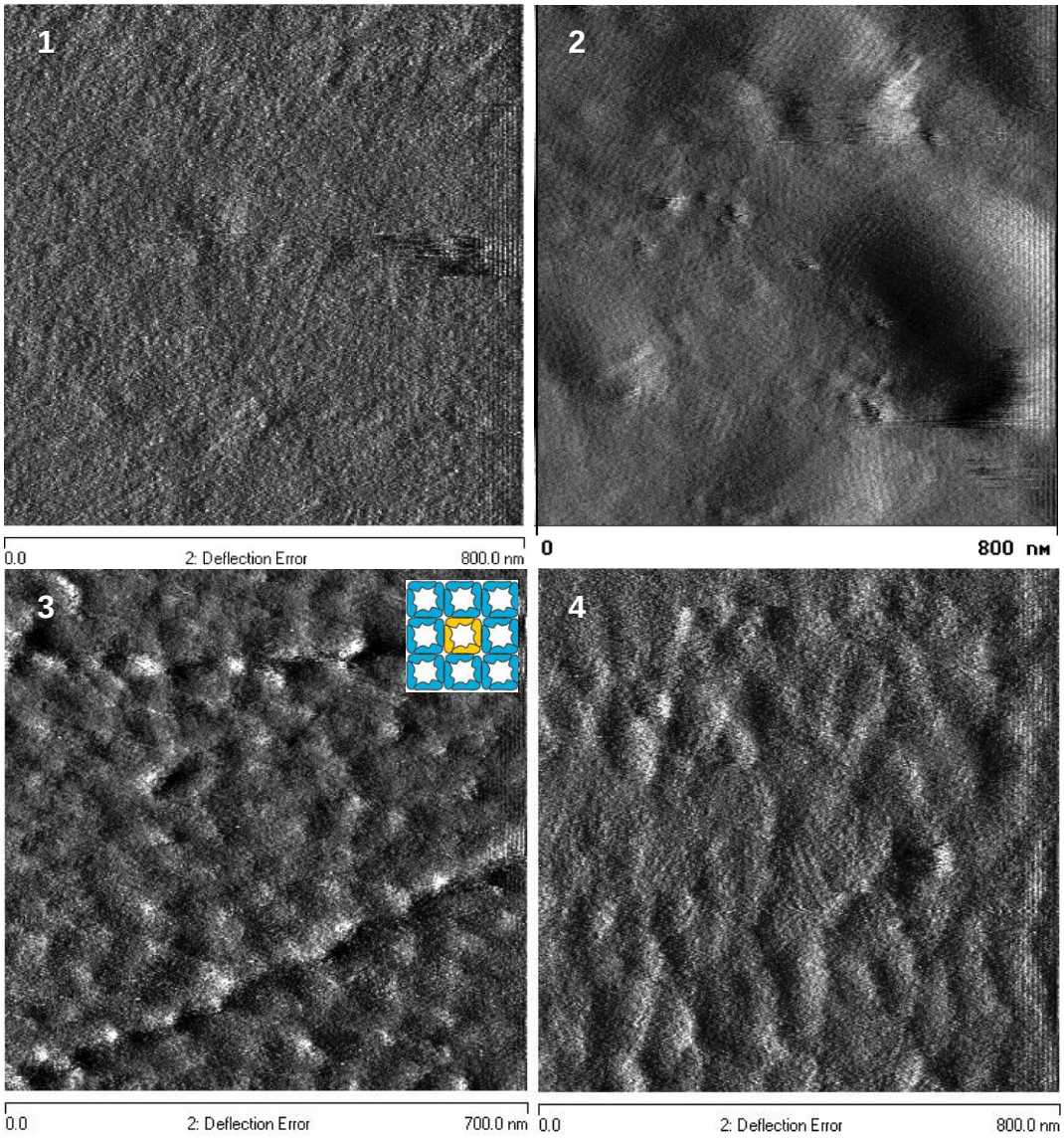

Fig. 41: AFM images of the recrystallized S-layer fusion protein rSbpA/ZZ.
The S-layer fusion protein recrystallized on 1) gold precoated with thiolated SCWP, 2) PS (by courtesy of DNBT) 3) glass and 4) SU8 reveals randomly oriented patches with square lattice structure (p4, insert).

4.2 Enzyme linked immunosorbent assay

4.2.1 SbpA and rSbpA/ZZ recrystallization and preparation for the immobilization of human IgG

The S-layer wild type protein SbpA and the S-layer fusion protein rSbpA/ZZ were recrystallized on ELISA plates and prepared for the human IgG immobilization. The fusion protein rSbpA/ZZ presents an IgG affinity matrix (33) and therefore doesn't need any special preparation. Due to the fact that SbpA doesn't contain any IgG affinity sequence and hence a chemical immobilization is required, several preparation steps such as crosslinking with glutardialdehyde and activation with EDC are necessary (79). Therefore, the modification and preparation of supports for antibody immobilization can be performed much more convenient with the S-layer fusion protein rSbpA/ZZ providing several advantages such as reduction in time and reagent consumption.

4.2.2 Detection of human IgG immobilization on SbpA and rSbpA/ZZ

Defined concentrations of human IgG ranging from 1000-8 ng/mL were immobilized on SbpA and rSbpA/ZZ coated ELISA plate wells. A secondary antibody linked to an enzyme (anti human IgG peroxidase (POD)) was detected by oxidizing the substrate TMB under color development which was colorimetrically measured at 450 nm. Difficulties occurred when providing the substrate solution to the enzyme POD, which reacted too rapidly in rSbpA/ZZ modified and at the same time too slowly at SbpA treated wells. To compare the efficiency of the human IgG immobilization on SbpA and rSbpA/ZZ, the enzyme reaction has to be carried out simultaneously. Hence, the optimal moment for stopping the enzyme reaction could be achieved neither for the SbpA- nor for the rSbpA/ZZ-setup. Despite of difficulties during the enzyme reaction, the results shown in Fig. 42 provide information about the sensitivity between human IgG and rSbpA/ZZ. A strong affinity between human IgG and rSbpA/ZZ and its complete saturation at a human IgG concentration of 1000 ng/mL could be observed, which correlates also with prior studies at DNBT (communication with A. Breitwieser). In terms of ELISA as antibody detection method, the chemical immobilization of human IgG on SbpA is too inefficient to be simultaneously compared to the human IgG immobilization on rSbpA/ZZ presenting a specific IgG affinity matrix.

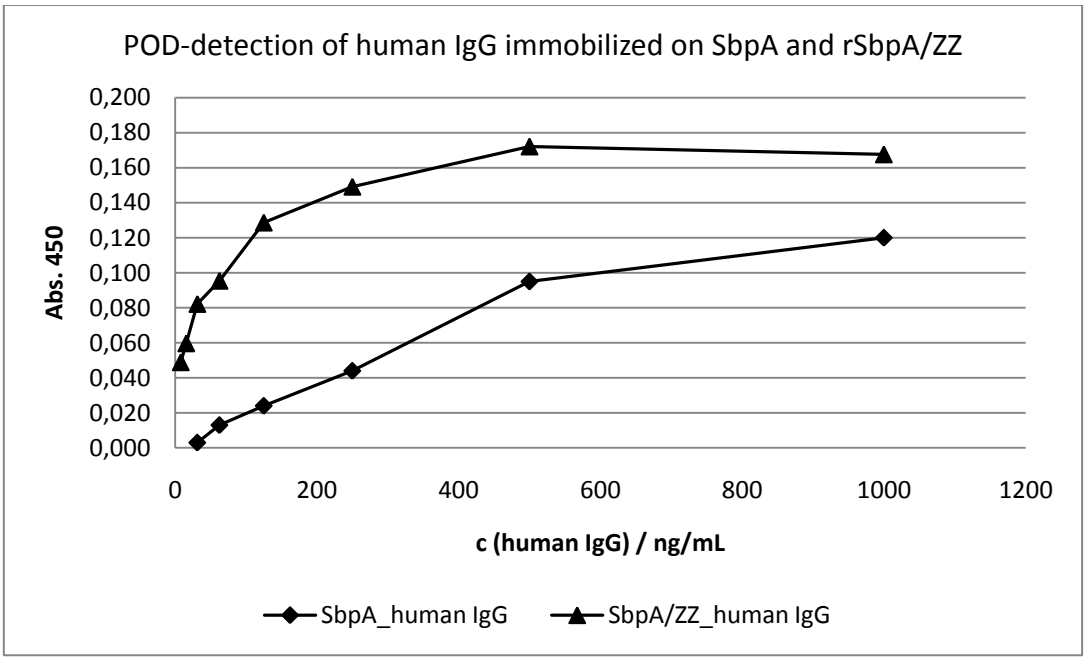

Fig. 42: Detection of human IgG immobilized on SbpA and rSbpA/ZZ.
The results indicate a strong affinity between human IgG and rSbpA/ZZ and its complete saturation at a concentration of 1000 ng/mL.

4.2.3 Optimization of human IgG detection on rSbpA/ZZ

In order to present an alternative to the too rapidly reacting enzyme POD, the secondary antibody anti human IgG linked to alkaline phosphatase (ALP), a slower reacting enzyme, was provided to indirectly detect the immobilization of human IgG to rSbpA/ZZ by photometrical measurements at 405 nm. Further, human IgG and rSbpA/ZZ were optionally crosslinked with DMP in order to introduce covalent bonds between the components (33). The results shown in Fig. 43 illustrate the strong affinity between human IgG and rSbpA/ZZ detectable from a human IgG concentration of 6 ng/mL (Table 11).

Table 11: Detection signals of human IgG immobilized on rSbpA/ZZ. Optionally crosslinked with DMP, measured at 405 nm.

concentration (human IgG) / ng/mL	Abs. 405 nm, (rSbpA/ZZ, human IgG)	Abs. 405 nm, (rSbpA/ZZ, human IgG, DMP)
500	0.233	0.233
167	0.113	0.115
55.6	0.056	0.055
18.5	0.031	0.030
6.17	0.017	0.018

At human IgG concentrations higher than 50 ng/mL, the signal increase is gradually reduced with increasing the human IgG concentration. At a human IgG concentration of 500 ng/mL,

the saturation point is nearly reached. Including the results from chapter 4.2.2, all further static IgG immobilization experiments were performed with an IgG excess-concentration of 2 µg/mL to guarantee complete saturation of the antibody immobilization on the S-layer protein. The introduction of covalent bonds between rSbpA/ZZ and human IgG by supplying the crosslinking reagent DMP doesn't reveal any negative impacts regarding the human IgG activity. The comparison of the crosslinked and non-crosslinked setup results in nearly identical human IgG detection signals (Table 11).

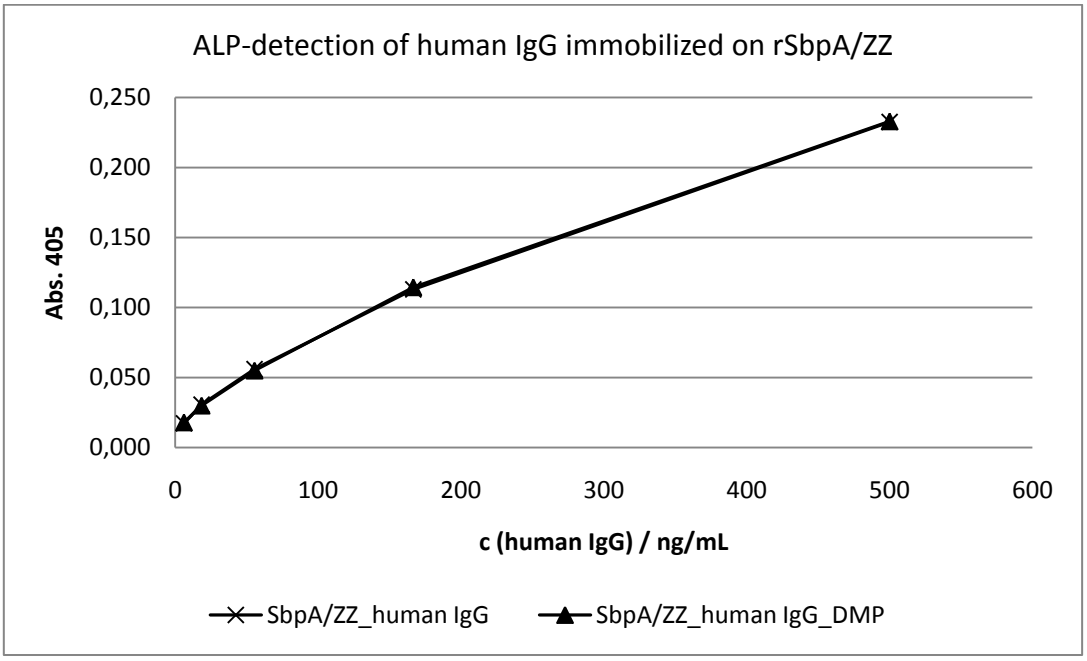

Fig. 43: ALP-detection of human IgG immobilized on rSbpA/ZZ.
The results affirm the strong affinity between human IgG and rSbpA/ZZ.

4.3 Surface Plasmon Resonance

4.3.1 Recrystallization of the S-layer proteins SbpA and rSbpA/ZZ

To investigate and compare the recrystallization behavior of the S-layer proteins SbpA (wild type) and rSbpA/ZZ (fusion protein) generated by oriented recrystallization of the S-layer proteins on gold chips precoated with thiolated SCWP, SPR studies were performed. Recrystallization of the SbpA and rSbpA/ZZ proteins led to an increase of ~5130 RU corresponding to 5.13 ng/mm^2 and 4.3x10^5 nM/mm^2 which is in good accordance to Völlenkle et al. 2004 (33) (Fig. 44).

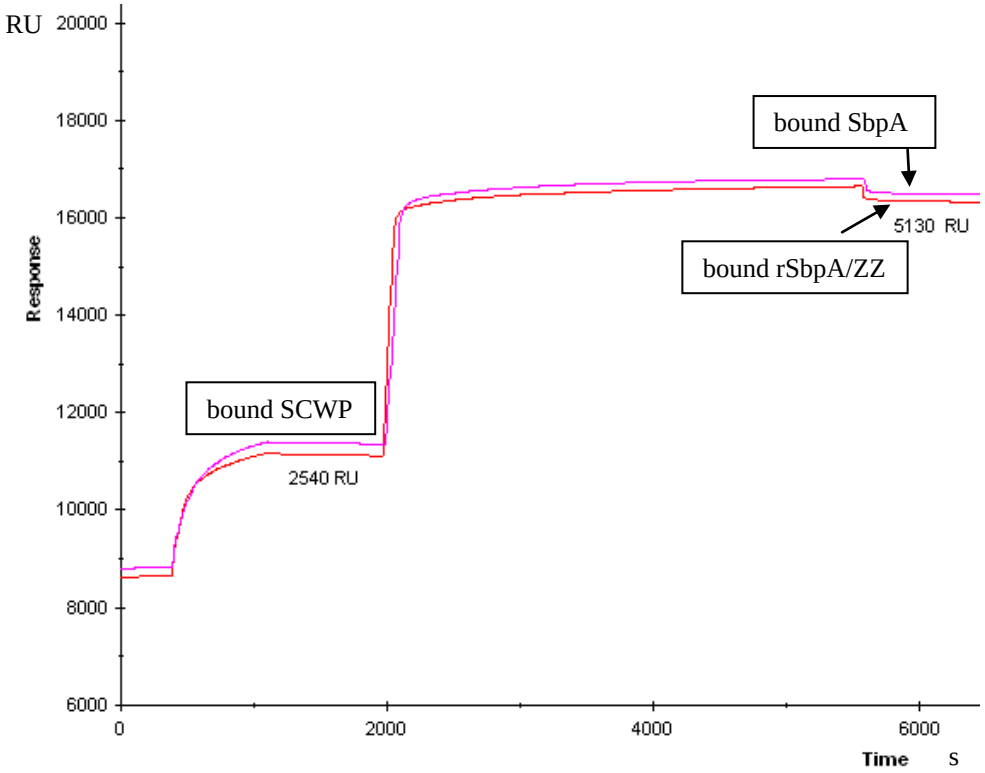

Fig. 44: SPR-sensorgram showing the binding of the S-layer proteins SbpA (pink) and rSbpA/ZZ (red) on gold precoated with thiolated SCWP.
The recrystallization reveals an increase of ~5130 RU corresponding to 4.3x10^5 nM/mm^2 for both S-layer proteins.

4.3.1.1 Antifouling properties of rSbpA/ZZ

In terms of the known antifouling properties of S-layer proteins against unspecific protein adsorption (26), the S-layer wild type protein SbpA revealed excellent antifouling properties against human full-plasma on SPR gold sensor chips in comparison to other antifouling materials such as PEG (91). Assuming that the S-layer fusion protein rSbpA/ZZ, containing an IgG affinity matrix, would bind IgGs from a full-plasma sample, IgG-free plasma samples

were produced via a protein G column. Supplying the different human plasma samples, the antifouling properties of the S-layer fusion protein rSbpA/ZZ recrystallized on gold precoated with thiolated SCWP in comparison to gold were studied in SPR. The full-plasma treatment of rSbpA/ZZ and gold affirmed the assumption of binding IgGs from full-plasma leading to an increase of ~6840 RU and ~4400 RU, respectively (Fig. 45). The amount of ~6480 RU bound to rSbpA/ZZ is significantly higher than data of human IgG bound to rSbpA/ZZ (~4400 RU) published by Völlenkle et al. 2004 (33). This indicates that due to the high affinity of human IgG to rSbpA/ZZ, also other plasma components are included unspecifically in the immobilization on the S-layer fusion protein.

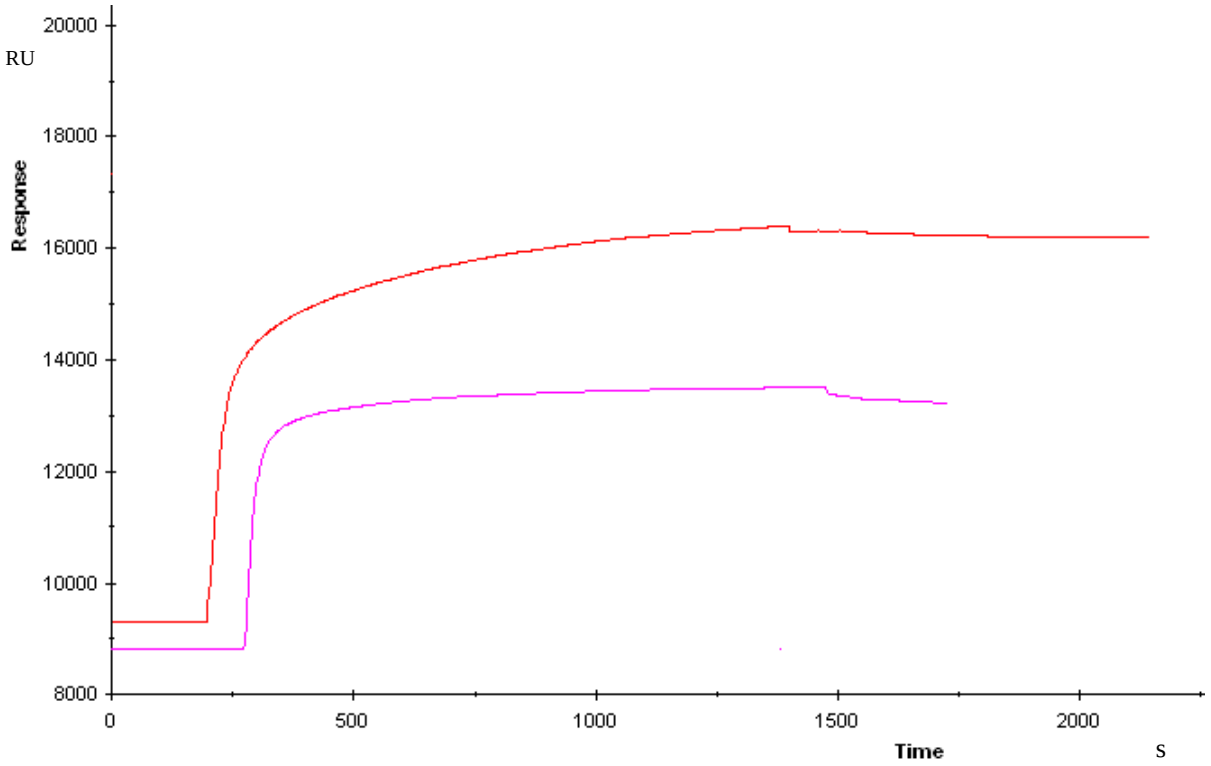

Fig. 45: Investigation of the rSbpA/ZZ antifouling properties compared to gold against full-plasma. The full-plasma treatment of the S-layer fusion protein rSbpA/ZZ (red, recrystallized on thiolated SCWP bound to gold) and gold (pink) resulted in an increase of ~6840 RU and ~4400 RU, respectively.

The IgG-free plasma treatment of the rSbpA/ZZ protein didn't lead to any increase of response units, while resulting in an increase of ~2900 RU on gold (Fig. 46) affirming that the antifouling properties of the native SbpA protein are generally maintained in the S-layer fusion protein rSbpA/ZZ, aside from the IgG binding to the ZZ-sequence.

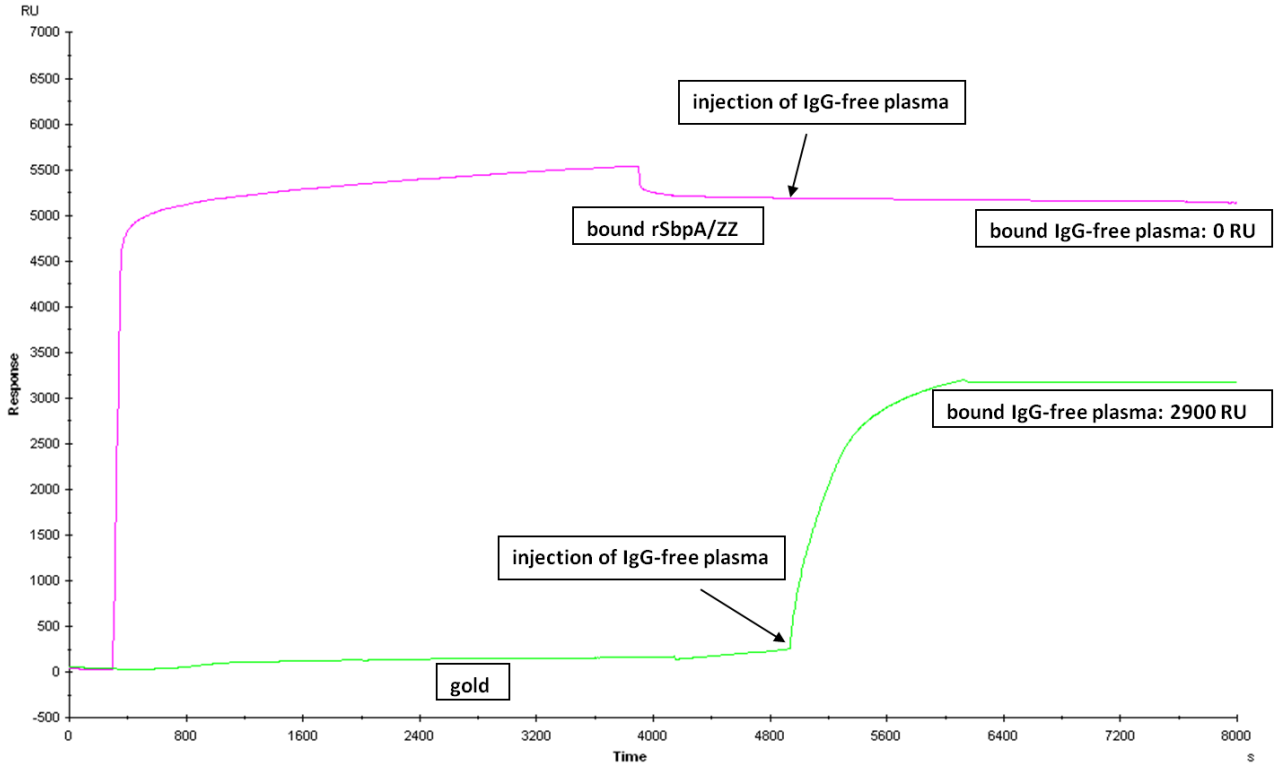

Fig. 46: Investigation of the rSbpA/ZZ antifouling properties compared to gold against IgG-free plasma. The IgG-free plasma treatment of the S-layer fusion protein rSbpA/ZZ (recrystallized on thiolated SCWP bound to gold) resulted in no signal increase (pink) while it led to an increase of ~2900 RU on gold (green).

4.3.2 Binding of human IgG and CD3-Ab to rSbpA/ZZ

According to Völlenkle et al. 2004, SbpA does not bind any IgG (33) and was therefore excluded from all further antibody experiments. To investigate and compare the immobilization capacity of human IgG and CD3-Ab on the rSbpA/ZZ protein by SPR experiments, the antibody samples were supplied to gold sensor chips precoated with thiolated SCWP and rSbpA/ZZ protein. The antibody CD3-Ab immobilized on rSbpA/ZZ should provide an affinity matrix to capture CD3-cells in further experiments. The immobilization of human IgG and CD3-Ab led to an increase of ~5100 RU and ~4200 RU, respectively (Fig. 47). The reason for the difference in the amount of immobilized antibodies may be that the affinity of protein A is the strongest to human IgG, while the CD3-Ab is produced in mouse. However, the immobilization of CD3-Ab leading to ~4200 RU which corresponds to 2.85×10^5 nM/mm^2 is in good accordance to the data of the immobilization of human IgG published by Völlenkle et al. 2004 (33) and provides a reliable and stable affinity matrix for the capture of CD3-cells.

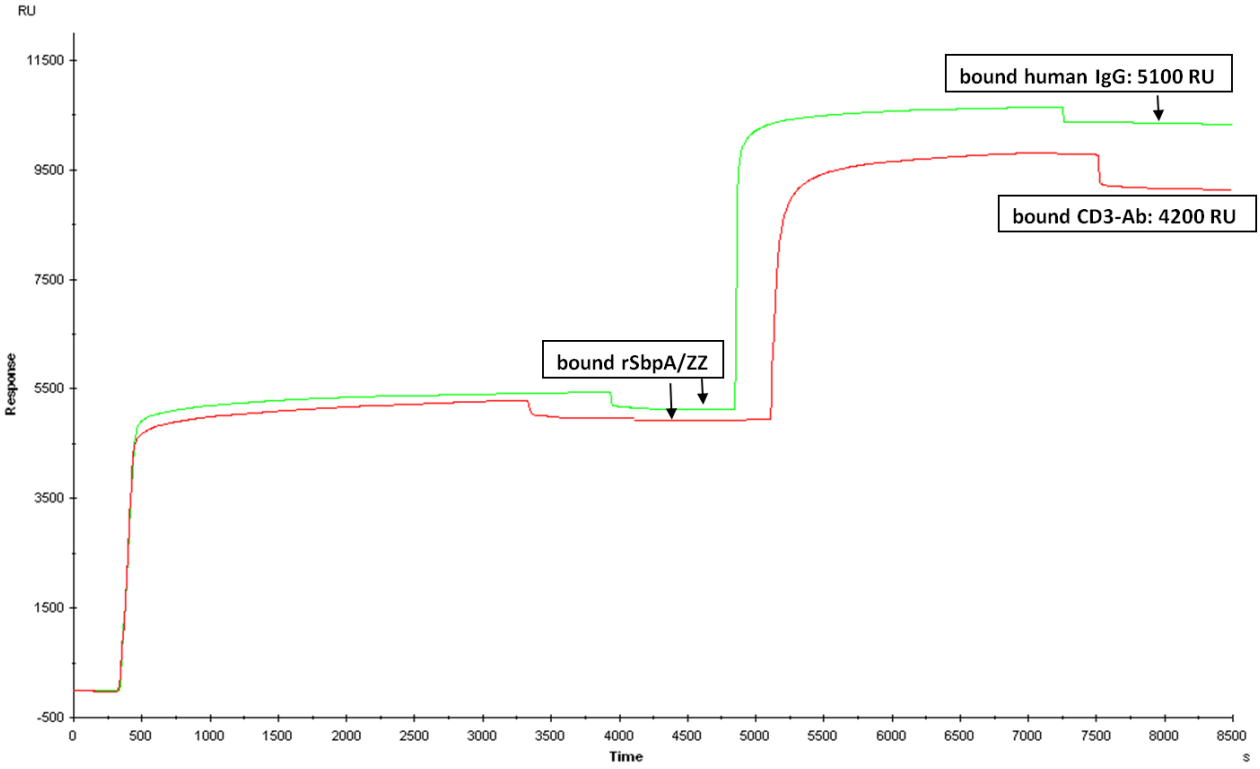

Fig. 47: SPR-sensorgram showing the immobilization of human IgG and CD3-Ab on rSbpA/ZZ protein. The binding of human IgG and CD3-Ab to rSbpA/ZZ led to an increase of ~5100 RU (green) and ~4200 RU (red), respectively.

4.3.2.1 Antifouling properties of rSbpA/ZZ with immobilized CD3-Ab

To extend the antifouling investigation of the recrystallized rSbpA/ZZ protein, the antifouling properties of the CD3-affinity matrix were studied in comparison to gold. The CD3-affinity matrix was produced by immobilizing the CD3-Ab on the rSbpA/ZZ protein followed by crosslinking with DMP to inhibit the replacement of CD3-Ab by plasma-IgG. The CD3-affinity matrix and the gold were treated with IgG-free plasma and full-plasma. The IgG-free plasma treatment of the CD3-affinity matrix didn't lead to any increase of the response signal (graph not shown) while resulting in a response signal of ~2950 RU on gold correlating to Fig. 46. The negative response of the CD3-affinity matrix to IgG-free plasma affirms that the antifouling properties of the S-layer fusion protein against IgG-free plasma are maintained after antibody immobilization and DMP crosslinking. The full-plasma treatment of the CD3-affinity matrix and gold led to an increase of ~750 RU and 3900 RU, respectively (Fig. 48). Even though the CD3-affinity matrix gives response to full-plasma, the signal is very low compared to the response of gold. In summary, the CD3-affinity matrix is not affected by IgG-free plasma and reveals only a weak response to full-plasma. For this, affinity matrices based on rSbpA/ZZ provide useful antifouling properties and feature a promising approach for the realization of antibody and cell capture from suspension as well as from blood.

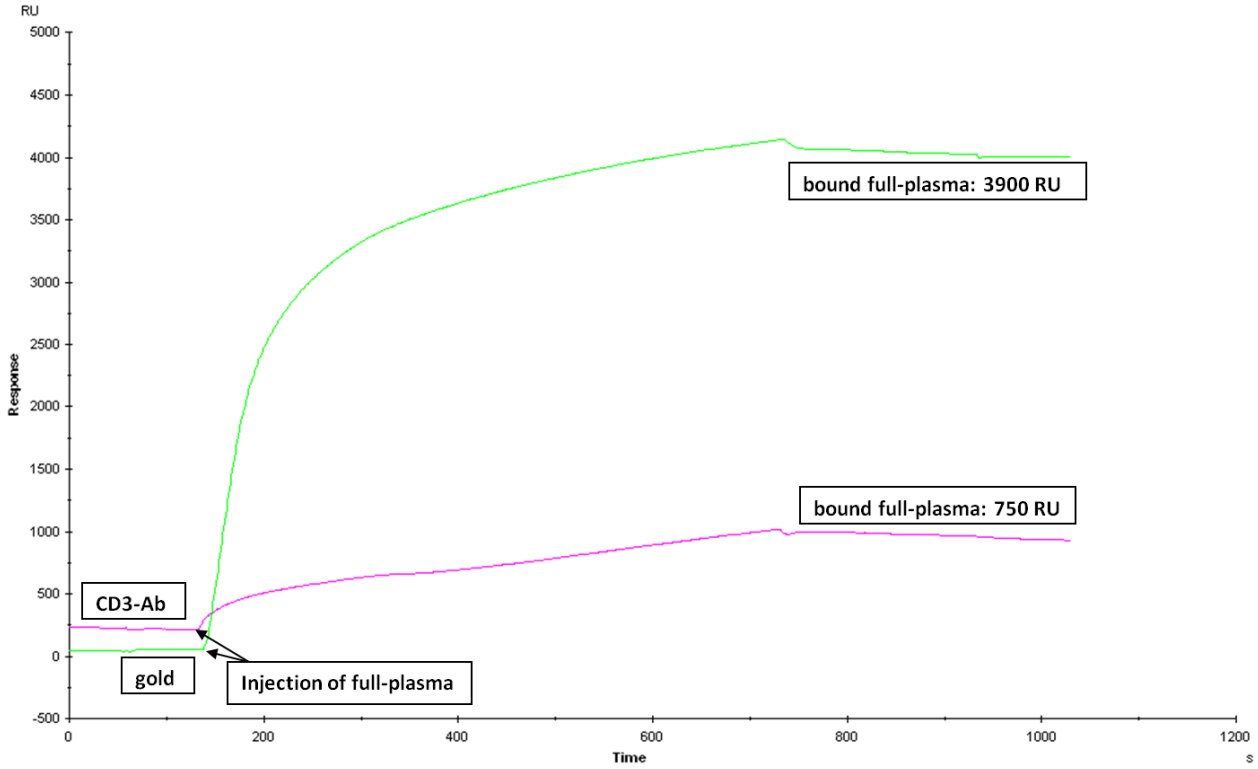

Fig. 48: Binding of full-plasma to the CD3-affinity matrix (pink) and gold (green) leading to an increase of ~750 RU and ~3900 RU, respectively.

The results affirm the preservation of the rSbpA/ZZ antifouling properties after antibody immobilization and DMP crosslinking.

4.4 Static cell capture

4.4.1 Jurkat cell capture via CD3-Ab immobilized on rSbpA/ZZ protein

Glass cover slides were functionalized with rSbpA/ZZ protein and CD3-Ab to offer an affinity matrix for the capture of Jurkat cells. The goal was to determine the amount of captured cells per cm^2. A statistic number of captured Jurkat cells was determined out of 10 cover slide samples; $2.9x10^5$ Jurkat cells/cm^2 could be captured on glass cover slides prior modified with rSbpA/ZZ and CD3-Ab (Fig. 49, 1). Relating to the average Jurkat cell diameter of 20 µm, a capture efficiency higher than 90% could be achieved, which confirms the operational reliability of the affinity matrix composed of the S-layer fusion protein rSbpA/ZZ and the IgG-antibody CD3-Ab. On cover slides only modified with rSbpA/ZZ, no capture of Jurkat cells was observed (Fig. 49, 2).

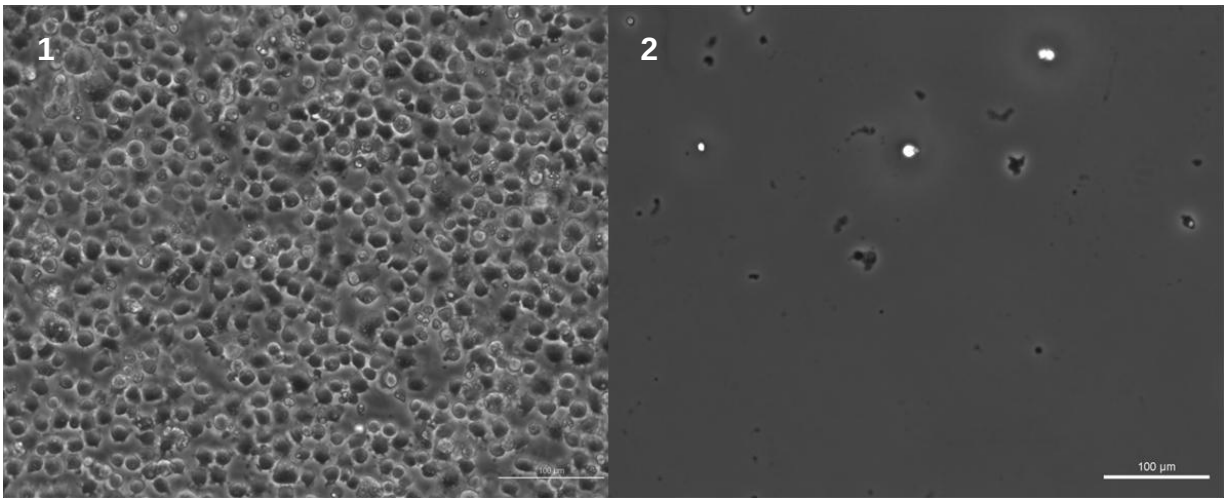

Fig. 49: Light microscope images of Jurkat cells captured via CD3-Ab immobilized on rSbpA/ZZ.
1) Determination of the cell capture efficiency: $2.9x10^5$ captured Jurkat cells per cm^2 result in a capture efficiency higher than 90%. 2) No cell capture was observed on glass cover slides only modified with rSbpA/ZZ. Scale bars: 100 µm.

4.4.2 Specific Jurkat cell capture from a cell mixture of Jurkat and MOLT 3 cells via CD3-Ab immobilized on rSbpA/ZZ

For the efficiency of the Jurkat cell capture on the S-layer-antibody-matrix could be proved as described above, the specificity of the cell capture was a further field of interest. Hence, several mixtures of differently labeled Jurkat and MOLT 3 cells were supplied to glass cover slides prior modified with rSbpA/ZZ protein and CD3-Ab. Fig. 50 shows pictures of the differently labeled Jurkat and MOLT 3 cells.

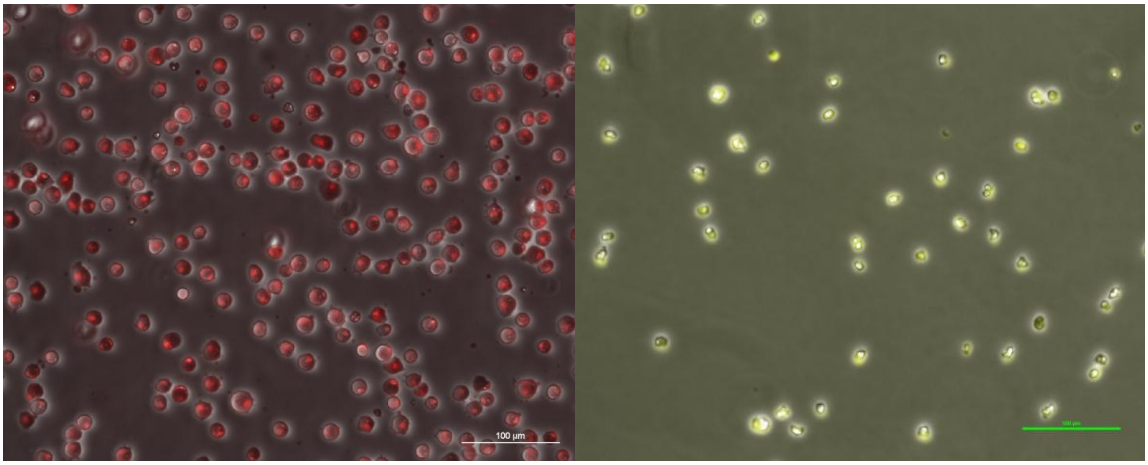

Fig. 50: (left) Labeled Jurkat cells, (right) labeled MOLT 3 cells, scale bars: 100 µm.

The results shown in Fig. 51 illustrate that only Jurkat cells could be captured via the CD3-Ab. Further, the impact of cell density could be visualized by supplying different cell mixtures with contents of 100%, 50% and 20% Jurkat cells. Consequently, the results affirm the specific CD3-cell capture via the CD3-Ab immobilized on the rSbpA/ZZ protein, which offers a valuable alternative to the chemical immobilization of antibodies on surfaces as well as on interfaces. The IgG-affinity matrix provided by the S-layer fusion protein rSbpA/ZZ indicates the possibility of capturing any cell type via a cell specific IgG-antibody immobilized on the rSbpA/ZZ fusion protein.

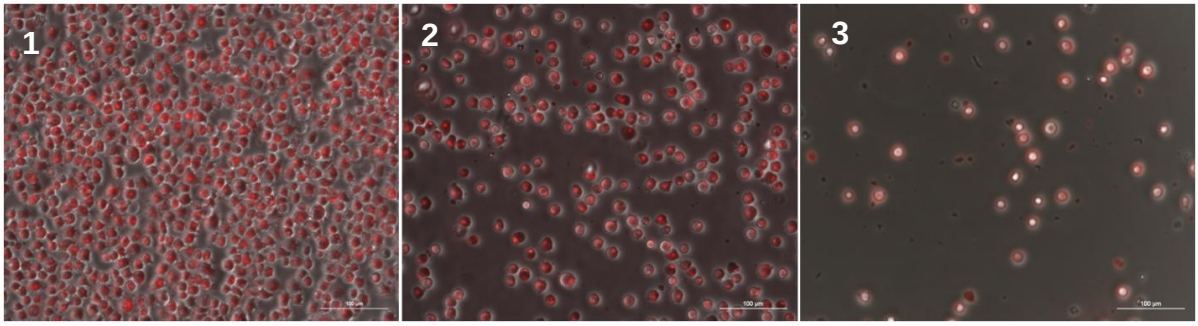

Fig. 51: Specific capture of Jurkat cells from cell mixtures via CD3-Ab immobilized on rSbpA/ZZ.
1) Captured Jurkat cells from a cell suspension with 100% Jurkat cells. 2) Captured Jurkat cells from a cell mixture with 50% Jurkat and 50% MOLT 3 cells. 3) Captured Jurkat cells from a cell mixture with 20% Jurkat and 80% MOLT 3 cells. Scale bars: 100 µm.

4.5 Microfluidic cell capture

4.5.1 Static modification of PDMS microchips with rSbpA/ZZ and CD3-Ab

The static modification of microchannels by supplying the reagents via a micropipette is a simple and reliable tool for microchip modification. As long as the pipette tips, plugged to the in- and outlet ports, were filled with reagent or buffer, no air bubbles occurred within the system. Problems came up when connecting the in- and outlet ports to the tubes of the syringe pump system. During this step, air bubbles can easily get into the microchannel which can cause damage to the S-layer-antibody matrix if no liquid is supplied in sufficient time.

4.5.2 Microfluidic Jurkat cell capture in modified PDMS microchips

Jurkat cell capture experiments were performed in PDMS fabricated microchips prior modified with rSbpA/ZZ protein and CD3-Ab. The cell-seeding procedure described in chapter 3.6.4.3 presents a useful tool to manually withdraw cells into the microchannel, while the flow via the syringe pump is stopped, even though attention is demanded to avoid the appearance of air bubbles in the system. Fig. 52 shows 1) the cell seeding, 2) the cell capture and 3) the microchannel after the cell removal.

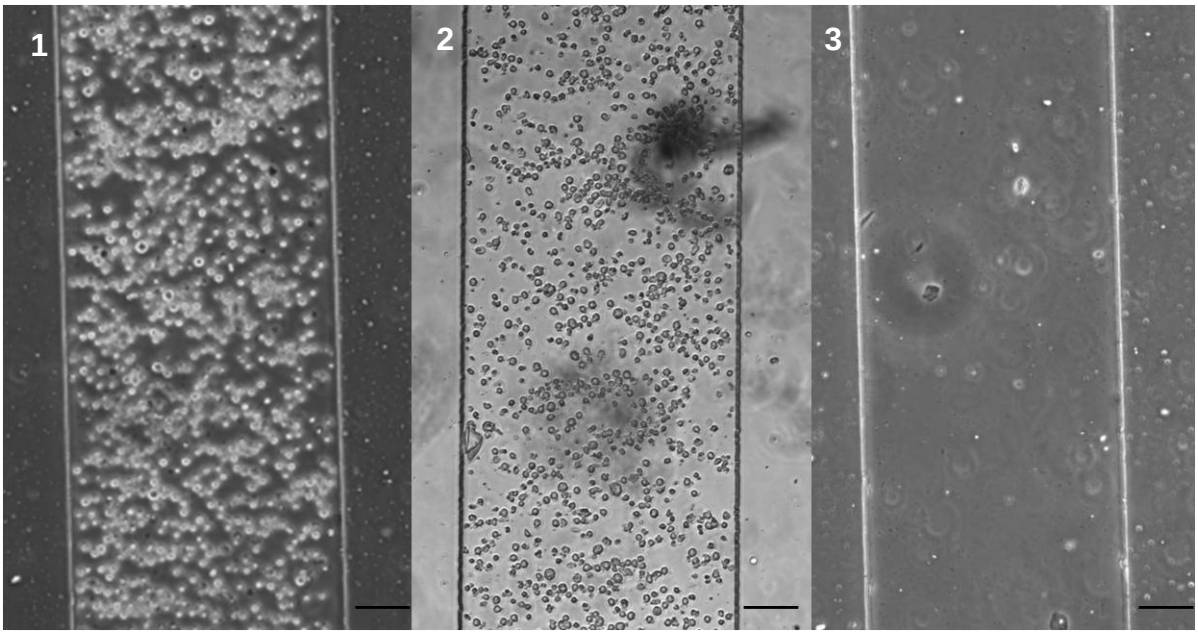

Fig. 52: Microfluidic Jurkat cell capture via CD3-Ab immobilized on the rSbpA/ZZ coated microchannel. 1) Manual Jurkat cell seeding. 2) Jurkat cell capture at flow rates from 0.1-0.5 µL/min. 3) Microchannel after cell removal at a flow rate of 1 µL/min. Scale bars: 100 µm.

According to the cell capture and cell removing, the flow rates were 0.1-0.5 µL/min and 1 µL/min, respectively. The critical Jurkat cell capture flow rate resulting from the herein presented experiments is 0.5 µL/min. In unmodified or only rSbpA/ZZ modified

microchannels, no cell capture events were observed correlating with the results of chapter 4.4.1. Nevertheless, problems occurred after the cell capture when the flow was restarted to figure out the critical cell capture flow rate. Switching the L-valve to reconnect the syringe pump with the LOC system resulted in uncontrolled cell moving within the microchannel, interrupting the cell capture events. Therefore, the valve system needed to be improved to provide a stable peripheral setup without passing on uncontrollable forces to the microchannel. After restarting the flow, the cells started to move unrelated to the flow rate, which indicated that stopping and restarting the syringe pump while connected via the valve to the microchannel was no adequate method for providing a constant flow rate. In addition to the deficiencies in the peripheral equipment (L-valve and syringe pump), the elastomer PDMS can generally cause irregularities regarding the flow rate (92). Even in the absence of Jurkat cells, a pulsing flow was observed in the microchannel via the microscope. The microchip design (spider chip) itself was not appropriate for cell capture experiments; the small channel width of 500 µm led to rapid flow velocities and intensification of flow rate irregularities so that the cells were easily rinsed out.

In summary, improvements in peripheral equipment, polymer properties and microchannel design were required in order to provide a stable system for microfluidic cell capture experiments.

4.5.3 Static modification of SU8 microchips with rSbpA/ZZ and CD3-Ab

Contrary to the manual modification procedure used for PDMS microchips, SU8 microchips were connected to the syringe pump system from the beginning to perform also the modification steps via the syringe pump. The clear advantage was that no tube exchange had to be carried out. The in- and outlet ports of the microchip were continuously connected to the same tubes avoiding the occurrence of air bubbles in the system.

4.5.4 Microfluidic Jurkat cell capture in modified SU8 microchips

Due to the deficiencies that occurred during the cell capture experiments in PDMS fabricated microchips discussed above, an improved microfluidic cell capture approach was presented to offer a stable peripheral setup providing reliable flow rates. SU8 fabricated microchips were produced; the negative photoresist SU8 is a hard polymer and therefore represents a thermally and mechanically stable material. Based on the microfluidic design established by Cheng et al. 2007 (50), the channel width was increased from 500 µm to 3 mm in order to increase the capture surface and apply higher flow rates. Several stabilizing arrangements described in

chapter 3.6.5.2, such as the microchip mounting station and the injecting/withdrawing syringe pump system with two integrated and stabilized diagonal four-way valves led to a constructive peripheral setup for microfluidic cell capture (Fig. 53).

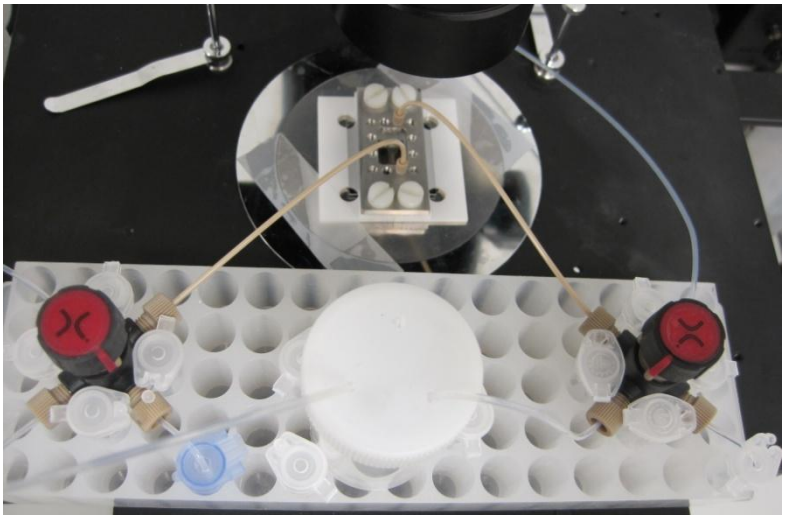

Fig. 53: Improved setup with microchip mounting station and two stabilized diagonal four-way valves.

The injecting/withdrawing syringe pump system decreased the pressure on the microchip due to simultaneous and uniform injecting and withdrawing. When switching the four-way valves, no observable forces were passed on to the microchannel, so that no interruption of cell capture events occurred. The four-way valves, offering additional operation modes (withdrawing and peripheral mode) aside from the injecting/withdrawing mode, represent an important tool in the herein presented setup. By switching the valves to peripheral mode, the flow is continued offside the microchannel. Hence, stopping the flow within the microchannel can be easily achieved by applying peripheral mode without stopping the flow itself, which guarantees a continuous and constant flow. Due to replacing PDMS by SU8, the flow-pulsing could be eliminated.

4.5.4.1 The cell-injecting mode

Performing the cell-injecting mode, Jurkat cells were manually injected into the prior modified microchannel via a syringe. The advantage of the manual cell-injecting mode is that the cells can be rapidly provided to the microchannel avoiding sinking and agglomerating within the syringe. Though, the channel walls were not stable enough to resist the high pressure applied by the manual injecting. Consequently, leakages and therefore air bubbles occurred in the channel making it impossible to determine the critical Jurkat cell capture flow rate. Despite the described difficulties, the Jurkat cells could be captured in the microchannel

prior modified with rSbpA/ZZ and CD3-Ab. 1) Seeding, 2) capture and 3) removal of Jurkat cells are shown in Fig. 54.

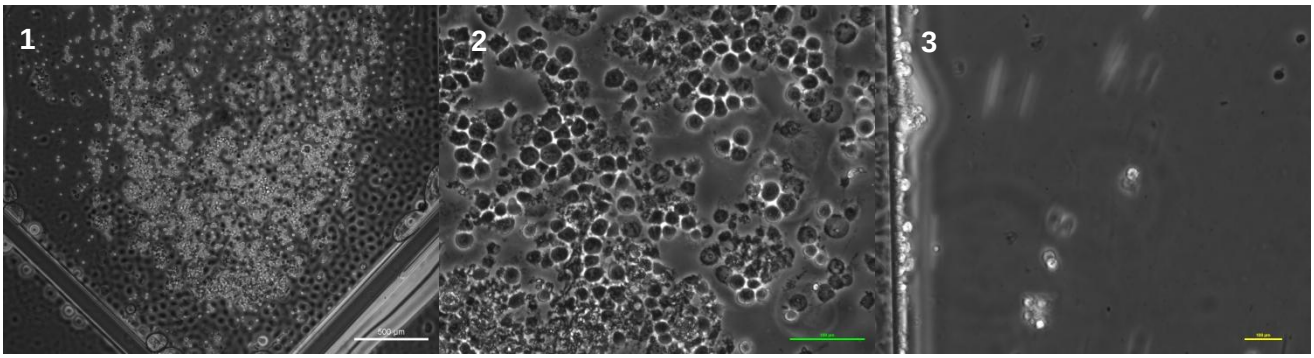

Fig. 54: Jurkat cell capture in modified SU8 microchips.
1) Jurkat cell seeding. Due to leakages air bubbles occurred at the channel wall. 2) Jurkat cell capture. 3) Jurkat cell removal. Scale bars: 1) & 2) 500 µm, 3) 100 µm.

4.5.4.2 The cell-withdrawing mode

Cells prefer withdrawing rather than injecting due to their physical character (personal communication with Dr. Michael Fischer, AKH, Vienna). Operating in the cell-withdrawing mode, Jurkat cells were supplied in a sample-tube and withdrawn into the prior modified microchip via the syringe pump. The advantage of the cell-withdrawing mode, compared to the cell-injecting mode, is that the withdrawing is performed under a controlled flow rate which should avoid leakages and air bubbles in the microchip. Contrary, Jurkat cells tend to sink and agglomerate in the sample-tube during the slow cell seeding and therefore require manual shaking treatment. Besides, the herein used SU8 microchips were produced at the very early state of their development. Therefore, they were not stable enough for cell seeding experiments yet leading to the occurrence of leakages and air bubbles. Despite this, the Jurkat cells could be captured in the microchannel via the CD3-Ab immobilized on the rSbpA/ZZ protein providing a promising approach for future microfluidic cell capture devices. The results for Jurkat cell seeding, capture and removal correlate with those depicted in Fig. 54.

4.6 LS measurements for Jurkat cell capture detection

In order to detect and analyze the Jurkat cell capture via the CD3-Ab immobilized on the rSbpA/ZZ protein, light scattering (LS) measurements in the Siemens-Box were performed with concentrations between 10% and 100% of cell coverage to investigate the relation between the detection signal and the amount of cell coverage. The different cell concentrations were added to PDMS reservoirs prior modified with rSbpA/ZZ protein and CD3-Ab and observed under the microscope to control the distribution and regularity of cell coverage (Fig. 55).

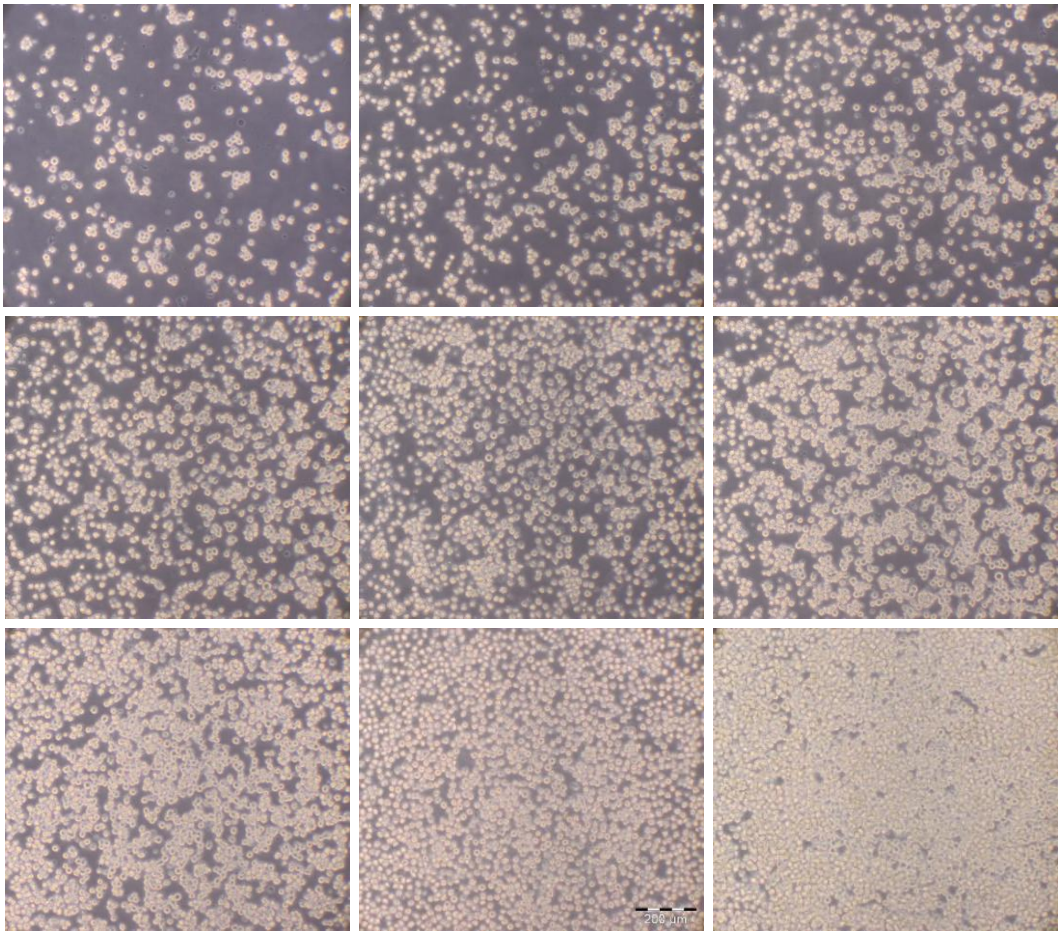

Fig. 55: Jurkat cells captured on glass slides prior modified with rSbpA/ZZ protein and CD3-Ab. The corresponding amounts of cell coverage are 10, 20, 30, 45, 50, 60, 80, 90 and 100%, respectively; scale bar: 200 µm.

The resulting calibration curve shown in Fig. 56 reveals that until a cell coverage amount of about 50% the detection signal increases linearly with the amount of coverage. At coverage amounts higher than 50%, the slope of the calibration curve decreases slightly. The herein presented LS method in the Siemens-Box presents a valuable and reliable tool for the quantification of cell capture. The system is capable of combining LS measurements with

microfluidic cell capture experiments in SU8 microchips; the microchip can be placed within the Siemens-Box resulting in simultaneous microfluidic cell capture and quantification of cell coverage by LS measurements. Besides, the calibration curve can be easily adapted to other cell types.

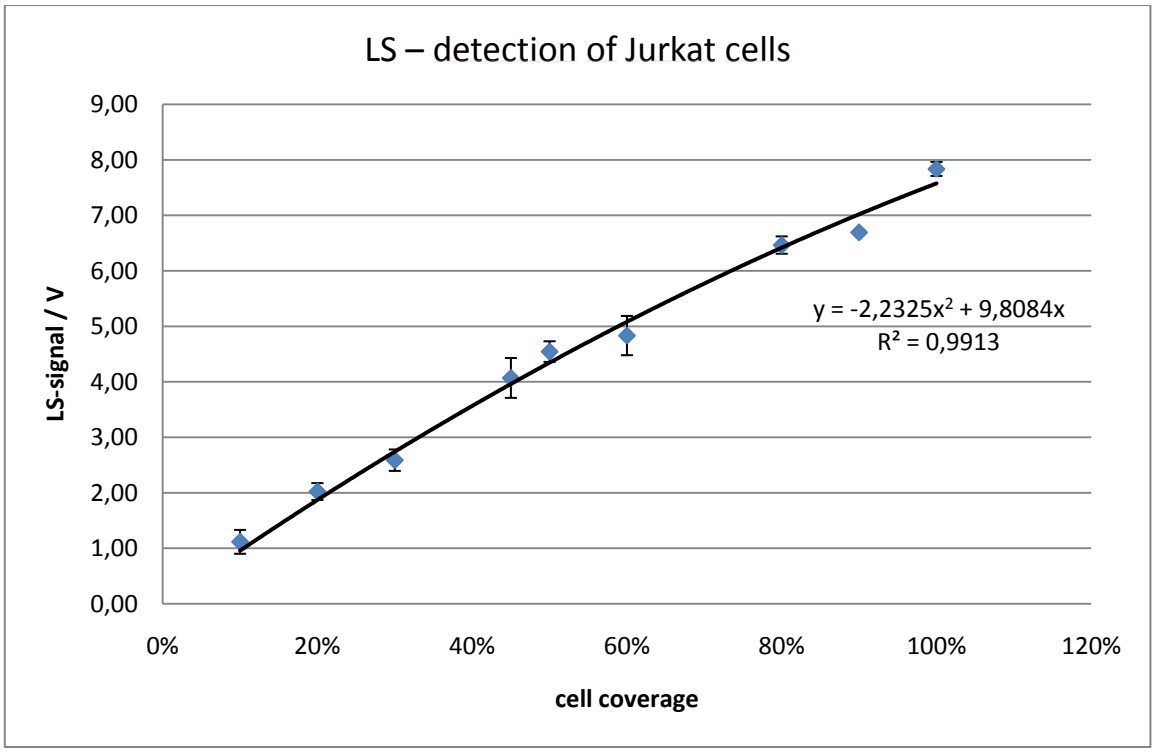

Fig. 56: Calibration curve resulting from LS measurements of several amounts of Jurkat cell coverage.

5 Conclusion

In this thesis, an S-layer fusion protein based CD3-affinity matrix with antifouling properties for immunocapture of CD3-cells in microfluidic devices was developed. The IgG-affinity matrix of the S-layer fusion protein rSbpA$_{31-1068}$/ZZ and its antifouling properties were investigated and affirmed by ELISA and SPR studies with different IgG based antibodies. Additionally, these antibodies could be crosslinked to the S-layer fusion protein without any negative impact on the antibody activity. Due to the development of a CD3-affinity matrix, CD3-cells were successfully captured from suspension via a specific antibody immobilized on the recrystallized S-layer fusion protein. The specific CD3-cell capture could be proved under static conditions by providing a cell mixture and was hence extended to microfluidic experiments. The primary microchip design fabricated of PDMS was further improved by developing a bigger microchannel fabricated of SU8 to obtain higher amounts of captured cells as well as reliable flow conditions. The enhancements provided a stable microfluidic setup and constant flow rates, though the herein used SU8 microchips were still at the beginning of their development and needed further improvements to be applied for cell capture. In terms of an analytical approach, a light scattering detection system (Siemens-Box) was coupled to static cell capture experiments revealing linearity between cell coverage and detection signal which indicates promising upgrading: SU8 microchips can be integrated in the Siemens-Box resulting in simultaneous cell capture and coverage detection. In conclusion, the herein presented affinity matrices based on the S-layer fusion protein rSbpA/ZZ providing useful antifouling properties offer a challenging prospect for the capture of antibodies and cells from suspension as well as from blood. Due to the unique features of microfluidic systems, becoming increasingly relevant for medical point-of-care diagnostics in developing countries, and the multifunctional characteristics of S-layer (fusion) proteins, their combination presents a challenging and promising approach for medical diagnostics and the study of biomolecules.

6 Appendix

6.1 References

1. **Sleytr, U.B., Messner, P., Pum, D., and Sára, M.** Crystalline surface layers on eubacteria and archaeobacteria. *Crystalline bacterial cell surface proteins.* Austin, Texas, USA : R.G. Landes Company and Academic Press, Inc., 1996, pp.6-8.

2. **Sleytr, U.B., Sára, M., Pum, D., Schuster, B., Messner P., Schäffer, C.** Self assembly protein systems: microbial S-layers. *Polyamides and complex proteinaceous materials I.* 2002, Vols. 1, pp. 285-338.

3. **Messner, P., and Sleytr, U.B.** Crystalline bacterial cell surface layers. *Advances in Microbial Physiology.* 1992, Vols. 33, pp. 213-275.

4. **Sára, M., and Sleytr, U.B.** S-layer proteins. *Journal of Bacteriology.* 2000, Vols. 182, pp.859-868.

5. **Sleytr, U.B., Messner, P., Pum, D., and Sára, M.** *Crystalline Bacterial Cell Surface Layers.* Berlin : Springer, 1988.

6. —. *Crystalline bacterial cell surface proteins.* Austin, Texas, USA : R.G. Landes Company and Academic Press, Inc., 1996.

7. —. Crystalline Bacterial Cell Surface Layers (S Layers): From Supramolecular Cell Structure To Biomimetics and Nanotechnology. *Angewandte Chemie, International Edition.* 1999, Vols. 38, pp.1034-1054.

8. **Houwink, A.L.** A macromolecular mono-layer in the cell wall of Spirillium spec. *Biochimica et Biophysica acta.* 1953, Vols. 10, pp.360-366.

9. **Sleytr, UB., Messner, P.** Crystalline Surface Layers On Bacteria. *Annual Review of Microbiology.* 1983, Vols. 37, pp.311-339.

10. **Ilk, N., Egelseer, E.M, and Sleytr, U.B.** S-layer fusion proteins - construction principles. *Current Opinion in Biotechnology.* 2011, Vols. 22, pp.1-8.

11. **Egelseer, E., Ilk, N., Pum, D., Messner, P., Schäffer, C., Schuster, B., Sleytr, UB.** S-Layers, Microbial, Biotechnological Applications. *Encyclopedia of Industrial Biotechnology: Bioprocess, Bioseparation, and Cell Technology.* 2009, pp.1-25.

12. **Sára, M.** Conserved anchoring mechanisms between crystalline cell surface S-layer proteins and secondary cell wall polymers in Gram-positive bacteria? *Trends in Microbiology.* 2001, Vols. 9, pp.47-49.

13. **Sleytr, U.B., and Beveridge, T.J.** Bacterial S-layers. *Trends in Microbiology.* 1999, Vols. 7, pp.253-260.

14. **Sleytr, U.B., Sára, M., Pum, D., and Schuster, B.** Crystalline Bacterial Cell Surface Layers (S-layers): A Versatile Self-Assembly System. [book auth.] A. Ciferri. *Supramolecular Polymers.* s.l. : Boca Raton, pp.583-612, 2005, Vols. pp.583-612.

15. **Messner, P., and Sleytr, U.B.** [book auth.] I.C. and Poxton, I.R. Hancock. *Bacterial Cell Surface Techniques.* Chichester : John Wiley & Sons, pp.97-104, 1988.

16. **Messner, P.** [book auth.] U.B., Messner, P., Pum, D., and Sára, M. Sleytr. *Crystalline bacterial cell surface proteins.* Austin, Texas, USA : R.G. Landes Company and Academic Press, Inc., pp.35-76, 1996.

17. **Sára, M., and Egelseer, E.M.** Funtional aspects of S-layers. [book auth.] U.B., Messner, P., Pum, D., and Sára, M. Sleytr. *Crystalline bacterial cell surface proteins.* Austin, Texas, USA : R.G. Landes Company and Academic Press, Inc., pp.103-131, 1996.

18. **Messner, P., and Schäffer, C.** Surface layer glycoproteins of Bacteria and Archaea. [book auth.] R.J. Doyle. *Glycomicrobiology.* New York : Kluwer Academic/Plenum Publishers, pp.93-125, 2000.

19. **Schäffer, C., and Messner, P.** Prokaryotic glycoproteins. [book auth.] W., Falk, H., Kirby, G.W., Moore, R.E., Tamm, C. Herz. *Progress in the chemistry of organic natural products.* Wien, New York : Springer, Vols. 85, pp.51-124, 2003.

20. **Novotny, R., Pföstl, A., Messner, P., and Schäffer, C.** Genetic organization of chromosomal S-layer glycan biosynthesis loci of Bacillaceae. *Glycoconjugate Journal.* 2004, Vols. 20, pp.435-447.

21. **Thomas, S.R., and Trust, T.J.** Tyrosine phosphorylation of the tetragonal paracrystalline array of Aeromonas hydrophila: molecular cloning and high-level expression of the S-layer protein gene. *Journal of Molecular Biology.* 1995, Vols. 245, pp.568-581.

22. **Boot, H.J., Kolen C.P., van Noort, J.M., and Pouwels, P.H.** S-layer protein of Lactobacillus acidophilus ATCC 4356: purification, expression in Escherichia coli, and nucleotide sequence of the corresponding gene. *Journal of Bacteriology.* 1993, Vols. 175, pp. 6089-6096.

23. **Sleytr, U.B., and Glauert, A.M.** Ultrastructure of the cell walls of two closely related clostridia that possess different regular arrays of surface subunits. *Journal of Bacteriology.* 1976, Vols. 126, pp.869-882.

24. **Sleytr, UB., Huber, C., Ilk, N., Schuster, B., Egelseer, E.** S-layers as a toolkit for nanobiotechnological applications. *FEMS Microbiology Letters.* 2007, Vols. 267, pp.131-144.

25. **Pum, D., Sára, M., and Sleytr, U.B.** Structure, surface charge, and self-assembly of the S-layer lattice from Bacillus coagulans E38-66. *Journal of Bacteriology.* 1989, Vols. 171, pp.5296-5303.

26. **Sára, M., and Weigert, S.** Ultrafiltration membranes prepared from crystalline bacterial cell surface layers as a model system for studying the influence of surface properties on protein adsorbtion. *Journal of Membrane Science.* 1996, Vols. 121(2), pp.185-196.

27. **Pleschberger, M., Saerens, D., Weigert, S., Sleytr, U.B., Muyldermans, S., Sára, M., Egelseer, E.M.** An S-layer heavy chain camel antibody fusion protein for generation of a nanopatterned sensing

layer to detect the prostate-specific antigen by surface plasmon resonance technology. *Bioconjugate Chemistry.* 2004, Vols. 15, pp.664-671.

28. **Ilk, N., Egelseer, E.M., Ferner-Ortner, J., Küpcü, S., Pum, D., Schuster, B., Sleytr, U.B.** Surfaces functionalized with self-assembling S-layer fusion proteins for nanobiotechnological applications. *Colloids and Surfaces A: Physicochem. Eng. Aspects* . 2008, Vols. 321, pp.163-167.

29. **Ilk, N., Völlenkle, C., Egelseer, E.M., Breitwieser, A., Sleytr, U.B., and Sára, M.** Molecular Characterization of the S-Layer Gene, sbpA, of Bacillus sphaericus CCM 2177 and Production of a Functional S-Layer Fusion Protein with the Ability To Recrystallize in a Defined Orientation while Presenting the Fused Allergen. *Applied and Environmental Microbiology* . 2002, pp.3251-3260.

30. **Tschiggerl, H., Breitwieser, A., de Roo, G., Verwoerd, T., Schäffer, C., Sleytr, U.B.** Exploitation of the S-layer self-assembly system for site directed immobilization of enzymes demonstrated for an extremophilic laminarinase from Pyrococcus furiosus. *Journal of Biotechnology* . 2008, Vols. 133, pp.403-411.

31. **Tschiggerl, H., Casey, J.L., Parisi, K., Foley, M., Sleytr, U.B.** Display of a Peptide Mimotope on a Crystalline Bacterial Cell Surface Layer (S-layer) Lattice for Diagnosis of Epstein–Barr Virus Infection. *Bioconjugate Chemisry* . 2008 , Vols. 19, pp.860-865.

32. **Pleschberger, M., Neubauer, A., Egelseer, E.M., Weigert, S., Lindner, B., Sleytr, U.B., Muyldermans, S., and Sára, M.** Generation of a Functional Monomolecular Protein Lattice Consisting of an S-Layer Fusion Protein Comprising the Variable Domain of a Camel Heavy Chain Antibody. *Bioconjugate Chemistry.* 2003, Vols. 14, 440-448.

33. **Völlenkle, C., Weigert, S., Ilk, N., Egelseer, E.M., Weber, V., Loth, F., Falkenhagen, D., Sleytr, U.B., and Sára, M.** Construction of a Functional S-Layer Fusion Protein Comprising an Immunoglobulin G-Binding Domain for Development of Specific Adsorbents for Extracorporeal Blood Purification. *Applied and Environmental Microbiology.* 2004, pp.1514-1521.

34. **Moks, T., Abrahmsen, L., Nilsson, B., Hellman, U., Sjoquist, J., and Uhlén, M.** Staphylococcal protein A consists of five IgG-binding domains. *European Journal of Biochemistry* . 1986, Vols. 156, pp.637-643.

35. http://oiboib.blogspot.com. [Online] [Cited: July 25., 2011.] http://oiboib.blogspot.com/2010/05/medsci-203-62-infection-1-sl-l-ln-p.html.

36. **Whitesides, G.M.** The origins and the future of microfluidics. *Nature.* 2006, Vols. 442, pp.368-373.

37. http://gigaomized-green-demo.blogspot.com. [Online] [Cited: June 05., 2011.] http://gigaomized-green-demo.blogspot.com/2011/02/lab-on-chip-what-is-this.html.

38. **Park, TH., Shuler, ML.** Integration of Cell Culture and Microfabrication Technology. 2003, Vols. 19, pp.243-253.

39. **Wu, M.-H., Huang, S.-B., Lee, G.-B.** Microfluidic cell culture systems for drug research. *Lab on a Chip.* 2010, Vols. 10, pp.939-956.

40. **Yeon, J.H., Park, J.-K.** Microfluidic Cell Culture Systems for Cellular Analysis. *Biochip Journal.* 2007, Vols. 1, pp.17-27.

41. **Schumacher, J.T., Grodrian, A., Kremin, C., Hoffmann, M., and Metze, J.** Hydrophobic coating of microfluidic chips structured by SU-8 polymer for segmented flow operation . *Journal of Micromechanics and Microengineering.* 2008, Vols. 18 (5), 055019.

42. **Wang, Y., Pai, J.-H., Lai, H.-H.,Sims, C.E., Bachman, M., Li, G.P. and Allbritton, N.L.** Surface graft polymerization of SU-8 for bio-MEMS applications . *Journal of Micromechanics and Microengineering.* 2007, Vols. 17 (7), pp.1371-1380.

43. **Takayama, S., Ostuni, E., Qian, X., McDonald, J.C., Jiang, X., LeDuc, P., Wu., M.-H., Ingber, D.E., Whitesides, G.M.** Topograhpical Micropatterning of Poly(dimethylsiloxane) Using Laminar Flows of Liquids in Capillaries. *Advanced Materials.* 2001, Vols. 13, pp.570-574.

44. **Geschke, O., Klank, H., Tellemann, P.** *Microsystem Engineering of Lab-on-a-Chip Devices.* 1. s.l. : John Wiley & Sons, 2004. pp. 14-19.

45. *Bubbles no more: Trapping removal of gas bubbles in single-layer elastomeric devices.* **Lochovsky, C., Yasotharan, S., Günther, A.** Groningen, The Netherlands : s.n., 3-7 October 2010, pp.1805-1807. 14th International Conference on Miniaturized Systems for Chemistry and Life Sciences.

46. **Kang, J.H., Kim, Y.C., Park., J.-K.** Analysis of pressure-driven air bubble elimination in a microfluidic device. *Lab on a Chip.* 2008, Vols. 8, pp.176-178.

47. **Kim, L., Toh, Y.-C., Voldman, J., Yu, H.** A practical guide to microfluidic perfusion culture of adherent mammalian cells. *Lab on a Chip.* 2007, Vols. 7, pp.681-694.

48. **Pratt, E.D., Huang, C., Hawkins, B.G., Gleghorn, J.P., b, Kirby, B.J.** Rare cell capture in microfluidic devices. *Chemical Engineering Science.* 2011, Vols. 66, pp.1508-1522.

49. http://www.apocell.com. [Online] [Cited: July 07., 2011.] http://www.apocell.com/ctc-technology-2/apostreamtm-technology/.

50. **Cheng, X., Irimia, D., Dixon, M., Sekine, K., Demirci, U., Zamir, L., Tompkins, R.G., Rodriguez, W., Toner, M.** A microfluidic device for practical label-free CD4+ T cell counting of HIV-infected subjects. *Lab on a Chip.* 2007, Vols. 7, pp. 170-178.

51. **Cheng, X., Gupta, A., Chen, C., Tompkins, R.G., Rodriguez, W., Tonera, M.** Enhancing the performance of a point-of-care CD4+ T-cell counting microchip through monocyte depletion . *Lab on a Chip.* 2009, Vols. 9, pp.1357-1364.

52. **Adams, A.A., Okagbare, P.I., Feng, J., Hupert, M.L., Patterson, D., Göttert, J., McCarley, R.L., Nikitopoulos, D., Murphy, M.C., Soper, S.A.** Highly Efficient Circulating Tumor Cell Isolation from Whole Blood and Label-Free Enumeration Using Polymer-Based Microfluidics with an Integrated Conductivity Sensor. 2008, Vols. 130 (8), pp. 633-8641.

53. **Rodriguez, W.R., Christodoulides, N., Floriano, P.N., Graham, S., Mohanty, S., Dixon, M., Hsiang, M., Peter, T., Zavahir, S., Thior, I., Romanovicz, D., Bernard, B., Goodey, A.P., Walker,**

B.D., McDevitt, J.T. A Microchip CD4 Counting Method for HIV Monitoring in Resource-Poor Settings. *PLoS Medicine.* 2005, Vols. 2 (7), e182.

54. **Cheng, X., Irimia, D., Dixon, M., Ziperstein, J.C., Demirci, U., Zamir, L., Tompkins, R.G., Toner, M., Rodriguez, W.R.** A microchip approach for practical label-free CD4+ T-cell counting of HIV-infected subjects in resource-poor settings. *Journal of Acquired Immune Deficiency Syndromes.* 2007, Vols. 45 (3), pp.257-261.

55. [Online] [Cited: July 25., 2011.] http://www.searo.who.int/LinkFiles/BCT_HLM-392.pdf.

56. **Usami, S., Chen, H.H., Zhao, Y., Chien, S., Skalak, R.** Design and construction of a linear shear stress flow chamber. *Annals of Biomedical Engineering.* 1993, Vols. 21, pp.77-83.

57. **Watkins, N.N., Sridhar, S., Cheng, X., Chen, G.D, Toner, M., Rodriguez, W., Bashir, R.** A microfabricated electrical differential counter for the selective enumeration of CD4+ T lymphocytes. *Lab on a Chip.* 2011, Vols. 11 (8), pp.1437-1447.

58. **Xu, Y., Phillips, J.A., Yan, J., Li, Q., Fan, Z.H., Tan, W.** Aptamer-based microfluidic device for enrichment, sorting, and detection of multiple cancer cells. *Analytical Chemistry.* 2009, Vols. 81 (17), pp.7436-7442.

59. **Yager, P., Edwards, T., Fu, E., Helton, K., Nelson, K., Tam, M.R., Weigl, B.H.** Microfluidic Diagnostic Technologies for Global Public Health. *Nature.* 2006, Vols. 442, pp.412-418.

60. **Reyes, D.R., Iossifidis, D., Auroux, P.A., Manz, A.** Micro Total Analysis Systems. 1. Introduction, Theory, and Technology. *Analytical Chemistry.* 2002 , Vols. 74, pp.2623-2636.

61. **Dittrich, P.S., Tachikawa, K., Manz, A.** Micro Total Analysis Systems. Latest Advancements and Trends. *Analytical Chemistry.* 2006, Vols. 78, pp.3887-3907.

62. **Mairhofer, J., Roppert, K. and Ertl, P.** Microfluidic Systems for Pathogen Sensing: A Review. *Sensors.* 2009, Vols. 9, pp.4804-4823.

63. **Kuswandi, B., Nuriman, Huskens, J., Verboom, W.** Optical sensing systems for microfluidic devices: A review. *Analytica Chimica Acta.* 2007, Vols. 601, pp.141-155.

64. **Lee, S.J., Park, J.S., Im, H.T., Jung, H.-I.** A Microfluidic ATP-bioluminescence Sensor for the Detection of Airborne Microbes. *Sensors and Actuators B.* 2008, Vols. 132, pp.443-448.

65. **Lee, S.-H., Cho, S.I., Lee, C.-S., Kim, B.-G., Kim, Y.-K.** Microfluidic chip for biochemical reaction and electrophoretic separation by quantitative volume control . 2005, Vols. 110, pp.164-173 .

66. **Huang, X., Ren, J.** On-line chemiluminescence detection for isoelectric focusing of heme proteins on microchips. 2005, Vols. 26 (19), pp.3595-3601.

67. **Malic, L., Kirk, A.G.** Integrated miniaturized optical detection platform for fluorescence and absorption spectroscopy . *Sensors and Actuators A: Physical.* 2007, Vols. 135 (2), pp.515-524 .

68. **Balslev, S., Jorgensen, A.M., Bilenberg, B., Mogensen, K.B., Snakenborg, D., Geschke, O., Kutter, J.P., Kristensen, A.** Lab-on-a-chip with integrated optical transducers. *Lab on a Chip.* 2006, Vols. 6, pp.213-217.

69. **Wojciechowski, J.R., Shriver-Lake, L.C., Yamaguchi, M.Y., Füreder, E., Pieler, R., Schamesberger, M., Winder, C., Prall, H.J., Sonnleitner, M., and Ligler, F.S.** Organic Photodiodes for Biosensor Miniaturization. *Analytical Chemistry.* 2009, Vols. 81, pp.3455-3461.

70. **Egelseer, E.M., Leitner, K., Jarosch, M., Hotzy, C., Zayni, S., Sleytr, U.B., Sára, M.** The S-layer proteins of two Bacillus stearothermophilus wild-type strains are bound via their N-terminal region to a secondary cell wall polymer of identical chemical composition. *Journal of Bacteriology.* 1998, Vols. 180, pp.1488-1495.

71. **Binnig, G., Quate, C.F., Gerber, C.** Atomic Force Microscope. *Physical Review Letters.* 1986, Vols. 56 (9), pp.930-933.

72. **Addae-Mensah, K.A., Wikswo, J.P.** Measurement techniques for cellular biomechanics in vitro. *Experimental Biology and Medicine.* 2008, Vols. 233, pp.792-809.

73. **Kirmizis, D., Logothetidis, S.** Atomic force microscopy probing in the measurement of cell mechanics. *International Journal of Nanomedicine.* 2010 , Vols. 7, pp.137-145.

74. [Online] [Cited: July 21., 2011.] http://www.farmfak.uu.se/farm/farmfyskem-web/instrumentation/afm.shtml.

75. **Perlmann, P. and Perlmann, H.** Wiley Online Library. Enzyme-Linked Immunosorbent Assay. [Online] April 19., 2001. [Cited: July 20., 2011.] http://onlinelibrary.wiley.com/doi/10.1038/npg.els.0002625/pdf.

76. **Lequin, R.M.** Enzyme Immunoassay (EIA)/Enzyme-Linked Immunosorbent Assay (ELISA). *Clinical Chemistry* . 2005, Vols. 51, pp.2415-2418.

77. http://www.leinco.com. [Online] [Cited: July 19, 2011.] http://www.leinco.com/indirect_elisa.

78. http://thefutureofthings.com. [Online] [Cited: July 19, 2011.] http://thefutureofthings.com/articles.php?itemId=37/56/.

79. **Breitwieser, A., Küpcü, S., Howorka, S., Weigert, S., Langer, C., Hoffmann-Sommergruber, K., Scheiner, O., Sleytr, U.B., and Sára, M.** 2-D Protein Crystals as an Immobilization Matrix for Producing Reaction Zones in Dipstick-Style Immunoassays. *BioTechniques.* 1996, Vols. 21, pp.918-925.

80. *http://www.applichem.com.* [Online] AppliChem. [Cited: August 8., 2011.] http://www.applichem.com/en/shop/product-detail/as/iblockingi-reagenz-ca/.

81. [Online] [Cited: July 19, 2011.] http://www.piercenet.com/Objects/View.cfm?type=ProductFamily&ID=02030224.

82. **Hoaa, X.D., Kirk, A.G., Tabrizian, M.** Towards integrated and sensitive surface plasmon resonance biosensors: A review of recent progress. *Biosensors and Bioelectronics* . 2007, Vols. 23, pp.151-160.

83. **Cooper, M.A.** Optical biosensors in drug discovery. *Nature Reviews Drug Discovery.* Vols. 1, pp.515-528.

84. **Cal, l M.E., Pyrdol, J., Wucherpfennig, K.W.** Stoichiometry of the T-cell receptor-CD3 complex and key intermediates assembled in the endoplasmic reticulum. *The EMBO Journal.* 2004, Vols. 23 (12), pp.2348-2357.

85. **de Felipe, P.** Skipping the co-expression problem: the new 2A "CHYSEL" technology. *Genetic Vaccines and Therapy.* 2004, Vol. 2:13.

86. **Schneider, U., Schwenk, H.U., Bornkamm, G.** Characterization of EBV-genome negative "null" and "T" cell lines derived from children with acute lymphoblastic leukemia and leukemic transformed non-Hodgkin lymphoma. *International Journal of Cancer.* 1977, Vols. 19 (5), pp.621-626.

87. **Deng, J., Schoenbach, K.H., Buesche,r E.S., Hair, P.S., Fox, P.M., Beebe, S.J.** The effects of intense submicrosecond electrical pulses on cells. *Biophysical Journal.* 2003, Vols. 84 (4), pp. 2709-2714.

88. **Zhang, C., Xu, Y., Gu, J, Schlossman, S.F.** A cell surface receptor defined by a mAb mediates a unique type of cell death similar to oncosis. *Proceedings of the National Academy of Sciences USA.* 1998, Vols. 95 (11), pp.6290-6295.

89. goldbook.iupac.org. [Online] [Cited: July 21, 2011.] http://goldbook.iupac.org/P04598.html.

90. **Tedde, S.F., Kern, J., Sterzl, T., Fürst, J., Lugli, P., Hayden, O.** Fully spray coated organic photodiodes. *Nano Letters.* 2009, Vols. 9 (3), pp.980-983.

91. **Picher, M.M.** Nanobiotechnology advanced Lab-on-a-Chip for continuous blood glucose monitoring. *Master thesis at the Department of NanoBiotechnology, University of Natural Resources and Life Sciences, Vienna.* 2010.

92. **Kuncová-Kallio, J., and Kallio, P.J.** PDMS and its Suitability for Analytical Microfluidic Devices. *EMBS Annual International Conference, New York City, USA.* 2006, pp.2486-2489.

6.2 List of Figures

Fig. 1: Electron micrographs of freeze-etched preparations of intact cells. 1
Fig. 2: Schematic illustration of the cell wall architecture of gram-positive archaea and bacteria containing crystalline S-layer proteins (11), modified. 2
Fig. 3: Schematic drawing of S-layer lattice types. The regular arrays exhibit oblique (p1, p2), square (p4), or hexagonal lattice symmetry (p3, p6) (24). 3
Fig. 4: Schematic of the reassembly of native and recombinant S-layer proteins into crystalline arrays. 4
Fig. 5: Schematic illustrating self-assembled S-layer fusion proteins with target molecules or nanoparticles bound in defined spacing and orientation (24). 5
Fig. 6: Microscope images of recrystallized SbpA fusion proteins showing square lattice structure. 6
Fig. 7: 1) Schematic of immunogloblins bound to a bacterium and 2) to staphylococcal protein A (SPA). 7
Fig. 8: Illustration of the immobilization of human IgG on rSbpA/ZZ (33). 7
Fig. 9: Schematic of how laboratory functions are confined in a microchip (37). 8
Fig. 10: Photograph of a microfluidic chemostat used to study the growth of microbial populations. 9
Fig. 11: Schematic of the two-plate model explaining fluid viscosity. 10
Fig. 12: Schematic of microfabrication procedures of a microfluidic chip. 11
Fig. 13: Schematic of removing trapped air bubbles using a pressurized microchannel with a PDMS ceiling (47). 12
Fig. 14: A microchannel flow field to isolate circulating tumor cells using DEP-FFF. 14
Fig. 15: Microfluidic devices used in the CD4+ T-cell counting studies. 16
Fig. 16: Microfluidic device and detection of three different cancer cell lines. 17
Fig. 17: Common setups used for LIF and CL detection. 20
Fig. 18: Photographs of two on-chip approaches and a hand-held controller. 21
Fig. 19: Atomic Force Microscopy (AFM) principle. 25
Fig. 20: Schematic setup of a “Sandwich ELISA”. 27
Fig. 21: Conversion of $TMBH_2$ to TMB by enzymatic reaction with H_2O_2 and peroxidase (POD). 29
Fig. 22: Conversion of p-NPP to p-nitrophenol by enzymatic reaction with alkaline phosphatase (ALP). 29
Fig. 23: Typical setup for an SPR biosensor. 31
Fig. 24: Schematic illustration of the immobilization of human IgG on rSbpA/ZZ recrystallized on the gold support via thiolated SCWP (33), slightly modified. 33
Fig. 25: Schematic of the TCR-CD3 complex across the cytoplasmic membrane. 36
Fig. 26: SEM image of Jurkat cells with scale bars of 10 µm (C) and 1 µm (F) (88). 37
Fig. 27: Eclipse TE2000-S inverted fluorescence microscope (Nikon Instruments, Japan). 39

Fig. 28: Schematic of microfluidic Jurkat cell capture via CD3-Ab immobilized on rSbpA/ZZ..... 40
Fig. 29: Master mold design for PDMS fabricated microchips..... 41
Fig. 30: Master mold design for SU fabricated microchips. 41
Fig. 31: Schematic of the process for the fabrication of an SU8 master mold. 42
Fig. 32: Plasma bonding procedure for PDMS microchips..... 43
Fig. 33: System setup for microfluidic Jurkat cell capture..... 45
Fig. 34: Microfluidic cell capture procedure..... 46
Fig. 35: Injecting/withdrawing syringe pump (KDS-260-CE, kdScientific, USA)..... 47
Fig. 36: Mounting station with SU8 microchip (left) and microscopical setup (right). 48
Fig. 37: Microfluidic setup comprising of the SU8 microchip, the in- and outlet valve, and several tubes (sample, reservoir and waste). The valves are switched to the withdrawing mode. 49
Fig. 38: OPD layout with glass encapsulation..... 52
Fig. 39: Siemens-Box consisting of light source, neutral density filter, aperture, microchip mounting station, notch filter and OPDs. 52
Fig. 40: Schematic of the LS setup for the detection of Jurkat cell capture..... 53
Fig. 41: AFM images of the recrystallized S-layer fusion protein rSbpA/ZZ..... 55
Fig. 42: Detection of human IgG immobilized on SbpA and rSbpA/ZZ. 57
Fig. 43: ALP-detection of human IgG immobilized on rSbpA/ZZ. 58
Fig. 44: SPR-sensorgram showing the binding of the S-layer proteins SbpA (pink) and rSbpA/ZZ (red) on gold precoated with thiolated SCWP. 59
Fig. 45: Investigation of the rSbpA/ZZ antifouling properties compared to gold against full-plasma. 60
Fig. 46: Investigation of the rSbpA/ZZ antifouling properties compared to gold against IgG-free plasma..... 61
Fig. 47: SPR-sensorgram showing the immobilization of human IgG and CD3-Ab on rSbpA/ZZ protein..... 62
Fig. 48: Binding of full-plasma to the CD3-affinity matrix (pink) and gold (green) leading to an increase of ~750 RU and ~3900 RU, respectively. 63
Fig. 49: Light microscope images of Jurkat cells captured via CD3-Ab immobilized on rSbpA/ZZ.. 64
Fig. 50: (left) Labeled Jurkat cells, (right) labeled MOLT 3 cells, scale bars: 100 µm. 65
Fig. 51: Specific capture of Jurkat cells from cell mixtures via CD3-Ab immobilized on rSbpA/ZZ.. 65
Fig. 52: Microfluidic Jurkat cell capture via CD3-Ab immobilized on the rSbpA/ZZ coated microchannel. 66
Fig. 53: Improved setup with microchip mounting station and two stabilized diagonal four-way valves. 68
Fig. 54: Jurkat cell capture in modified SU8 microchips. 69
Fig. 55: Jurkat cells captured on glass slides prior modified with rSbpA/ZZ protein and CD3-Ab. 70

Fig. 56: Calibration curve resulting from LS measurements of several amounts of Jurkat cell coverage. 71

6.3 List of Tables

Table 1: Buffers and reagents used for SPR experiments. 32
Table 2: Recrystallization of rSbpA/ZZ and SbpA on gold prior modified with thiolated SCWP. 32
Table 3: Basic setup with coating of thiolated SCWP and rSbpA/ZZ. 33
Table 4: Investigation of antifouling properties of rSbpA/ZZ against IgG-free plasma and full-plasma in comparison to gold. 34
Table 5: Immobilization of human IgG and CD3-Ab to rSbpA/ZZ. 34
Table 6: Antifouling experiments with IgG-free plasma on CD3-Ab prior immobilized on rSbpA/ZZ and crosslinked with DMP. 35
Table 7: Antifouling experiments with full plasma on human IgG and CD3-Ab prior immobilized on rSbpA/ZZ and crosslinked with DMP. 35
Table 8: Absorption/emission spectra for the fluorophors and filter blocks. 39
Table 9: Components of the microfluidic tubing system for PDMS microchips. 44
Table 10: Components of the microfluidic tubing system for SU8 microchips. 47
Table 11: Detection signals of human IgG immobilized on rSbpA/ZZ. Optionally crosslinked with DMP, measured at 405 nm. 57

6.4 Abbreviations

AFM ..... Atomic Force Microscopy
AIT ..... Austrian Institute of Technologies
ALP ..... alkaline phosphatase
CD3-Ab ..... purified mouse human anti-CD3, IgG2a, monoclonal
DMP ..... Dimethyl pimelimidate dihydrochloride
DNBT ..... Department of NanoBiotechnology
ELISA ..... enzyme linked immunosorbent assay
full-plasma ..... human heparin plasma
IgG ..... Immunoglobulin G
IgG-free plasma ..... human heparin plasma purified from IgG
LOC ..... lab-on-a-chip
LS ..... light scattering
µTAS ..... micro total analysis system
OPD ..... organic photodiode
PBS ..... Phosphate buffered saline solution
PDMS ..... polydimethylsiloxane
POD ..... peroxidase
rSbpA/ZZ ..... $rSbpA_{31-1068}$/ZZ of *Lysinibacillus sphaericus* CCM 2177
S-layer ..... surface layer
SbpA ..... S-layer protein of *Lysinibacillus sphaericus* CCM 2177
SCWP ..... secondary cell wall polymer
SPR ..... Surface Plasmon Resonance
SU8 ..... epoxybased negative photoresist